KU LEUVEN

ARENBERG DOCTORAL SCHOOL
Faculty of Engineering Technology

Indoor Multipath Assisted Angle of Arrival Localization

Stijn Wielandt

Supervisor:
Prof. dr. ir. L. De Strycker
Co-supervisor:
Prof. dr. ir. B. Nauwelaers

Dissertation presented in partial fulfillment of the requirements for the degree of Doctor of Engineering Technology (PhD)

November 2017

Indoor Multipath Assisted Angle of Arrival Localization

Stijn WIELANDT

Examination committee:
Prof. dr. ir. D. Moens, chair
Prof. dr. ir. L. De Strycker, supervisor
Prof. dr. ir. B. Nauwelaers, co-supervisor
Ing. J.-P. Goemaere
Dr. ir. N. Stevens
Prof. dr. ir. L. Van der Perre
Prof. dr. ir. J. Bauwelinck
(Ghent University - Belgium)
Prof. dr.-ing. M. Kuhn
(Darmstadt University of Applied Sciences - Germany)
Dr. ir. P. Lambrecht
(Newtec Cy - Belgium)

Dissertation presented in partial fulfillment of the requirements for the degree of Doctor of Engineering Technology (PhD)

November 2017

Uitgegeven in eigen beheer, Stijn Wielandt, Gebroeders De Smetstraat 1, B-9000 Gent (Belgium)

Preface

In this thesis, I proudly present my work of the past four years. The last months mainly consisted of technical reflections, however, in this final statement I would like to express my gratitude to the people that contributed to this end result in any way.

My career in academics started in 2011, when I joined the DRAMCO research group for investigating wireless power systems. Nobby Stevens, Jean-Pierre Goemaere, Prof. Lieven De Strycker and Prof. Liesbet Van der Perre deserve a great thank you for their support and belief, and all the opportunities they created during the past six years. In October 2013, I was given the chance to start a PhD in the field of indoor multipath assisted AoA localization. The journey that followed was marked by ups and downs, but I could always fall back upon my colleagues for inspiration, support and friendship. Gilles, Bogdan, Dries, Joyrai, Qingli, Yanxiang, Geoffrey, Guus, Anneleen, Other Stijn, Ben, Davy, Bart, Henk, Bert, Jeroen, Tom, Kenneth, Steven, Willem, Jan, Karel, The Old Kevin and The New Kevin: thank you, you made our office a fascinating workplace. I will always connect the smell of hot glue, burned flux and sawdust to our lab. Occasionally, my research also brought me to the campus in Leuven. In this context, I am particularly grateful to Cheng-Ming, Sen and Vladimir of TELEMIC for offering their RF expertise and insights. In 2015 and 2016, I had the opportunity to work at the Darmstadt University of Applied Sciences for two months. Therefore, a special thanks goes out to Prof. Michael Kuhn for hosting me twice, these experiences were not only fruitful from a technical point of view, but also meant a cultural enrichment. Sharing an office with Tobias and Matthias was great, and I genuinely appreciate all efforts and contributions of the professors of the department of electrical engineering and information technology. My work as a researcher also involved the supervision of bachelor and master thesis students in Ghent and in Darmstadt. I wish to praise them for their motivation and diligence, which often resulted in nice results and demonstrations in my field of research.

The outcome of this PhD is the result of the guidance by my advisory committee. I am thankful to Prof. Lieven De Strycker and Prof. Bart Nauwelaers for taking on the roles of supervisors, guiding me towards this end point. Also my assessors contributed to this result with constructive remarks and advice. Therefore I would like to thank Peter Lambrecht, Prof. Michael Kuhn, Jean-Pierre Goemaere and Nobby Stevens. I am also grateful to the extra jury members, Prof. Johan Bauwelinck and Prof. Liesbet Van der Perre, for their expert judgement and contribution to the quality of this text. Furthermore, I wish to thank Prof. David Moens for presiding the jury.

Last but not least, I want to express my gratitude towards my friends and family, who supported me along the way and interestedly listened to my stories about beamforming, or at least pretended to. I especially want to thank my parents for their endless support and encouragement. The opportunities they gave me brought me where I am today.

Stijn Wielandt
August 5, 2017
Sint-Niklaas

Abstract

Indoor positioning systems enable a broad range of location aware applications, ranging from guidance and tracking to position based entertainment. A multitude of localization systems exists, but Radio Frequency (RF) technologies are mostly preferred, due to the omnipresence of wireless communication infrastructure and handsets. However, the localization accuracy is often impaired by Non-Line-Of-Sight (NLOS) connections and indoor multipath effects, driving further research in this domain. An interesting evolution in widely deployed communication systems is the transition to multi-antenna devices with beamforming capabilities. These properties form an opportunity for localization methods based on Angle of Arrival (AoA) estimation.

This work investigates how multipath propagation can be exploited to enhance the accuracy of AoA localization systems. The presented multipath assisted method resembles a fingerprinting approach, matching an AoA measurement vector to a set of reference vectors. In contrast to common fingerprinting systems, reference data is not generated by labor intensive site surveying. Instead, a ray tracer is developed, simulating Line-Of-Sight (LOS) and specularly reflected multipath components based on a-priori known floor plan information. For the calculation of AoA measurement vectors, the established MVDR, MUSIC and ESPRIT algorithms are employed. The resulting algorithm requires only one fixed receiving antenna array to determine the position of a mobile transmitter in a room.

The proposed method is implemented in a Matlab® framework for indoor positioning, allowing an extensive optimization and evaluation of the developed localization algorithms. All tests are performed in LOS and NLOS conditions, providing insights in the robustness of the system. For the acquisition of real-world measurement data, a flexible hardware setup is designed, consisting of a linear synthetic antenna array for the 2.4 GHz and 5 GHz bands. The measurements are performed in various environments, allowing an assessment of localization accuracy as a function of building materials and room sizes. Also,

the performance of the implemented multipath simulator is examined. At the infrastructure side, multiple hardware parameters are investigated, for example the size of the antenna array, the number of arrays and their geometrical organization, the operating frequency, the number of array snapshots, etc. Finally, the combination of AoA with received signal strength and time of flight techniques is demonstrated within the same localization framework.

In order to assess the added value of simulating multipath components, all measurements are processed by the multipath assisted AoA method, as well as a standard AoA approach. These tests indicate the superior accuracy of the multipath assisted method, especially in NLOS conditions. Furthermore, the performance of the presented system is compared to results in literature. This leads to the conclusion that the proposed system yields a considerable accuracy improvement over similar RF positioning systems.

Beknopte samenvatting

Systemen voor indoor lokalisatie maken plaatsafhankelijke toepassingen mogelijk, zoals het volgen en begeleiden van personen of toestellen. Ondanks het uitgebreide gamma van bestaande lokalisatietechnieken gaat de voorkeur meestal uit naar radiofrequente (RF) systemen, omwille van de alomtegenwoordige infrastructuur voor draadloze netwerken. Nochtans zijn deze systemen onderhevig aan multipadeffecten en Non-Line-Of-Sight (NLOS) verbindingen. Courante communicatiesystemen worden meer en meer uitgerust met beamforming technologie op basis van meerdere antennes. Deze evolutie biedt opportuniteiten voor lokalisatietechnieken op basis van Angle of Arrival (AoA) metingen.

In dit onderzoek wordt een AoA lokalisatiesysteem ontworpen dat multipadpropagatie benut voor extra nauwkeurigheid. De voorgestelde techniek met multipadassistentie leunt aan bij de courante fingerprinting methode, aangezien de overeenkomst bepaald wordt tussen een opgemeten vector en een set van referentievectoren. De nieuwe techniek onderscheidt zich echter van standaard fingerprinting technieken, omdat de referentievectoren niet worden opgebouwd uit meetwaarden. In plaats daarvan worden de referentiewaarden berekend door een multipadsimulator. Hiertoe wordt een ray tracer ontworpen die de Line-Of-Sight (LOS) verbinding en de speculaire reflecties berekent op basis van een grondplan. Voor de berekening van de opgemeten vector worden bestaande AoA algoritmes gebruikt, zoals MVDR, MUSIC en ESPRIT. Het resultaat is een algoritme dat de positie van een mobiele zender kan bepalen met behulp van een enkele antenne array op een vaste locatie.

De voorgestelde lokalisatiemethode wordt geïmplementeerd in Matlab®, waardoor de ontwikkelde algoritmes uitgebreid geoptimaliseerd en getest kunnen worden. Alle tests worden uitgevoerd met zowel LOS als NLOS connecties, wat de robuustheid van het systeem in wisselende omstandigheden demonstreert. Voor het verzamelen van realistische meetdata in de 2,4 GHz en 5 GHz frequentiebanden wordt een synthetische antenne array ontworpen. De metingen worden uitgevoerd in verscheidene omgevingen, waardoor de werking

van het plaatsbepalingsalgoritme geanalyseerd kan worden in functie van de bouwmaterialen en de kamergrootte. Bovendien illustreren deze metingen de nauwkeurigheid van de ontworpen ray tracer. Aan de infrastructuurzijde worden verscheidene hardware parameters onderzocht, zoals de grootte van de antenne array, het aantal arrays en hun geometrische opstelling, de werkingsfrequentie, het aantal metingen, etc. Tenslotte volgt een demonstratie van de voorgestelde AoA techniek, gecombineerd met lokalisatiemethoden gebaseerd op signaalsterkte of -vertraging.

Om de waarde van de multipadassistentie te beoordelen, worden alle metingen verwerkt met zowel het voorgestelde algoritme als een standaard (LOS) AoA methode. Deze tests wijzen op een verhoogde nauwkeurigheid wanneer multipad propagatie in rekening wordt gebracht, in het bijzonder bij NLOS connecties. Verder wordt de nieuwe plaatsbepalingstechniek getoetst aan gerapporteerde resultaten uit de vakliteratuur. Hieruit blijkt een aanzienlijke verbetering van de nauwkeurigheid in vergelijking met gelijkaardige smalbandige RF systemen.

List of Abbreviations

kNN	k-Nearest-Neighbor. 26, 56
A/D	Analog to Digital. 67
ANN	Artificial Neural Network. 26
AoA	Angle of Arrival. 13, 17
AoD	Angle of Departure. 13
CDF	Cumulative Density Function. 62
CMIM	Conventional Mutual Impedance Method. 79
CSS	Chirp Spread Spectrum. 141
DoA	Direction of Arrival. 13
DSSS	Direct-Sequence Spread Spectrum. 16
ESPRIT	Estimation of Signal Parameters via Rotational Invariance Techniques. 22, 23
FBA	Forward-Backward Averaging. 23, 24
FIR	Finite Impulse Response. 21
GNSS	Global Navigation Satellite System. 1
GO	Geometric Optics. 40
IF	Intermediate Frequency. 68
LBS	Location Based Services. 4
LNA	Low Noise Amplifier. 68
MaMIMO	Massive Multiple Input Multiple Output. 32
MIMO	Multiple Input Multiple Output. 6

MINT	Multipath assisted Indoor Navigation and Tracking. 28
ML	Maximum Likelihood. 22
MUSIC	Multiple Signal Classification. 22
MVDR	Minimum Variance Distortionless Response. 21
NLOS	Non-Line-Of-Sight. 5, 14
OFDM	Orthogonal Frequency Division Multiplexing. 16
PDF	Probability Density Function. 46
RMI	Receiving Mutual Impedance. 80
RMIM	Receiving Mutual Impedance Method. 79, 80
RSS	Received Signal Strength. 7, 12, 14, 137, 138
SDR	Software Defined Radio. 154
SDS-TWR	Symmetric Double-Sided Two Way Ranging. 16
SPDF	Spatial Probability Density Function. 38, 57, 58
SVM	Support Vector Machine. 26
TDoA	Time Difference of Arrival. 12, 15
ToA	Time of Arrival. 12, 15
ToF	Time of Flight. 7, 12, 15, 137, 141
TWR	Two Way Ranging. 12, 16
ULA	Uniform Linear Array. 17
URA	Uniform Rectangular Array. 16
UWB	Ultra Wideband. 3, 16

List of Symbols

$\alpha(t)$	Amplitude of a modulated signal
$\beta(t)$	Phase of a modulated signal
Δh	Material boundary imperfection (m)
Δ	Inter element distance
$\epsilon_{\text{est}}(\theta)$	AoA estimation error
$\eta_m(t)$	Noise signal at antenna m
Γ	Reflection coefficient
$\Gamma_{\perp}$	Transverse electric reflection coefficient
$\hat{\epsilon}_{\text{loc}}$	Normalized localization error
$\hat{}$	Normalization operator
λ	Wavelength
$\mathbb{E}\{\}$	Statistical expectation operator
$\mathcal{T}$	Training data
μ_l	Phase delay of signal $s_l(t)$ between contiguous array elements
μ_r	Relative permeability
$\overline{\hat{P}_{MVDR}}(\theta_{\text{LOS}})$	Mean value of the normalized MVDR spatial spectrum
—	Mean value operator
ϕ_i	Grazing angle
ϕ_r	Reflection angle

ϕ_t	Transmission angle
Π_M	$M \times M$ exchange matrix
$\boldsymbol{\eta}(t)$	Vector of noise signals
$\boldsymbol{A}$	Array manifold
$\boldsymbol{a}(\theta)$	Array steering vector
$\boldsymbol{E}$	Electric field vector
$\boldsymbol{e}_j$	Eigenvectors of $\tilde{\boldsymbol{R}}$
$\boldsymbol{f}$	Fingerprint measurement vector
$\boldsymbol{H}$	Magnetic field vector
$\boldsymbol{I}_L$	$L \times L$ identity matrix
$\boldsymbol{m}$	Measurement vector
$\boldsymbol{p}$	Position vector
$\boldsymbol{R}$	Spatial covariance matrix
$\boldsymbol{r}(t)$	Vector of received signals
$\boldsymbol{R}_\eta$	Spatial covariance matrix of $\boldsymbol{\eta}(t)$
$\boldsymbol{R}_{\text{ss}}$	Spatially smoothed covariance matrix
$\boldsymbol{R}_{\text{sub},k}$	Spatial covariance matrix of subarray k
$\boldsymbol{S}$	Spatial covariance matrix of $\boldsymbol{s}(t)$
$\boldsymbol{s}(t)$	Vector of transmitted signals
$\boldsymbol{w}$	Weight vector
σ_η^2	Noise variance
$\sigma_{\epsilon_{\text{AoA}}}$	Standard deviation of AoA errors
τ	Time of Flight
$\tau_{l,m}$	Additional time delay of signal $s_l(t)$ at array element m
θ_l	AoA of wavefront l
θ_{LOS}	AoA of the LOS signal

$\theta_{\text{refl.}}$	AoA of the reflected signal
$\tilde{\boldsymbol{p}}$	Estimated position
$\tilde{\boldsymbol{R}}$	Estimated spatial covariance matrix
$\tilde{}$	Estimation operator
ε_r	Relative permittivity
*	Complex conjugate operator
^{H}	Hermitian transpose operator
^{T}	Transpose operator
c	Light speed ($3 \cdot 10^8$ m/s)
d	Distance
f_c	Carrier frequency
$G_{\text{Rx}}(\theta)$	Receive antenna gain
$G_{\text{Tx}}(\theta)$	Transmit antenna gain
$h(\theta)$	Filter window $h(\theta)$
$H_m(f_c, \theta)$	Antenna response of element m
I_k	Induced current in antenna element k
$K_{\text{ss,optimal}}$	Optimal amount of spatial smoothing
K_{ss}	Number of spatial smoothing operations
L	Number of impinging wavefronts
L_r	Reflection loss
L_{path}	Path loss
L_{ray}	Power loss of a ray
M	Number of array elements
M_{sub}	Number of subarray elements
N	Number of array snapshots
n	Refractive index

n_{path}	Path loss exponent
N_f	Number of fingerprints
P_{PDF}	Angular probability density function
P_i	Power of an incident wave
P_r	Power of a reflected wave
P_t	Power of a transmitted wave
$P_{\text{PDF,sim}}(\theta)$	Angular PDF from simulated spatial spectra
P_{Rx}	Received power
$P_{\text{sim}}(\theta)$	Discrete or continuous spatial spectrum from multipath simulations
P_{Tx}	Transmitted power
Q	Number of antenna arrays
$r_m(t)$	Received signal at element m
R_t	Mutual resistance
$r_{\text{corr}}(i)$	Pearson correlation coefficient
$r_{\text{dotprod}}(i)$	Dot product
$r_{\text{SPDF}}(i)$	Spatial probability density function
$s_l(t)$	Signal generated by source l
SI	Surface Interval
t	Time
U_k	Induced voltage in antenna element k due to the impinging wavefront
V_k	Induced voltage in antenna element k
W	Width of the window function $h(\theta)$
W_k	Induced voltage in antenna element k due to antenna coupling
X_t	Mutual reactance
$Z_t^{k,i}$	RMI of array element i on element k

Z_{field}	Field impedance
Z_L	Load impedance
Z_{air}	Effective wave impedance of air
Z_{wall}	Effective wave impedance of a wall
ϵ_{loc}	Localization error
P()	Probability operator
P50	50^{th} percentile
P95	95^{th} percentile

Contents

List of Figures

List of Tables

Chapter 1

Introduction

This first chapter forms an introduction to indoor localization and the contributions of this research. Section 1.1 sketches the general principles of localization. A discussion of indoor positioning techniques is provided in Section 1.2, including an overview of possible application domains and their requirements. The current technological challenges, limitations and opportunities are also discussed here. Based on this information, a new localization approach is proposed in Section 1.3. The presented method is reduced to a set of research questions, forming a lead for this work. The topics of the following chapters are summarized in Section 1.4.

1.1 Localization

Positioning or localization can be defined as the process of finding a point in space with respect to a reference system. In ancient Greece and Egypt, coastal landmarks or celestial bodies were used as reference points for marine navigation. The first signs of artificially created reference points for localization even date back to 3000 BC in Mesopotamia [MLVC09]. Present-day Global Navigation Satellite Systems (GNSS) form a modern implementation of this approach. The satellites constitute a network of reference transmitters that enable outdoor localization of a receiver with meter accuracy. Unfortunately, these systems underperform in urban and indoor environments, while some applications even require centimeter accuracy [Ben08].

1.2 Indoor Positioning

In Western society, humans spend approximately 90% of their time indoors [KNO+01]. A significant portion is spent in large buildings that might be unfamiliar (e.g., airports, shopping malls, office buildings, etc.). This creates an application domain for indoor localization systems, tracking persons or objects [LR14]. However, interior environments are characterized by undelimited complex structures, blocking and reflecting signals. The diversity of operating environments and system requirements has led to a multitude of localization systems, which can be classified into three categories according to the underlying technology.

The first type relies on a dedicated infrastructure, specifically transmitting signals for localization. Generally, these systems offer superior accuracy, which comes at a high installation cost. Another category uses 'signals-of-opportunity', exploiting the existing infrastructure (e.g., Wi-Fi, cellular, lighting, etc.) for positioning purposes. This approach features a low setup cost, but hardware limitations typically restrict localization accuracy. The third category comprises all technologies that do not rely on signal transmission (e.g., inertial sensors, vision based systems, etc.). Hybrid systems also exist, combining multiple technologies to achieve a higher localization accuracy [MYTB12].

Signal based systems rely on an infrastructure of fixed reference nodes, transmitting and/or receiving signals. These nodes are often called base stations, anchor nodes or beacons. The device to be localized is commonly denoted as the mobile terminal, mobile node, target or mobile station. Depending on the architecture, this node can be a transmitter as well as a receiver. In these systems, received signal characteristics are measured and converted to parameters that indicate vicinity, distance or direction, eventually leading to a location estimate. Optical, acoustic and Radio Frequency (RF) signals have been explored in a variety of positioning systems for their distinct properties [KH06, Kup05, LDBL07, Mau09, Mei14].

Optical

Optical systems are potentially cheap and theoretically enable a very high localization accuracy, because of the short wavelengths. However, these signals strictly require a Line-Of-Sight (LOS) connection. Invisible light (infra red) systems are mostly implemented in a dedicated infrastructure. In case of a laser based approach, even mm-accuracy can be obtained. Visible light positioning systems can be integrated in visible light communication (VLC) equipment, which classifies this approach as a 'signals-of-opportunity' technology [LSG+16].

The reported localization errors for these systems range between 0.02 m and 0.8 m.

Acoustic

Acoustic positioning also allows low-cost hardware implementations, but has less strict LOS requirements than optical systems. Furthermore, acoustic signals are characterized by a limited propagation speed, facilitating signal acquisition and processing. However, indoor environments are highly reverberant, complicating the localization process. The systems can also be categorized according to perceptibility. Dedicated systems often rely on a combination of ultrasound and RF signals, enabling cm-accuracy. Audible sound setups do not always require dedicated hardware and might even allow positioning of any type of sound source. In this area, localization errors below 0.6 m have been described as feasible [MLG+05].

Radio Frequency

RF technology has experienced a strong evolution towards low-cost, low-power and miniaturized solutions over the past two decades. LOS connections are not strictly required and reverberations are less pronounced than in the acoustic domain. Ultra wideband (UWB) systems represent a common dedicated RF technology, with reported accuracies up to 0.1 m. Another example uses radio frequency identification (RFID), which can result in sub-meter accuracy. The RF 'signals-of-opportunity' category represents the largest group of localization systems. Given the widespread indoor deployment of wireless communication technology (e.g., Wi-Fi, Bluetooth, Zigbee, etc.), RF transmitters and receivers are available abundantly. As a result, existing communication infrastructure is commonly used for indoor positioning purposes, relying on signal strength, delay or direction information. However, the indoor propagation channel is characterized by multipath components, affecting localization performance. As a result, sub-meter accuracy is usually not obtained in commercial systems.

Inertial Measurements and Post Processing Techniques

The common availability of inertial sensors like MEMS accelerometers and gyroscopes in consumer electronics has induced a new type of localization systems. The so-called dead reckoning technique relies on a previous location to determine a new position, based on motion measurements. In order to filter out irregularities in the measurements, extended Kalman filtering can be

applied. Another method for improving travelled path prediction consists of particle filters, relying on Monte Carlo simulations to predict the next position [GART13]. However, these techniques are not solely applicable to inertial measurements. Any type of localization system can be equipped with these 'post processing' techniques to improve tracking accuracy.

1.2.1 Applications and Requirements

Indoor positioning systems form an enabling technology for location aware applications, often referred to as location based services (LBS). The broad field of applications can be divided into distinct categories according to the usage scenario [STK05, Ben08, KH06, Kup05, MLVC09, SGG08]. Table 1.1 summarizes the accuracy requirements for each system category.

Person or asset tracking systems represent a major category with applications in multiple domains. In a medical context, hospital equipment, staff and patients can be tracked. Also in industrial environments and warehouses, inventory and staff are monitored. Other examples are found in wireless handcuffs, tracking systems for elderly people or lost children, and systems for observing person flows at mass events. The gathered information is usually intended for system administrators, enabling the optimization and management of workflows, traffic flows and equipment usage. Also, the systems can be used for retrieving lost assets.

Local information systems are aimed at the mobile user. For instance, advertisements in supermarkets or malls can be location dependent. Another example is found in museums, as specific information on nearby exhibits can be provided. Guidance systems can be considered as a subclass of location based information systems. Similar to outdoor GNSS navigators, people can be guided in large unfamiliar buildings like airports, hospitals, campuses, libraries, malls, event halls, museums etc. Besides people, robots can also be guided indoors. Remark that these applications usually require another class of accuracy and reliability. Examples include automatic guided vehicles in warehouses, and even drones.

In a safety and security context, positioning systems are used for emergency call localization, rescue team positioning, safety zone monitoring and hazardous asset tracking. Access or login systems that require physical presence can also be classified in this category, as well as anti-theft tracking systems.

A last category contains all applications with a focus on entertainment, including location based games, social media, etc. Furthermore, indoor localization plays

a role in the rise of augmented reality and artificial intelligence applications, stimulating innovation in any LBS category.

Table 1.1: Accuracy requirements for different LBS categories (After [SGG08, MLVC09])

LBS category	Accuracy
Tracking	
- People	1 - 10 m
- Assets	0.01 - 20 m
Local information	
- Advertising	5 - 100 m
- Local information	3 - 30 m
Guidance	
- People	1 - 10 m
- Robots	0.01 - 0.1 m
Safety & Security	1 - 20 m
Entertainment	0.1 - 100 m

Table 1.1 roughly represents the accuracy requirements for different applications. However, this is not the only criterion of importance for the selection of an indoor localization system. The broad field of positioning systems is caused by a heterogeneity of requirements, as listed below.

- The robustness indicates whether the system performs consistently in various environments and (adverse) situations (e.g., Non-Line-Of-Sight (NLOS) conditions, multipath, etc.).
- The signaling and computational overhead of the localization system should be minimal in a 'signals-of-opportunity' approach. This limits the burden to the underlying (communication) technology. However, this is often a trade-off with accuracy.
- The power consumption of the nodes can represent a limiting factor in battery powered solutions.
- The latency of localization represents the time for the first position estimation, which is preferably short.
- In some applications, the trustworthiness of position estimates might form a restriction.

- System complexity is mostly related to the price, which is a reason for simplification.
- Roll-out and operating costs represent one of the leading factors. As previously explained, this is a major motivation for choosing a 'signals-of-opportunity' approach.

The variety of indoor positioning systems indicates that no universal approach exists for all requirements. Furthermore, the reported localization accuracies of optical, acoustic and RF systems assume a dense grid of reference nodes and ideal operating conditions. A deviation from these assumptions usually results in a reduced accuracy and can even make localization impossible [MLVC09, Kup05]. A non exhaustive enumeration of possible error sources includes: NLOS connections, multipath propagation, inaccurate clocks, suboptimal base station positions and orientations, as well as medium access problems if positioning runs as a service on top of a communication system. Despite extensive research and development efforts in the past, these error sources form a significant restriction towards practical applicability. However, the combination of challenging requirements, limitations of existing positioning systems and continuous innovations in RF communication systems form an impulse for new research contributions.

1.3 Contributions

Over the past years, widely deployed RF communication systems have gained Multiple Input Multiple Output (MIMO) properties (e.g., 802.11ac [Hoe13], cellular systems [Mol11], etc.). This multi antenna approach will evolve even further to Massive MIMO (MaMIMO) solutions in next generation radio systems [LETM14]. The *antenna arrays in these communication systems could be used for measuring angular signal parameters, allowing the spatial distinction of multipath components.* Previous research has indicated that a distinction of multipath components in the time domain can result in an increased localization accuracy in dedicated UWB setups [Mei14].

This work presents an indoor RF positioning technique, relying on the angular (Angle of Arrival, AoA) information of multipath components, extracted from antenna arrays. The array based solution possibly allows a low cost implementation due to the potential 'signals-of-opportunity' approach and the massive spread of compatible mobile devices. The hypothesis of this research is that an improvement of accuracy and robustness can be obtained over comparable systems, leveraging on AoA measurements of multipath components.

The multipath propagation channel is usually considered as an error source because it disrupts the measurement of LOS signal characteristics. Nevertheless, the proposed localization method aims to exploit this propagation phenomenon to obtain extra spatial information. Therefore, a ray tracing algorithm is used to generate valuable multipath information based on an a-priori known floor plan. The simulated multipath data is then used in a localization algorithm. With this 'multipath assisted' approach, even NLOS connections can contribute to the positioning accuracy instead of causing errors. An extensive evaluation of error sources in different environments allows a further optimization of system parameters. Finally, the proposed system can even be combined with existing RF localization schemes, based on the Received Signal Strength (RSS) or signal Time of Flight (ToF).

In the proposed system, other considered requirements include overhead, latency, power consumption, complexity and cost. These criteria do not constitute the main research focus, but the chosen architecture of the system implies that they can be handled in a favorable way. The computational overhead and latency during operation are reduced by performing the ray tracing simulations in advance, during the setup phase. Furthermore, the system relies on a simple omnidirectional mobile transmitter, and antenna arrays at the infrastructure side, performing receive beamforming. The result is a possible reduction of processing and power requirements of the mobile node, since all processing takes place at the infrastructure side. The complexity of the infrastructure is automatically reduced in comparison to common localization methods because of the multipath assisted approach: since a large number of (multipath) signals is considered by each anchor point, the required number of reference nodes is restricted, even allowing single anchor operation. A reduction of roll-out costs is achieved by the use of a ray tracing simulator: while common systems rely on labor intensive site surveying during setup, multipath simulations form a fast and cost-effective alternative. Other cost limiting factors include the omnipresence of mobile handsets and wireless infrastructure.

The envisioned localization method is primarily aimed at LBS applications that already rely on RF infrastructure. The target improvements include an increased accuracy and NLOS robustness, or a reduced number of anchor nodes. However, the cm or even mm accuracy of dedicated optical or UWB systems is not aspired.

1.3.1 Research Questions

The technological challenges of the proposed localization approach can be distilled to the following set of research questions:

- Is it possible to exploit multipath effects to enhance indoor localization accuracy?
- Can useful multipath information be generated through simulations when floor plan information is available?
- How can simulated multipath information be used in an AoA localization system, and what model accuracy is required?
- Does the proposed approach allow positioning in NLOS situations?
- How do system parameters influence the performance of the system? (e.g., the number of antennas per array, the number of arrays in a room and their geometric organization, the operating frequency, etc.)
- How do environmental factors influence the performance of the system? (e.g., the size of the environment, building materials, etc.)
- Can the multipath assisted AoA method be extended with ToF and RSS techniques in order to increase accuracy?

1.3.2 Research Methods

In order to answer the research questions, a practical and structured approach is adopted, based on theory, related work, simulations and experiments. The followed procedure is reflected by the structure of this book, as expounded in Section 1.4. All presented results are verified by measurements in multiple realistic environments, picturing real-world performance. However, a finished setup with ready-to-use hardware and software is not aspired. This means that measurements are performed with lab equipment, and algorithms are implemented in a Matlab® framework for testing. The goal of the experiments is to evaluate the pure performance of the multipath assisted algorithms. Therefore, the software does not implement travelled path tracking, dead reckoning, Kalman filtering, particle filters, or any other post processing algorithms.

1.4 Outline

The remainder of this text is structured according to the contributions presented in Section 1.3.

Chapter 2: State of The Art: Indoor Radio Frequency Localization provides an overview of indoor RF positioning techniques with a strong focus on AoA

estimation. Also, the related research in the domain of multipath handling is studied.

Chapter 3: Indoor Multipath Assisted Angle of Arrival Localization Method introduces the envisioned multipath assisted indoor positioning system, which relies on ray tracing simulations and AoA estimation techniques. The chapter concludes with a presentation of evaluation criteria for assessing algorithm performance.

Chapter 4: Experimental Setup presents the measurement setup that is used for all testing of the proposed localization system. A synthetic linear antenna array in the 2.4 GHz and 5 GHz bands is described and characterized, followed by a feasibility test of the proposed localization approach.

Chapter 5: System Performance contains an extensive discussion of experimental results in different test scenarios. The chapter starts with an evaluation of the localization algorithms. Next, the influence of hardware parameters is investigated, as well as the impact of the environment.

Chapter 6: Combination of Localization Techniques combines RSS and ToF measurements with the AoA approach. First, RSS and ToF localization is implemented in the existing framework, followed by an assessment of the possible accuracy improvements.

Chapter 7: Conclusions and Future Work recapitulates the most important realizations and findings, followed by a discussion of future research opportunities in the field.

Chapter 2

State of The Art: Indoor Radio Frequency Localization

The conducted research touches on many aspects of the broad field of indoor RF localization. This chapter provides a comprehensive overview of the relevant literature. Section 2.1 gives a high-level overview of existing localization techniques, their requirements and characteristics. The following sections present a further elaboration of the supporting technologies. Section 2.2 explains the basics of RSS localization. Section 2.3 elaborates on ToF based systems and their technological challenges. Section 2.4 contains an extensive overview of AoA estimation techniques, covering the basic theory of phased antenna arrays, parametric and non-parametric AoA estimation algorithms, and preprocessing techniques for signal decorrelation. Next, Section 2.5 explains the properties of a fingerprinting localization approach. Section 2.6 covers the related work, focusing on the state of the art in the specific field of localization in multipath environments. The conclusions of this chapter can be found in Section 2.7.

2.1 Indoor Localization Methods

RF localization systems generally consist of multiple base stations at known locations, and a mobile node with an unknown position [Ben08]. A system is called 'unilateral' or 'handset based' if the mobile device determines its own position based on the received signals from anchor nodes. In 'multilateral' or 'network based' systems, a central processing unit determines the position of the mobile node, based on the signals received by the anchor nodes. The following

sections describe methods for localization on a 2D floor plan, assuming multiple base stations. The presented techniques can be applied in both unilateral and multilateral systems.

Distinction can be made between proximity, range, angle, and fingerprinting based systems [SGG08, MLVC09]. Proximity based (also range-free) systems are considered simple and inexpensive, while offering coarse accuracy. The position of a mobile node in a wireless sensor network is estimated by evaluating which anchor nodes offer a stable connection [HHB+03].

Range and angle based positioning schemes follow a geometric approach for localization, relying on respectively measured distances or angles between a mobile node and the anchor nodes. Distance based localization applies lateration methods to estimate the location of a node. As illustrated in Figure 2.1a, anchor points form the center of a circle, while the measured distances determine the radius. The intersection of all circles indicates the estimated locus. In RF systems, distances can be obtained by measuring the Received Signal Strength (RSS) or Time of Flight (ToF), relying on respectively the declining signal strength or the increasing travel time over distance. In a practical setup, the ToF is usually determined by measuring the Time of Arrival (ToA) at each anchor node, or by performing Two Way Ranging (TWR), which is further explained in Section 2.3. Another ToF-based approach is Time Difference of Arrival (TDoA), a method that is related to ToA but does not require clock synchronization of the mobile node with the base stations. TDoA systems only provide information about distance differences. This relative information results in a geometric localization technique of intersecting hyperbolas, as depicted in Figure 2.1b. One hyperbole can be conceived for each combination of two anchor nodes, with these nodes as focus points.

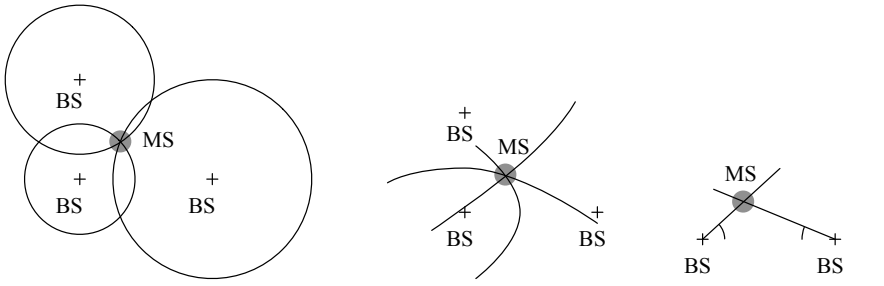

(a) Distance information (b) Distance differences (c) Angular information

Figure 2.1: Geometric localization of a mobile station (MS) with multiple base stations (BS) on a 2D floor plan

In angulation based geometric localization systems, signal directions are represented as straight lines, which is depicted in Figure 2.1c. The intersection of these lines indicates the location of the node. Angular systems require anchor nodes and/or the mobile node to be equipped with multiple antennas in order to estimate signal directions. Direction of Arrival (DoA) systems measure the directions of received signals at the base station side. In a 3D environment, these directions are defined by an azimuth and elevation angle, which is illustrated in Figure 2.2.

In a simplified approach for 2D operation, the term 'Angle of Arrival' (AoA) is used, estimating angles in a single plane. However, this 2D simplification represents a possible source of positioning errors. For angulation, azimuth angles are usually required. However, linear phased antenna arrays, commonly used for AoA estimation, measure broadside angles [Ben08]. The difference between broadside and azimuth angles should not be disregarded. As illustrated by Figure 2.2, the azimuth angle is always measured in the xy-plane, between the x-axis and the orthogonal projection of the DoA in the xy-plane. The broadside angle is measured in a variable plane, between the DoA and its orthogonal projection in the xz-plane. As a result, broadside and azimuth angles are only equal for 0° elevation. A cone surface around the y-axis groups all possible DoAs with the same broadside angle, illustrating the remaining degrees of freedom when a broadside angle has been measured.

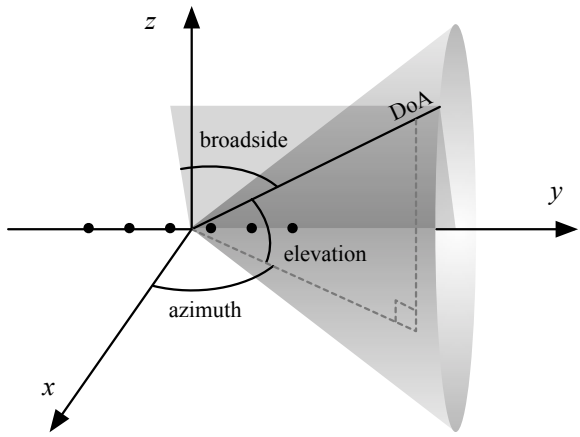

Figure 2.2: Azimuth, elevation and broadside angle for a certain DoA

The Angle of Departure (AoD) method is a less common approach for angular localization. The process requires control of transmit directions, aiming beams in certain directions and evaluating the response at the receivers. The AoD

approach is often combined with DoA techniques in systems where mobile nodes and anchor nodes are equipped with antenna arrays.

An important drawback of RF positioning systems lies in their susceptibility to indoor multipath effects such as reflections, scattering, diffraction, refraction and absorption, especially in NLOS conditions when shadowing occurs [STK05, Bar03, MLVC09]. The effects cause fluctuations in RSS values due to destructive or constructive interference. Also the ToF and DoA parameters can be influenced when the propagation path is altered. The multipath phenomena are usually considered as random events in geometric localization systems. Their influence is mostly reduced by averaging, filtering or redundancy.

Fingerprinting techniques are widely applied in real-world situations because the detrimental effects of the environment on signal characteristics can be taken into account, limiting localization errors [KH06]. This method consists of an offline phase, in which a reference dataset is built from surveyed signal characteristics at known positions. In the online phase, measurement data is matched to the reference dataset, leading to an estimated position. In most fingerprinting systems, RSS data is used because this parameter is readily available in wireless communication systems, requiring no further hardware investments. A major drawback of fingerprinting lies in the labor intensive offline survey phase. Also, the technique is susceptible to changes in the environment, which alter the propagation channel.

2.2 Received Signal Strength

RSS localization schemes are widely applied in wireless communication systems because they require no extra hardware, bandwidth or energy, making the implementation simple and low-cost. The received power P_{Rx} is expressed in Equation 2.1 as a function of the transmitted power P_{Tx}, the gains of transmitting and receiving antenna $G_{\mathrm{Tx}}(\theta)$ and $G_{\mathrm{Rx}}(\theta)$, and the path loss L_{path} [Ben08]. True antenna gains are always direction (θ) dependent, however isotropic radiation patterns are pusued since the DoA is unknown in RSS systems.

$$P_{\mathrm{Rx}}[\mathrm{dBm}] = P_{\mathrm{Tx}}[\mathrm{dBm}] + G_{\mathrm{Tx}}(\theta)[\mathrm{dB}] + G_{\mathrm{Rx}}(\theta)[\mathrm{dB}] - L_{\mathrm{path}}[\mathrm{dB}] \tag{2.1}$$

With the values of P_{Tx}, $G_{Tx}(\theta)$ and $G_{Rx}(\theta)$ assumed to be known, the path loss value can be calculated. This parameter can be used for localization purposes, given the relationship between the path loss and the travelled distance. This is expressed by the Friis path loss model in Equation 2.2, which is a function of

travelled distance d, wavelength λ and a path loss exponent n_{path} [Fri46]. In free space situations, the path loss exponent has a value of $n = 2$.

$$L_{\text{path}} = -10 \cdot \log_{10} \left(\frac{\lambda}{4\pi d} \right)^{n_{\text{path}}} \tag{2.2}$$

However, due to fading effects in indoor environments, signal strengths tend to decrease quicker than described by the free space model. Therefore, practical values for the path loss exponent range between 2 and 5 [MLVC09, PAK+05]. The exact value depends on the environment and can be determined in site surveys. In favorable circumstances, signals can add constructively, even resulting in $n_{\text{path}} < 2$ values. This happens in indoor LOS situations, creating a waveguide effect, as demonstrated in [APV+13]. The travelled distance can be estimated by isolating d from the Friis equation, resulting in Equation 2.3. The distance estimates usually deliver a coarse accuracy, as path loss models provide only generalized predictions of the received signal strength [SGG08]. In realistic situation, site-specific multipath effects, shadowing, antenna polarizations and changes in the environment will decrease performance.

$$d = \frac{\lambda}{4\pi} \cdot 10^{L_{\text{path}}/10n_{\text{path}}} \tag{2.3}$$

2.3 Time of Flight

ToF based systems rely on the finite propagation speed of electromagnetic waves ($c = 3 \cdot 10^8$ m/s) in order to calculate a distance, as simply expressed by Equation 2.4, where τ denotes the travel time of the signal (the ToF) [Ben08].

$$d = c \cdot \tau \tag{2.4}$$

In order to measure τ, different technical solutions are available. In ToA systems, all anchor nodes and the mobile node have synchronized clocks. When the time of transmission and time of arrival at each anchor node is available, distances can easily be computed. However, the perfect synchronization of clocks is critical and challenging: a clock error of 1 ns represents a 0.30 m deviation.

TDoA systems relieve the technical burden of synchronizing the mobile node with the rest of the system. Only the fixed anchor nodes are synchronized, so no time of transmission is known in this layout. However, localization is still

possible with multiple anchor nodes, as the time differences of arrival are known, resulting in the hyperbolic localization approach of Figure 2.1b.

A third technical solution for ToF based localization is called Two Way Ranging (TWR) [KPGT10]. When the mobile node transmits a signal, it starts a timer. A second node receives this signal and after a known fixed delay, answers with a retransmission of this signal. When the mobile node receives the retransmission, the timer is stopped and the ToF can be calculated. This approach requires no synchronization, because the time of transmission and time of arrival are measured at the same node. A variation on this technique is Symmetric Double-Sided Two Way Ranging (SDS-TWR), where ToF information is calculated at the initiating node and the responding node. Both results are exchanged and averaged, reducing the influence of clock drift errors and resulting in an improved accuracy [KC10].

2.3.1 Ultra Wideband

ToF based systems often rely on UWB signals, which have a minimum bandwidth of 500 MHz or 20% of the carrier frequency [SGG08]. Different signal shapes can be used to exploit the bandwidth: narrow pulses, chirps and DSSS or OFDM signals. Due to the large bandwidth, propagation channels can be measured at multiple frequencies with different propagation characteristics, which reduces the multipath damage, improving the direct link quality. Even if multipath components are received, the LOS connection can usually be isolated as it represents the shortest ToF, even with a reduced signal strength. Also, the large bandwidth provides a high time resolution, allowing an accurate detection of start and stop timer events in ranging systems. As a result of these favorable characteristics, cm-accuracy can be obtained in UWB ranging systems [SGG08].

2.4 Angle of Arrival Estimation

Angular estimation systems rely on antenna arrays and phase processing. The organization of multiple antennas (i.e. array elements) results in phase delays, which can be used for calculating signal directions. For 3D DoA estimation, the array elements can be arranged on a 2D surface or even in a 3D configuration. When all elements are placed in a rectangular configuration with equal inter-element spacing, it is called a Uniform Rectangular Array (URA). 3D configurations (e.g., spherical, cylindrical, etc.) are denoted as conformal arrays. However, antennas can also be arranged in a 1-dimensional manner, enabling the estimation of broadside angles, as depicted in Figure 2.2. A Uniform Linear

Array (ULA) is equipped with multiple equally spaced antennas along a line as depicted in Figure 2.3.

2.4.1 Uniform Linear Phased Antenna Arrays

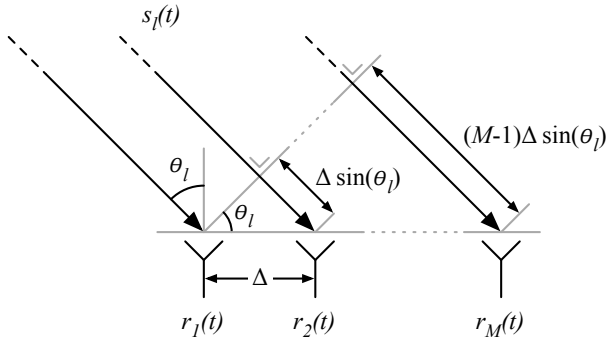

Figure 2.3: Theoretical ULA system model

This section aims to provide a comprehensive and straight-forward discussion of AoA estimation theory, based on the profound work of [VT05, MLVC09, CGY10]. The schematic representation of the array depicts M antennas with an inter-element distance Δ. L wavefronts $s_l(t)$ ($l \in \{1, \ldots, L\}$) impinge on the array under an angle θ_l ($\theta_l \in [-90°, 90°]$, i.e. the angle of arrival), resulting in the received signals $r_m(t)$ ($m \in \{1, \ldots, M\}$). In the further theoretical discussion, uncorrelated sources are assumed, generating planar wavefronts (i.e. signals travel in parallel). This condition is fulfilled when signal sources are located in the far field, as expressed by Equation 2.5. This rule-of-thumb expression depends on the array size $\Delta(M-1)$ and the wavelength λ. Furthermore, the medium is assumed to be isotropic and linear, allowing linear superpositions of signals.

$$d > \frac{2[\Delta(M-1)]^2}{\lambda} \tag{2.5}$$

When a wavefront impinges on the array, it hits the first antenna ($m = 1$) after the ToF τ_l. The signal arrives at the other antennas with additional time delays $\tau_{l,m}$ due to the longer distance travelled for each consecutive element in the array, which is described by Equation 2.6. These time delays result in phase differences μ_l between contiguous elements, as expressed by Equation 2.7. f_c represents the carrier frequency of the system, which is assumed to be smallband.

This means for the (modulated) signals $s_l(t)$ that the phase $\beta_l(t)$ and amplitude $\alpha_l(t)$ changes slowly when traveling from one array element to another, as expressed by $\alpha_l(t) \approx \alpha_l(t - \tau_{l,m})$ and $\beta_l(t) \approx \beta_l(t - \tau_{l,m})$.

$$\tau_{l,m} = (m-1)\Delta \sin(\theta_l) \tag{2.6}$$

$$\mu_l = \frac{2\pi f_c}{c}\Delta \sin(\theta_l) = \frac{2\pi}{\lambda}\Delta \sin(\theta_l) \tag{2.7}$$

$$s_l(t) = \alpha_l(t - \tau_l)e^{j[2\pi f_c(t-\tau_l)+\beta_l(t-\tau_l)]} \tag{2.8}$$

The phase differences μ_l are measured and used to determine the values of θ_l. Therefore, unambiguous phase information is needed, leading to the requirement $|\mu_l| \leq \pi$, which assures a one-on-one relationship between μ_l and θ_l. Substituting this condition in Equation 2.7 results in the requirement $\Delta \leq \lambda/2$. When inter-element spacing is larger than $\lambda/2$, phase ambiguities are introduced, reducing the field of view of the array. In this case, grating lobes can be observed in the array response pattern. Usually, the $\lambda/2$ spacing is adopted, as smaller values stimulate practical problems like antenna coupling and small scale fading. Furthermore, it must be noted that $\theta_l \in \{-90, -89, \ldots, 0, \ldots, 89, 90\}$ results in the same phase differences μ_l as $\theta_l \in \{-90, -91, \ldots, 180, \ldots, 91, 90\}$. This means that a ULA cannot distinguish the frontside from the backside of the array.

The received signal at antenna element m is described in Equation 2.9, with $H_m(f_c, \theta_l)$ representing the m-th antenna response and $\eta_m(t)$ being the noise at element m. The noise is assumed to be white and gaussian with a zero mean and variance σ_η^2. It is not correlated with $s_l(t)$ and there is no noise correlation between array elements.

$$r_m(t) = \sum_{l=1}^{L} H_m(f_c, \theta_l)s_l(t)e^{-j(m-1)\mu_l} + \eta_m(t) \tag{2.9}$$

$H_m(f_c, \theta_l)e^{-j(m-1)\mu_l}$ is defined as the m-th element of the array steering vector $\boldsymbol{a}(\theta)$ in Equation 2.10, representing the array response to an impinging signal under an angle θ. In most configurations all array elements are equal. Furthermore, antenna coupling is omitted in this simplified theoretical approach, resulting in a single antenna response $H(f_c, \theta)$, which simplifies Equation 2.10 to Equation 2.11. The array outputs for L signals $s_l(t)$ are expressed in Equation 2.12, relying on the linear nature of the medium.

$$\boldsymbol{a}(\theta_l) = [H_1(f_c, \theta_l) \quad H_2(f_c, \theta_l)e^{-j\mu_l} \quad \dots \quad H_M(f_c, \theta_l)e^{-j(M-1)\mu_l}]^T \tag{2.10}$$

$$\boldsymbol{a}(\theta_l) = H(f_c, \theta_l)[1 \quad e^{-j\mu_l} \quad \dots \quad e^{-j(M-1)\mu_l}]^T \quad {\scriptstyle H(f_c,\theta)=H_1(f_c,\theta)=\ldots=H_M(f_c,\theta)} \tag{2.11}$$

$$\begin{bmatrix} r_1(t) \\ r_2(t) \\ \vdots \\ r_M(t) \end{bmatrix} = [\boldsymbol{a}(\theta_1) \quad \boldsymbol{a}(\theta_2) \quad \dots \quad \boldsymbol{a}(\theta_L)] \begin{bmatrix} s_1(t) \\ s_2(t) \\ \vdots \\ s_L(t) \end{bmatrix} + \begin{bmatrix} \eta_1(t) \\ \eta_2(t) \\ \vdots \\ \eta_M(t) \end{bmatrix} \tag{2.12}$$

In matrix notation, this is reduced to Equation 2.13, with $\boldsymbol{A}$ denoting the array manifold, i.e. a collection of L steering vectors, defining the array response to all impinging wavefronts. The values of $\boldsymbol{A}$ can be determined analytically or in calibration measurements.

$$\boldsymbol{r}(t) = \boldsymbol{A}\boldsymbol{s}(t) + \boldsymbol{\eta}(t) \tag{2.13}$$

The received signals $\boldsymbol{r}(t)$ contain uncorrelated noise and correlated signal components, originating from the same signal sources. This property can be exploited for the extraction of AoA information. Therefore, the spatial covariance matrix $\boldsymbol{R}$ is introduced, as expressed in Equation 2.14. $\mathbb{E}\{\}$ denotes the statistical expectation operator, while $\boldsymbol{S}$ and $\boldsymbol{R}_\eta$ represent the spatial correlation matrices of $\boldsymbol{s}(t)$ and $\boldsymbol{\eta}(t)$.

$$\begin{aligned} \boldsymbol{R} = \mathbb{E}\left\{\boldsymbol{r}(t)\boldsymbol{r}(t)^H\right\} &= \boldsymbol{A}\boldsymbol{S}\boldsymbol{A}^H + \boldsymbol{R}_\eta \\ &= \boldsymbol{A}\boldsymbol{S}\boldsymbol{A}^H + \sigma_\eta^2 \boldsymbol{I}_L \end{aligned} \tag{2.14}$$

In real-world systems, $\boldsymbol{R}$ will always be calculated from N array snapshots over time, resulting in the estimated spatial covariance matrix $\tilde{\boldsymbol{R}}$.

$$\boldsymbol{R} \approx \tilde{\boldsymbol{R}} = \frac{1}{N}\sum_{t=1}^{N} \boldsymbol{r}(t)\boldsymbol{r}(t)^H \tag{2.15}$$

2.4.2 Non-Parametric AoA Estimation Algorithms

In order to estimate the θ_l values, different AoA estimation algorithms are available, which can be classified as parametric or non-parametric. In non-parametric algorithms, sometimes referred to as quadratic algorithms, no assumptions are made about the statistical properties of the signals. The estimation of signal directions is performed by steering the beam electronically over all directions and measuring the output power of the beamformer. This results in a 'spatial periodogram' $|y(t)|^2$, as defined by Equation 2.16. The N-snapshot average of the periodogram is a 'spatial spectrum', which is a curve that indicates the received power $P(\theta)$ as a function of the steering direction θ. The peaks in this spectrum indicate the estimated values of θ_l. Steering the beam of the array is done by linearly combining all antenna signals with a complex weight vector $\boldsymbol{w}$, as expressed in Equation 2.16. In order to determine the values of the weight vector, knowledge of the array steering vectors $\boldsymbol{a}(\theta)$ is required.

$$|y(t)|^2 = \left|\boldsymbol{w}^H \boldsymbol{r}(t)\right|^2 \tag{2.16}$$

$$\begin{aligned} P(\theta) &= \frac{1}{N}\sum_{t=1}^{N} |y(t)|^2 \\ &= \frac{1}{N}\sum_{t=1}^{N} \boldsymbol{w}^H \boldsymbol{r}(t)\boldsymbol{r}(t)^H \boldsymbol{w} \\ &= \boldsymbol{w}^H \tilde{\boldsymbol{R}} \boldsymbol{w} \end{aligned} \tag{2.17}$$

Beamscan

The beamscan algorithm or 'conventional beamformer' uses weight vectors that maximize the power output for the steered direction by constructively adding all received signals. This is achieved by using normalized steering vectors as weights, as presented in Equation 2.18. The resulting spatial spectrum is described by Equation 2.19.

$$\boldsymbol{w}_{BS}(\theta) = \frac{\boldsymbol{a}(\theta)}{\sqrt{\boldsymbol{a}(\theta)^H \boldsymbol{a}(\theta)}} \tag{2.18}$$

$$P_{BS}(\theta) = \frac{\boldsymbol{a}(\theta)^H \tilde{\boldsymbol{R}} \boldsymbol{a}(\theta)}{\boldsymbol{a}(\theta)^H \boldsymbol{a}(\theta)} \tag{2.19}$$

The beamscan algorithm exhibits limited computational complexity, and performs well in the case of a single impinging signal. However, the algorithm shows poor resolution when signals impinge from multiple directions, particularly when they are correlated (e.g., in multipath environments).

MVDR

The Minimum Variance Distortionless Response (MVDR) algorithm, also known as the Capon beamformer, applies a different approach. The focus of this algorithm is not on power maximization in the looking direction, but on minimization of average power ($\mathbb{E}\left\{|y(t)|^2\right\}$) while maintaining unity response in the looking direction ($\boldsymbol{w}^H \boldsymbol{a}(\theta) = 1$) [God97]. The resulting weight vector $\boldsymbol{w}$ is described in Equation 2.20, while the spatial spectrum $P_{MVDR}(\theta)$ is expressed by Equation 2.21.

$$\boldsymbol{w}_{MVDR}(\theta) = \frac{\tilde{\boldsymbol{R}}^{-1} \boldsymbol{a}(\theta)}{\boldsymbol{a}(\theta)^H \tilde{\boldsymbol{R}}^{-1} \boldsymbol{a}(\theta)} \tag{2.20}$$

$$P_{MVDR}(\theta) = \frac{1}{\boldsymbol{a}(\theta)^H \tilde{\boldsymbol{R}}^{-1} \boldsymbol{a}(\theta)} \tag{2.21}$$

This algorithm achieves superior AoA estimation performance because the sidelobes of the beamformer are reduced in comparison to the beamscan algorithm. This assures better performance when multiple signals impinge on the array, but it comes at the cost of a higher computational load. In spite of the increased overall performance, this beamforming algorithm still underperforms when signal sources are correlated.

An interesting remark with respect to AoA estimation algorithms is their resemblance to frequency spectral estimators [Hay96, SM05]. In this analogy, μ_l is called the 'spatial frequency' and the inter-element spacing requirement $\Delta \leq \lambda/2$ can be linked to the Nyquist sampling theorem in the time domain. More interestingly, the weight vectors $\boldsymbol{w}$ can be considered as filter weights in the spatial domain, in analogy to Finite Impulse Response (FIR) filter coefficients in the time domain. For the beamscan algorithm, filter weights only depend on $\boldsymbol{a}(\theta)$. Since this is a known parameter, the shape and bandwidth of the filter can

be determined. In the MVDR algorithm however, weights are also determined by $\tilde{\boldsymbol{R}}$. This means that the shape of the filter depends on the received signals (cfr. adaptive filters).

2.4.3 Parametric AoA Estimation Algorithms

In parametric estimators, assumptions are made about the statistical characteristics of the received signals. An illustrative example is the maximum likelihood (ML) AoA estimator, assuming the signal model from Equation 2.13 to estimate θ_l and $\boldsymbol{s}(t)$ parameters, as expressed in Equation 2.22.

$$\left\{\tilde{\theta}_l, \tilde{\boldsymbol{s}}(t)\right\} = \arg \min_{\tilde{\theta}_l, \tilde{\boldsymbol{s}}(t)} \left\{\|\boldsymbol{r}(t) - \boldsymbol{A}(\tilde{\theta}_l)\tilde{\boldsymbol{s}}(t)\|^2\right\}_N \tag{2.22}$$

However, the ML estimator reportedly exhibits suboptimal performance and a high complexity. Another type of parametric algorithms consists of subspace-based or super-resolution estimators. These algorithms exploit the eigenstructure properties of the covariance matrix $\tilde{\boldsymbol{R}}$ to divide this matrix in two orthogonal subspaces. The part with the highest eigenvalues is defined as signal subspace and contains the steering vectors, while the lowest eigenvalues represent the noise subspace. The Multiple Signal Classification (MUSIC) and the Estimation of Signal Parameters via Rotational Invariance Techniques (ESPRIT) algorithms are most frequently used, reportedly offering good performance and low computational complexity.

Multiple Signal Classification

The MUSIC algorithm performs AoA estimation by checking the orthogonality of steering vectors (in signal subspace) to noise subspace [SPK86]. An impinging signal at a certain angle results in orthogonality and a peak of the pseudo spatial spectrum, which is defined in Equation 2.23. $\boldsymbol{e}_j$ represents the eigenvectors of $\tilde{\boldsymbol{R}}$, ranked according to their decreasing eigenvalues, so the signal subspace is constituted by $\boldsymbol{e}_j$ for $j \in \{1, \ldots, L\}$. L denotes the number of impinging signals and M is the number of antenna elements. $P_{MUSIC}(\theta)$ is considered a pseudo spectrum, because it does not represent the actual received power as a function of θ. Instead, this curve theoretically peaks to infinity for each AoA, as the denominator reaches 0.

$$P_{MUSIC}(\theta) = \frac{\boldsymbol{a}(\theta)^H \boldsymbol{a}(\theta)}{\sum_{j=L+1}^{M} [\boldsymbol{a}(\theta)^H \boldsymbol{e}_j]^2} \tag{2.23}$$

A variation of this method is the root MUSIC algorithm, which estimates peaks in the MUSIC pseudo spatial spectrum by calculating the roots of the spectrum polynomial instead of calculating the complete spectrum, which is an easier operation from a computational point of view [HAGY08]. Although MUSIC is a so-called super-resolution algorithm, it is known to seriously underperform when received signals are correlated. Signal correlation (e.g., in multipath environments) decreases the number of large eigenvalues, complicating the detection of noise subspace and resulting in a failing algorithm. Accurate results can only be expected at high SNR values, no signal correlation and clearly separated angles. Furthermore, steering vectors are supposed to be known, making a practical solution susceptible to calibration errors.

Estimation of Signal Parameters via Rotational Invariance Techniques

The ESPRIT algorithm requires a translational invariant antenna array that consists of two identical subarrays. This gives rise to a rotational invariant signal subspace and eliminates the need for accurate calibration. For the AoA estimation, no spatial spectrum is calculated, but an invariance equation is formulated and solved, resulting in a set of eigenvalues that is used for the calculation of estimated AoA values [RK89]. A more in-depth elaboration of the algorithm can be found in [VT05, CGY10, MLVC09]. ESPRIT performance is comparable to MUSIC and also suffers from correlated signals, but less array snapshots are required and it is computationally less complex than MUSIC since no spatial pseudospectrum is calculated.

2.4.4 Signal Decorrelation

The performance of AoA estimation algorithms is negatively impacted by correlated signal sources. This can be explained intuitively because the algorithms rely on the correlation between the channels of the array. A more underpinned explanation is based on Equation 2.14. In order to estimate the angles of L impinging signals, $\boldsymbol{R}$ is required to have rank L. This means that $\boldsymbol{S}$ should be diagonal and singular, a condition that is only fulfilled when the L signal sources are uncorrelated. In case of slight correlation between all signals or high correlation between two or more signals, the rank of the spatial covariance matrix will be less than L, resulting in AoA estimation errors. For Q highly correlated waveforms, $\boldsymbol{R}$ will have rank $L - Q$. This condition deserves particular attention in multipath environments, where multiple signals originate from the same source and are consequently correlated. This problem can be treated with signal decorrelation techniques like Forward-Backward Averaging (FBA) or Spatial Smoothing.

Forward-Backward Averaging

The FBA preprocessing technique is only applicable in symmetrical antenna arrays (a ULA for example). This method relies on the fact that steering vectors remain the same when their order is reversed and their values are complex conjugated. Using this property, a backward spatial covariance matrix can be defined as in Equation 2.24, with Π_M denoting an $M \times M$ exchange matrix (anti-diagonal matrix of ones).

$$\boldsymbol{R}_{\text{back}} = \Pi_M \boldsymbol{R}^* \Pi_M \tag{2.24}$$

Forward-backward averaging is achieved by averaging the spatial covariance matrix with its backward counterpart, as expressed by Equation 2.25. For an N-snapshot approximation, Equation 2.26 is used.

$$\boldsymbol{R}_{\text{fb}} = \frac{1}{2}\left(\boldsymbol{R} + \boldsymbol{R}_{\text{back}}\right) \tag{2.25}$$

$$\tilde{\boldsymbol{R}}_{\text{fb}} = \frac{1}{2N}\sum_{t=1}^{N}\left(\boldsymbol{r}(t)\boldsymbol{r}(t)^H + \Pi_M[\boldsymbol{r}(t)\boldsymbol{r}(t)^H]^*\Pi_M\right) \tag{2.26}$$

In case of correlated signals, this manipulation achieves one decorrelation, resulting in an increased rank of $\tilde{\boldsymbol{R}}_{\text{fb}}$.

Spatial Smoothing

Another solution consists of spatial smoothing, a preprocessing technique for signal decorrelation that divides the array into $K_{\text{ss}} + 1$ subarrays containing $M_{\text{sub}} = M - K_{\text{ss}}$ elements, each with a separate spatial covariance matrix $\boldsymbol{R}_{\text{sub},k}$, as illustrated by Figure 2.4. A new spatially smoothed spatial covariance matrix $\boldsymbol{R}_{\text{ss}}$ can be obtained by averaging the spatial correlation matrices of the subarrays as presented in Equation 2.27. The result is a spatial covariance matrix $\boldsymbol{R}_{\text{ss}}$ with rank L, assuming that the array is equipped with a sufficient number of elements M. This assumption is supported by Equation 2.28, expressing the relation between the required number of array elements (M), the number of spatial smoothing operations (K_{ss}) and the number of signals that is to be detected (L). From a different perspective, the number of detectable signals (L) can be expressed for a given number of elements (M).

$$\boldsymbol{R}_{\mathrm{ss}} = \frac{1}{K_{\mathrm{ss}}+1} \sum_{k=1}^{K_{\mathrm{ss}}+1} \boldsymbol{R}_{\mathrm{sub},k} \tag{2.27}$$

$$\begin{aligned} M &\geq L + K_{\mathrm{ss}} + 1 \\ L &\leq M - K_{\mathrm{ss}} - 1 \end{aligned} \tag{2.28}$$

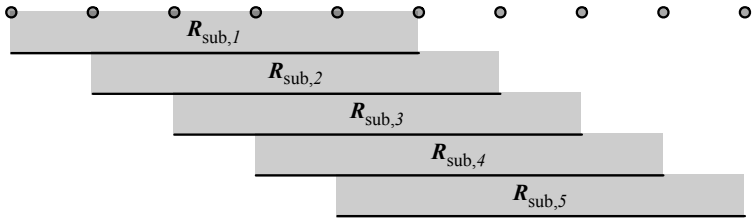

Figure 2.4: Spatial smoothing example for $K_{\mathrm{ss}} = 4$, $M_{\mathrm{sub}} = 6$ and $M = 10$

In case of correlated signals, spatial smoothing enhances the rank of the spatial covariance matrix by K_{ss}. Due to the averaging of subarrays, the number of available snapshots increases from N to $N(K_{\mathrm{ss}}+1)$. However, the array aperture decreases to M_{sub}, limiting the number of detectable signals. Therefore, the amount of spatial smoothing operations K_{ss} will always be a trade-off between the array aperture (the number of detectable signals) and the number of signal decorrelations. This contrasts with the FBA technique, which does not affect the array aperture, but performs only one signal decorrelation.

2.5 Fingerprinting

A fingerprinting (also called 'mapping') localization scheme applies a direct localization approach, as input vectors are directly mapped to a location with a set of training data $\mathcal{T}$ [SGG08]. Equation 2.29 represents this data set, with fingerprint vectors $\boldsymbol{f}_i$ for position vectors $\boldsymbol{p}_i = (x_i, y_i)$, where i represents the data point index ($i \in \{1, \ldots, N_f\}$).

$$\mathcal{T} = \left\{ (\boldsymbol{f}_1, \boldsymbol{p}_1), (\boldsymbol{f}_2, \boldsymbol{p}_2), \ldots, (\boldsymbol{f}_{N_f}, \boldsymbol{p}_{N_f}) \right\} \tag{2.29}$$

In order to estimate the position $\boldsymbol{p}$ for a measurement $\boldsymbol{m}$, pattern matching algorithms are used. In the simplest approach, the position estimate $\tilde{\boldsymbol{p}}_{\mathrm{1NN}}$ equals

position $\boldsymbol{p}_j$, where j satisfies Equation 2.30. The match is defined as the point with the closest match between the measurement vector $\boldsymbol{m}$ and the training data $\boldsymbol{f}_i$. In an RSS fingerprinting system, this is often represented as the closest euclidean distance between both RSS vectors: $\|\boldsymbol{m} - \boldsymbol{f}_i\|$. However, different approaches are possible and different signal characteristics can be considered.

$$j = \arg \min_{i \in \{1,\ldots,N_f\}} \|\boldsymbol{m} - \boldsymbol{f}_i\| \tag{2.30}$$

The k-Nearest-Neighbor (kNN) algorithm is a frequently used method that reportedly achieves very good performance when reference data is distributed uniformly across the area [SL15]. This method elaborates on Equation 2.30: instead of only relying on the closest match, the k closest matches in $\mathcal{T}$ are considered, with k being an empirically chosen number. As formulated in Equation 2.31, the estimated position $\tilde{\boldsymbol{p}}_{k\mathrm{NN}}$ represents a weighted average of the k closest matches $\tilde{\boldsymbol{p}}_1, \tilde{\boldsymbol{p}}_2, \ldots, \tilde{\boldsymbol{p}}_k$. Weighting factors can be chosen as a function of measurement results, but also uniform distributions are possible, among others [MPV03]. Since the resulting position $\tilde{\boldsymbol{p}}_{k\mathrm{NN}}$ is an average of training data positions, this method is not restricted to the resolution of training points, in contrast to $\tilde{\boldsymbol{p}}_{1\mathrm{NN}}$.

$$\tilde{\boldsymbol{p}}_{k\mathrm{NN}} = \sum_{n=1}^{k} w_n \tilde{\boldsymbol{p}}_n \tag{2.31}$$

Besides the kNN approach, Support Vector Machines (SVM) and Artifical Neural Networks (ANN) can be used in fingerprinting localization systems. The SVM approach maps the measurements to a higher-dimensional feature space in order to perform linear regression. In contrast to the kNN approach, this results in a non-linear regression in the original space. The ANN method is a machine learning approach in software that resembles the operation of a biological brain, mapping input vectors to outputs with the help of so-called neurons [YLAU11]. Comparisons of fingerprinting methods generally indicate very good performance of the straight-forward kNN approach [ZLS+13]. Variations also exist in the type of input data, the amount of required training samples and the computational complexity.

2.6 Related Work

Chapter 1 introduced a new multipath assisted localization approach, which was reduced to a set of research questions. However, these questions have

captivated many researchers in the past, elaborating a variety of solutions in pursuit of improved accuracy and robustness in indoor localization systems. This section specifically discusses recent and related contributions from literature, covering AoA estimation in general, multipath and NLOS handling, single anchor node localization systems, fingerprinting and the combination of localization techniques.

2.6.1 AoA

As explained in Section 2.4, standard AoA localization systems consist of multiple anchor nodes and use triangulation of LOS signals to determine the position of a mobile node. Recent research in this area focuses on system implementation issues, such as the minimization of the computational load [SDB07] and reducing the impact of system imperfections on localization accuracy [BHH+12]. The systems are generally deployed in well defined LOS situations, such as satellite based localization or an open indoor area. In [ACD+11], a classical LOS triangulation based AoA system is presented. Three 868 MHz 3-element arrays are used for the localization of a mobile node in a 3 m x 3 m area, resulting in an average localization error of 0.26 m.

When the straight-forward LOS triangulation approach is applied in multipath or NLOS situations, localization accuracy can be heavily affected due to erroneous AoA estimation of the LOS components. Various techniques have been proposed to tackle this issue, including multipath mitigation, multipath exploitation and fingerprinting.

2.6.2 Multipath and NLOS Mitigation

Multipath signals are mostly treated as error sources that should be detected and mitigated. Most NLOS handling algorithms rely on statistical methods. As NLOS signals generally do not match the expected LOS characteristics, these situations can be statistically detected and treated as outliers. In the time domain, this approach only works for occasional NLOS connections [CZ05]. An approach in the spatial domain is proposed in [Che99], using redundant anchor nodes. If a NLOS connection is detected, it is excluded from the positioning algorithm. A similar method is used in [GAMD04], performing triangulation in a cellular network with only the two most probable LOS connections.

Garcia et al. proposes a narrowband AoA localization system for outdoor use in MaMIMO communication systems with multiple base stations [GWL+17]. The NLOS problem is tackled by a direct localization approach called ‘Direct Source

Localization' (DiSouL): instead of performing triangulation with the strongest signals, all received multipath components are processed by a 'fusion center' that determines the LOS directions, leading to an estimated position through triangulation. For NLOS situations, this means that very weak LOS signals can be used in a triangulation algorithm, even when stronger NLOS components exist. In an outdoor scenario with synthetic data, the system exhibits superior performance over the classical triangulation approach, achieving sub-meter accuracy in favorable conditions (SNR over 10dB, over 80 array elements).

[hFnLcL08] presents an RSS fingerprinting system that performs a multipath effect reduction on measurement results before estimating the position of a user. The technique is demonstrated in a 24.6 m x 17.6 m environment, presenting a significant improvement of localization accuracy over a standard RSS fingerprinting approach. Absolute localization errors heavily depend on the number of anchor nodes: mean errors range from 6.4 m to 0.5 m for respectively 1 to 8 anchor nodes.

2.6.3 Multipath Assisted Localization

Most indoor localization systems consider multipath components as undesirable because they introduce localization errors. However, these components contain spatial information that can be exploited, a feature that is explored in multipath assisted localization systems.

Meissner et al. developed a system for multipath assisted indoor navigation and tracking (MINT), which can currently be considered as the most accurate and robust indoor localization system that was reported in literature [Mei14]. Ranging measurements are performed with a ToA UWB system with a 2 GHz bandwidth around a 7 GHz or 8 GHz center frequency. The system measures the distances of direct and reflected signal paths between the anchor node and the mobile node. With the help of ray tracing algorithms and a-priori known information of the room geometry, the location of the mobile node can be retrieved. The required availability of floor plan information should not be considered as an insuperable restriction, as most systems already use a floor plan for visualizing the localization outcome. For the simulation of reflected multipath components, calculations rely on the image method: so called 'virtual anchor points' are created as mirror images of the physical anchor node with respect to the walls [MSW10, MGM$^+$13]. The available measurement data and ray tracing algorithms enable multilateration of direct and reflected signals, leading to an estimated position of the mobile device. The result is a system that exploits multipath information, increasing localization accuracy and overcoming NLOS problems. Furthermore, the system can operate with a single

anchor node because multilateration can be performed with multiple signal components. By assigning weight factors to the signal components, a single solution of the localization algorithm can be obtained. The system performance was demonstrated in a 4.5 m x 5.5 m room, showing < 0.20 m localization errors for 95% of the tested positions [MLLW14]. In a 6 m x 8.5 m room, 95th percentile localization errors of 0.08 m to 0.20 m were reported, depending on the accuracy of the room geometry model [KLM+16]. Another configuration was evaluated in a setup for tracking indoor pedestrian movements. Therefore the system was expanded with a motion model for pedestrians, correcting localization imperfections. In this setup of a 25 m x 25 m room with a single anchor node, < 0.70 m localization errors are achieved for 95% of the tested positions [MGW10]. Operation in NLOS conditions was claimed, but no test results were reported.

A similar system is presented by Van De Velde et al. [dVS12, dVWM+12]. The proposed 'cooperative UWB positioning indoors' (CUPID) algorithm relies on the same principle of multipath ranging and ray tracing based multilateration. The difference lies in the determination of multipath weights, here relying on a cooperative algorithm that requires multiple mobile users. In a 10 m x 25 m room with LOS connections of at least three cooperating mobile nodes, a 95th percentile localization error of 0.70 m was reported.

The results of these multipath assisted UWB ranging systems demonstrate sub-meter and sometimes even centimeter accuracy for a single anchor node positioning system. These exceptional results can be attributed to the favorable UWB signal characteristics, as discussed in Section 2.3.1. However, the UWB approach is not compatible with narrowband communication systems, preventing a merge of these techniques with contemporary communication technologies.

In [dGBCK14], an outdoor localization system with three anchor nodes is presented, relying on ray traced AoA, ToA and RSS multipath data. The paper demonstrates tracking capabilities in LOS and NLOS situations, but testing conditions remain unclear and localization accuracy is not reported.

Also in the acoustic domain, multipath information has been considered for increasing (NLOS) localization accuracy [RBZF10]. In [PDV14] and [ÖDV14], a similar approach to MINT has been applied in the audio domain: ranging measurements of direct audio signals and echos lead to an estimated source position. The presented algorithms use a similar approach of virtual anchor or source points, relying on the image method. Another interesting contribution in the acoustic domain is presented in [SBO11], using a linear microphone array for resolving acoustic reflections. The position of the source is estimated using the image method.

2.6.4 Single Anchor Fingerprinting

As explained in Section 2.5, fingerprinting techniques can be used to account for the environmental effects on signal characteristics. This means that multipath effects are included in the localization process, making fingerprinting systems a type of multipath assisted localization system. Most fingerprinting systems use omnidirectional RSS data of multiple anchor nodes because of the standard availability in wireless communication systems, requiring no further hardware investments. However, some solutions with a single anchor node have been proposed, performing RSS fingerprinting for different directions of arrival. This uncommon method of DoA localization relies on measurements with multiple antennas. In [GCGM09, MCGM10] an anchor node with six directional antennas is proposed, using antenna switching to measure signal characteristics in different directions. The fingerprinting localization algorithm yields an average localization error of 2.32 m in a 7.20 m x 8.00 m room with LOS conditions. Another example can be found in [RWK16], describing a 1+12 elements parasitic array for measuring RSS values. The reported errors in an indoor 4.5 m x 4.5 m LOS area exhibit mean values ranging from 1.66 m to 1.86 m and median values of 1.12 m. More accurate results can be obtained by equipping both the anchor node and the mobile node with an antenna array, an approach that is presented in [OIS13]. In an ideal 4 m x 5 m area, average localization errors below 0.2 m were achieved.

In [SL15], a MaMIMO fingerprinting system is proposed for outdoor use. Localization of a mobile device is performed with a single base station, which is equipped with 36 to 100 antennas. Instead of performing beamforming, the algorithm uses an RSS vector containing channel hardened RSS values for each antenna of the base station (i.e. small scale fading is reduced). The base station consists of a large 50 m x 50 m antenna array, performing localization in a 150 m x 200 m area. It should be noted that the size of the array is comparable to the size of the testing area, justifying the RSS vector approach. In all system configurations, > 30 m RMS localization errors are reported.

Another paper presents an outdoor fingerprinting system that uses signal subspace matching with a single antenna array [CiTTG07]. As explained in 2.4.3, non-parametric beamforming algorithms rely on the calculation of a signal subspace. This subspace can be used as a fingerprint and matched to new measurements to perform localization. No numerical results on positioning accuracy were reported, however LOS localization was described as ‘successful’, while NLOS and multipath localization was found to be erroneous. Kupershtein et al. tested a similar approach with a single 6-element circular array in indoor multipath environments [KWC13]. The system was trained and evaluated in a 33 m x 33 m indoor NLOS area consisting of multiple rooms. In this exact

setup, 95% of the measurements resulted in < 5 m localization errors.

2.6.5 Combination of Localization Techniques

Seow et al. proposed a multipath aided positioning system that combines AoA and ToA measurements, enabling an accurate distinction between LOS and NLOS signal components [CSW12, ST08]. The system exploits LOS signals and first order reflections using the virtual anchor node approach. Tests were performed with non-specified hardware. Three anchor nodes were placed in a 20 m x 26 m outdoor area and five positions of the mobile node were evaluated, varying the number of LOS connections. The tests demonstrated overall localization feasibility in LOS and NLOS situations, but no overall results on achievable accuracies in the whole testing area are presented.

[TGdAG09] claims improved results for a fingerprinting system that combines ray traced AoA and RSS data. Details on the applied localization method, test setup and results are not completely disclosed in the paper. A test setup with 9 anchor nodes in a 25 m x 25 m building renders mean localization errors between 0.45 m and 0.9 m, depending on the configuration.

In [HPT+16], Hanssens et al. presented an UWB localization system with a 4-element array as anchor node and an identical array as mobile node. The system with 8 GHz bandwidth combines AoA, AoD and ToA measurements. Furthermore, floor plan information is used for ray tracing, enabling localization in NLOS situations. In the considered 16 m x 11 m non-rectangular test area, median localization errors of 0.42 m in LOS conditions and 1.22 m in NLOS conditions were reported.

2.6.6 Summary

The performance of a localization system is always expressed in terms of localization errors, here denoted as ϵ_{loc}. Some papers report the mean value, the 50th percentile (median), 95th percentile or RMS value of the errors. The comparison of systems is therefore difficult. The assessment of various localization systems is further complicated by tests in differently sized environments. In an attempt to overcome this issue, localization errors are normalized to the size of the testing area, although this still does not account for differences in building materials or room interiors. The normalization is expressed in Equation 2.32, where a and b denote the dimensions of the (rectangular) testing area. Since the room diagonal represents the largest

possible localization error, all normalized error values $\hat{\epsilon}_{\text{loc}}$ will range between 0 and 1.

$$\hat{\epsilon}_{\text{loc}} = \frac{\epsilon_{\text{loc}}}{\sqrt{a^2 + b^2}} \tag{2.32}$$

Table 2.1: Summary of localization accuracies

Description	param.	$\hat{\epsilon}_{\text{loc}}$
Triangulate, 3 arrays, LOS, open area [ACD+11]	mean	0.061
RSS fingerprinting with multipath reduction [hFnLcL08]		
1 anchor node	mean	0.256
8 anchor nodes	mean	0.020
Multipath assisted UWB ToA, LOS [MLLW14]	P95	< 0.028
Multipath assisted UWB ToA, LOS [KLM+16]	P95	0.008 . . . 0.019
Multipath assisted UWB ToA pedestrian, LOS [MGW10]	P95	0.020
Multipath assisted UWB ToA (CUPID), LOS [dVS12, dVWM+12]	P95	0.026
Single anchor, 6 antennas, fingerprinting, LOS [GCGM09, MCGM10]	mean	0.216
Single anchor, 1+12 antennas, fingerprinting, LOS [RWK16]	mean	0.261 . . . 0.292
Rx-array and Tx-array, fingerprinting, LOS [OIS13]	mean	0.031
MaMIMO outdoor RSS fingerprinting, LOS [SL15]	RMS	> 0.120
Single anchor, 6 antennas, NLOS fingerprinting [KWC13]	P95	< 0.107
AoA and RSS fingerprinting, 9 anchor nodes [TGdAG09]	mean	0.013 . . . 0.026
UWB AoA, AoD, ToA multipath assisted, LOS [HPT+16]	P50	0.022
UWB AoA, AoD, ToA multipath assisted, NLOS [HPT+16]	P50	0.063

Table 2.1 lists the reported mean, median, P95 and RMS normalized localization errors. The performance of multipath assisted systems is remarkable, with 95% of the errors lower than 3% of the room diagonal. The LOS conditions and UWB ToA approach play an important role in these results. RSS fingerprinting systems exhibit significantly lower performance, especially if a single anchor node is used. NLOS results are very limited, with just [HPT+16] reporting a threefold increase of median error values. This overview illustrates that non-UWB systems are characterized by a significantly lower performance compared to UWB systems. Furthermore, multipath measurements can provide useful information for an improvement of robustness and accuracy. As a result, multipath assistance in non-UWB systems can be considered as a promising solution that is worth investigating.

2.7 Conclusions Concerning Indoor Localization

In this chapter, the difference between proximity, range, angle and fingerprinting based systems was elaborated. In the range based category, RSS and ToF signal characteristics are used. The RSS method relies on the Friis path loss equation to calculate distances, while ToF methods rely on the finite propagation speed of electromagnetic waves. This property is exploited in ToA, TDoA and TWR systems, measuring signal timing with or without time synchronized nodes.

AoA localization schemes mostly use phased antenna arrays to measure signal directions. A theoretical analysis provided insights in hardware and processing characteristics. Based on the presented signal models, AoA estimation algorithms are discussed. The beamscan and MVDR algorithm are considered non-parametric methods that result in a spatial spectrum. MUSIC and ESPRIT represent parametric subspace-based algorithms that rely on the eigenstructure properties of the spatial covariance matrix to calculate the AoA values. Overall, these AoA estimators underperform in multipath environments due to signal correlation. With the help of preprocessing techniques like forward-backward averaging or spatial smoothing, this effect can be counteracted.

Fingerprinting based localization systems rely on surveyed signal characteristics (usually RSS data) to find the position of a mobile node. With pattern matching algorithms like kNN, a measurement vector is linked to a location in a set of training data.

Previous work in the field of indoor localization with AoA methods demonstrated good performance in LOS conditions. However, performance degrades in multipath and NLOS situations, so various solutions have been proposed. The most applied technique consists of multipath and NLOS mitigation, showing significant accuracy improvements. Another approach involves multipath assisted localization, producing impressive results by exploiting multipath effects. In combination with UWB ranging techniques, cm-accuracy was demonstrated. In the field of fingerprinting, some interesting contributions were presented, measuring the multipath channel with a single anchor node. Finally, the combination of localization techniques was investigated, presenting solutions that combine AoA, ToA, RSS and AoD data in order to obtain a higher accuracy and robustness in LOS and NLOS conditions.

Chapter 3 presents a new localization approach based on AoA measurements. The proposed technique relies on ray tracing and allows single anchor node localization, resembling the multipath assisted method that has previously been explored in UWB ToA systems.

Chapter 3

Indoor Multipath Assisted Angle of Arrival Localization Method

The theoretical background and related research of Chapter 2 provides a solid basis for the development of a localization system. This chapter introduces a method for indoor multipath-assisted localization based on AoA measurements. Section 3.1 provides a general overview of the system, starting with the assumptions, boundary conditions and requirements, followed by a high-level description of the localization process. The proposed technique relies on multipath propagation and requires the design of a ray tracer, which is covered in Section 3.2. The system is implemented using a fingerprinting approach, so Section 3.3 discusses the training data, while Section 3.4 treats the measurement data. The matching algorithms are presented in Section 3.5. The localization process is initially aimed at single anchor systems, so Section 3.6 explains how data can be merged in multi-anchor setups. The criteria for evaluating localization accuracy are presented in Section 3.7. The conclusions of this chapter are summarized in Section 3.8.

3.1 System Overview

The research questions of chapter 1 form a guideline for this work. The first question is answered by Section 2.6, demonstrating that multipath components

contain spatial information that can be exploited by localization systems. A straight-forward and widely applied approach consists of fingerprinting. However, this technique requires a labor intensive setup phase and it is sensible to changes in the environment. In UWB multipath assisted indoor positioning systems, LOS signals and specular reflections can be resolved. With the help of a floor plan, these signals are traced back to the position of the mobile transmitter, even enabling localization in NLOS conditions. The limited research of multipath assisted indoor localization has only been reported recently and focuses on ToA measurements. However, no results for AoA are reported, leaving room for further exploration of this concept.

In order to answer the remaining research questions, a new localization method is envisioned, leveraging on the ideas that have been explored in literature. Before explaining the core architecture, the assumptions and boundary conditions are discussed.

3.1.1 Assumptions, Boundary Conditions and Requirements

The system is centered around AoA measurements to observe the multipath environment. The AoA approach with antenna arrays is selected for its conformity with contemporary (Massive) MIMO systems, enabling a future implementation in communication systems (e.g., 802.11ac [Hoe13] and cellular systems [Mol11], etc.). From this point of view, the 2.4 GHz and 5 GHz ISM bands are selected as operation frequencies of the system.

A network based approach is proposed, offloading all processing to the server side. This relaxes the computational requirements for mobile devices, making the technology accessible for sensor networks. Of course, this design choice imposes further challenges that are not covered by this research, for example user privacy.

Considering the practical implementation of the system, only single room setups with a single mobile node are currently evaluated. This ensures maximum control of environmental parameters, resulting in straight-forward and consistent LOS and NLOS testing. Furthermore, results will be comparable to the related work in Section 2.6, which mostly applies a similar approach.

With respect to anchor nodes, multiple assumptions and requirements are put forward. For AoA measurements, uniform linear arrays are proposed. The symmetrical structure and a uniform $\lambda/2$ inter-element spacing allows forward-backward averaging, spatial smoothing and ESPRIT, while maintaining a field of view of 180°. As explained in Section 2.4, the linear array only measures broadside angles. This allows a 2D simplification of the localization problem,

assuming elevation angles of 0°. A 2D floor plan is sufficient in this respect, and mobile nodes and anchors are always placed in the same horizontal plane (i.e. at the same height).

For the placement of anchor nodes, only lateral positions are considered, close to the walls of the room. From a user point of view, this means that no inconvenient infrastructure is required in the middle of the room. From a technical point of view, this design choice solves the problem with ULAs not being able to distinguish the frontside from the backside of the array, which was discussed in Section 2.4.1. By placing the array against a wall, signals from the backside can be eliminated, so all estimated AoA values can be considered frontal.

Furthermore, the system should be able to operate with a single anchor node. As demonstrated in [GCGM09, RWK16], a single antenna array can be used for positioning by measuring multipath propagation. However, the addition of extra nodes should be straight-forward, resulting in a flexible system.

An important requirement is a straight-forward and easy setup phase, with flexibility to add extra nodes or even other signal parameters (e.g., ToF, RSS). This does not only speed up the installation of a system, but also the development and evaluation. Furthermore, the system should be tolerant to changes in the environment. Multipath information should be exploited to enhance localization accuracy and improve NLOS results. It is clear that a classical fingerprinting approach does not meet these requirements. Therefore, a multipath assisted algorithm is proposed, estimating a position based on AoA measurements.

3.1.2 Localization Process

The outline of the envisioned localization algorithm for a single anchor node is visualized in Figure 3.1. The overall structure resembles a fingerprinting approach with an online and offline phase. However, no labor intensive site surveying is required in the training phase, but multipath simulations are performed instead. These simulations are performed in the offline phase in order to alleviate the computational load during localization (i.e. the online phase). For the multipath calculations, only the fixed infrastructure is taken into account, ignoring movable objects like furniture. As a result, only the guaranteed multipath components are included, reducing the impact of changes in the environment. This approach requires only a basic floor plan without details, facilitating the setup of the system. However, the validity of these simplifications should be verified. For the multipath simulations, a fine grid of training positions $\boldsymbol{p}_i = (x_i, y_i)$ is defined in the room. For each grid point, the propagation path is simulated and stored as a fingerprint $\boldsymbol{f}_i$. The resulting

training vector $\mathcal{T}$ contains multipath AoA information for every position in the room.

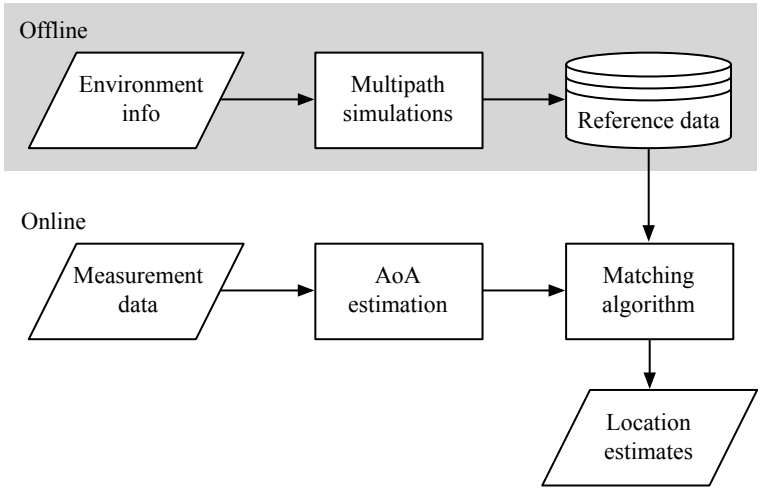

Figure 3.1: Architecture of the localization process with a single anchor node

The online phase always starts with measurement data from the antenna array (i.e. phase and amplitude information of each channel). This data is processed by AoA estimation algorithms, forming a representation of the multipath environment as vector $\boldsymbol{m}$. A pattern matching algorithm is used to calculate the resemblance between the measurement vector $\boldsymbol{m}$ and the simulated training data. The result can be represented as a 'Spatial Probability Density Function' (SPDF), visualizing the probability of the transmitter location for each position $\boldsymbol{p}_i$ in the room. The position with the highest probability yields the estimated location.

When multiple anchor nodes are used, the localization process is repeated for each anchor node, resulting in multiple SPDFs. These results can be combined, as discussed in Section 3.6. The same approach can be applied for combining localization results of various signal characteristics.

3.2 Multipath Propagation

Multipath propagation can be defined as the phenomenon of a signal travelling from a transmitter to a receiver via different propagation paths. These paths are created by irregularities in the medium, resulting in propagation effects

like reflection, refraction, diffraction and scattering [SAZ07, SWSPB03, Sey05]. These effects depend on the frequency and polarization of the signals, the angle of incidence, and the properties of the medium and the obstacles.

When an electromagnetic wave impinges on a large object ($\gg \lambda$) with a smooth material boundary, a part of the energy is reflected in a specific direction. The non-reflected part of the signal is transmitted through the object with an altered direction, i.e. the refracted signal component. For indoor wireless communication systems in the sub-5 GHz domain, these specular reflections and refractions usually occur at the large surfaces of walls, floors and furniture.

Diffraction occurs at obstacles with sharp material boundaries ($< \lambda$). Given the small nature of these irregularities, waves are not blocked or reflected, but bend around the edge, changing direction.

Scattering is sometimes denoted as non-specular reflections, spreading the impinging energy in different directions instead of one specular component. This effect happens when an electromagnetic wave impinges on many small obstacles compared to the wavelength. In practice, this occurs at rough material boundaries, small furniture, stairs, etc.

3.2.1 Multipath Simulators

In the offline phase of the localization system, channel simulations are performed to generate a training set of AoA data. A variety of software packages for simulating radio propagation is commercially available (Softwright TAP®, Ranplan iBuildNet®, iBwave®, Altair ProMan®, Fluke InterpretAir®, EDX SignalPro®, Actix Analyzer®, etc.). However, the focus is mostly on generating coverage maps for wireless communication systems [dGBCK14]. In the proposed localization approach, signal parameters are desired for all individual signal paths. Furthermore, integration in a Matlab® framework is required for a flexible design flow. The evaluation of features, stability, overhead and cost of commercial channel modelling tools, resulted in a design choice for a dedicated multipath simulator, as explained in Section 3.2.3. This solution allows a simplified, low complexity implementation that only provides the required signal parameters and can be integrated in the developed Matlab® framework. This approach was also followed by the other multipath assisted systems in Section 2.6.

3.2.2 Multipath Simulation Techniques

In order to predict signal propagation, two different approaches can be followed [TT95]. Statistical or empirical methods follow standard propagation models that can be applied in a wide variety of environments. These generalized methods rely on approximations and do not include any environmental information, resulting in relatively low complexity and limited accuracy. Site-specific or deterministic methods rely on a geometric model of the environment to calculate all signal components, which is a computationally intensive task with accurate results. Theoretically, signal propagation in a given environment could be computed exactly with the Maxwell equations. This solution is not practically conceivable, as it would require a very detailed model of the infrastructure and complex computations [SKS12]. Therefore ray tracing techniques are usually applied, offering high accuracy with an acceptable level of complexity.

Ray tracing is a multipath simulation technique based on Geometric Optics (GO) [JSR11]. The energy of the electromagnetic waves is assumed to travel through infinitesimally small tubes called 'rays'. These rays indicate the travel direction of the waves in a straight line, normal to the plane of equal signal power. For the simulation of a propagation channel, two implementations of ray tracing can be followed. The 'brute-force', 'ray launching' or 'shooting and bouncing' method can be considered as a Monte Carlo simulation, transmitting a large number of rays in random directions. For each ray, the propagation path is calculated. If a path arrives at the receiver, its contribution to the received signal is calculated, otherwise the signal path is discarded. This method is appropriate for complex environments, but requires a lot of computational power due to the number of rays to be calculated. Also, the accuracy heavily relies on the number of simulated rays [SM99].

Another ray tracing technique is the 'image method' [LG11, IY02]. By mirroring the complete geometry of the environment against each possibly reflecting surface, images are created with virtual transmitters or receivers. Instead of launching rays in random directions, only the point-to-point connections between the transmitter and (virtual) receivers are simulated. This method is particularly appropriate for simulating LOS and specularly reflected signal components. Especially in low complexity infrastructures, this results in a high computational efficiency and high accuracy.

3.2.3 Simulation Environment

A basic simulation environment was developed in order to simulate the various paths that can be followed from transmitter to receiver. The starting point is

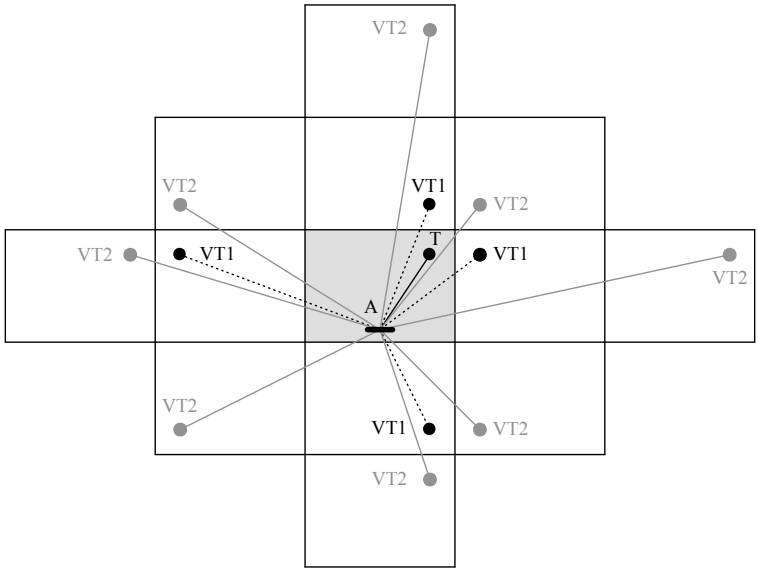

Figure 3.2: Virtual image method: a rectangular room with anchor node (A), transmitter (T), first order virtual transmitters (VT1) and second order virtual transmitters (VT2)

a two-dimensional map of a rectangular room with one antenna array and a mobile transmitter. This basic approach was considered sufficient given the early research stage, limiting tests to rectangular rooms. Because of these properties, the image method was selected for generating site-specific reference data for the localization system. This technique creates a virtual environment of mirrored rooms, as depicted in Figure 3.2.

The implementation only simulates the LOS connection and specular reflections up to a given order. Diffracted and scattered components are not considered for two reasons. First of all, these signal components do not contain valuable spatial information on the location of the transmitter, as scattering and diffraction cause unknown changes in the directions of the rays [MLLW14]. Furthermore, previous research has indicated that these components generally carry a significantly lower energy than the line-of-sight (LOS) connection or specular reflections in indoor environments for the considered frequency domain [YI05, GMM+14, SIM11, SWSPB03].

At the large material boundaries, the power of the incident wave P_i is split into a reflected component P_r and a transmitted component P_t, as depicted in Figure 3.3. Specular reflections only occur at sufficiently smooth material

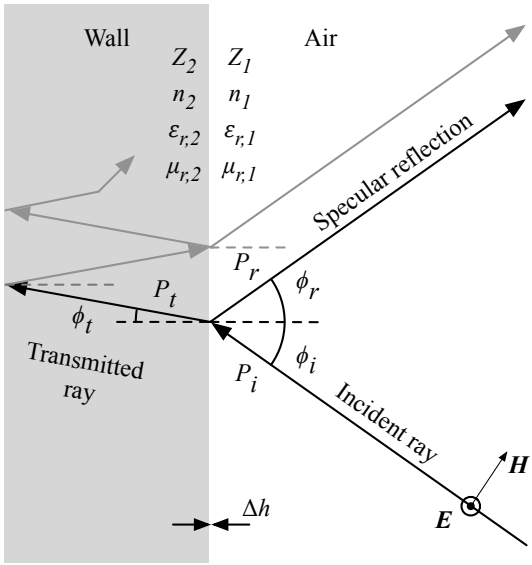

Figure 3.3: Multipath effect at a smooth and large material boundary

boundaries. This condition is met when the boundary imperfections (Δh in m) meet the Rayleigh criterion of Equation 3.1 [SAZ07]. The grazing angle (i.e. the angle of the impinging rays) is denoted as ϕ_i. For 5 GHz signals, this means that $\Delta h < 0.0075$ m, a criterion that can be assumed valid for most indoor walls.

$$\Delta h < \frac{\lambda}{8\cos(\phi_i)} \tag{3.1}$$

Specular reflections are calculated according to the Fresnel formulas, with incident and reflected angles being equal to each other ($\phi_i = \phi_r$) [Sey05, PP00, SAZ07]. This property is the foundation of multipath assisted systems: because of this predictability, signal paths can be traced, enabling the calculation of a transmitter position, be it in the time domain or angular domain. The interaction of the waves at the material boundaries can be treated as a transmission line problem. In order to calculate the reflection of the incident wave, the reflection coefficient Γ is defined in Equation (3.2). Z_{wall} represents the effective wave impedance of the wall material and Z_{air} is the wave impedance of air. These quantities are a function of wave polarization, grazing angle ϕ_i, the relative permittivity and permeability of air ($\varepsilon_{r,1}$ and $\mu_{r,1}$), and the relative permittivity and permeability of the wall ($\varepsilon_{r,2}$ and $\mu_{r,2}$). The material properties determine

the field impedance Z_{field} and refractive index n of the medium. However, when working with non-magnetic materials $\mu_r = 1$, leading to the simplified expressions 3.3.

$$\Gamma = \frac{Z_{\text{wall}} - Z_{\text{air}}}{Z_{\text{wall}} + Z_{\text{air}}} \tag{3.2}$$

$$\begin{aligned} Z_{\text{field}} &= 120\pi\sqrt{\frac{\mu_r}{\varepsilon_r}} \approx 120\pi\frac{1}{\sqrt{\varepsilon_r}} \\ n &= \sqrt{\mu_r\varepsilon_r} \approx \sqrt{\varepsilon_r} \end{aligned} \tag{3.3}$$

In the simulated environment, a vertically polarized antenna is assumed for the transmitter (e.g., a half wavelength vertically oriented dipole). This means that the considered reflections against the walls are transverse electric: the electric field vector ($\boldsymbol{E}$) is normal to the plane of incidence (i.e. the plane that contains the incident and reflected rays). In this case, the reflection coefficient $\Gamma_\perp$ can be calculated as in Equation 3.4, which is a function of ϕ_i, ϕ_t and the field impedances of medium 1 and 2 (Z_1 and Z_2).

$$\Gamma_\perp = \frac{Z_2\cos(\phi_i) - Z_1\cos(\phi_t)}{Z_2\cos(\phi_i) + Z_1\cos(\phi_t)} \tag{3.4}$$

The refracted angle ϕ_t is generally unknown, but can be calculated with Snell's law of refraction in Equation 3.5. As a result, $\Gamma_\perp$ can be formulated as a function of material parameters $\varepsilon_{r,1}$, $\varepsilon_{r,2}$ and the grazing angle ϕ_i, in Equation 3.6.

$$\frac{\sin(\phi_i)}{\sin(\phi_t)} = \frac{n_2}{n_1} \tag{3.5}$$

$$\Gamma_\perp = \frac{Z_2\cos(\phi_i) - Z_1\sqrt{1 - \left(\frac{Z_2}{Z_1}\right)^2\sin(\phi_i)^2}}{Z_2\cos(\phi_i) + Z_1\sqrt{1 - \left(\frac{Z_2}{Z_1}\right)^2\sin(\phi_i)^2}} \tag{3.6}$$

The resulting reflection coefficient $\Gamma_\perp$ represents a ratio of electric field strengths. Equation 3.7 expresses the reflection power loss L_r in dB.

$$L_r(\text{dB}) = P_i(\text{dBm}) - P_r(\text{dBm}) = -20\log_{10}|\Gamma_\perp| \tag{3.7}$$

Besides the specular reflection, signal transmission and refraction occurs at material boundaries, as illustrated in Figure 3.3. In case of homogenous walls, the transmitted ray can result in a (weak) contribution to the specular reflection. In this case, multiple reflection and transmission coefficients should be included, as well as absorption. Signal absorption for concrete, brick and plasterboard walls has been reported as respectively 165 dB/m, 42 dB/m and 37 dB/m at 2.4 GHz [SLD08, SJRMB02]. However, walls can mostly not be considered as homogenous structures because of cavities, metal structures for reinforcement or support, or other imperfections. These inner structures are generally unknown and make transmitted rays highly unpredictable and thus invaluable (cfr. scattered and diffracted rays). Because of the reduced signal strength and unpredictability of transmitted rays, these components are not considered for ray tracing. This approach is called a 'thin wall' approximation, which was validated in [YI05].

For each simulated ray, the loss L_{ray} is calculated as a sum of the free space path loss ($L_{\text{path,free}}$) and all reflection losses against north-south oriented walls ($L_{r,NS}$) and east-west oriented walls ($L_{r,EW}$) [SIM11]. $L_{\text{path,free}}$ is calculated according to the Friis path loss Equation 2.2 with path loss exponent $n_{\text{path}} = 2$ and d representing the unfolded path length of the ray. The $L_{r,NS}$ and $L_{r,EW}$ values are calculated according to Equations 3.6 and 3.7. The assumed values for ε_r are presented in Section 3.2.4.

$$L_{\text{ray}}(\text{dB}) = L_{\text{path,free}} + \sum L_{r,NS} + \sum L_{r,EW} \tag{3.8}$$

The result is a 2D ray tracer based on the image method, simulating LOS signals and specular reflections as proposed in literature. The dimensions of the room, wall material permittivity, operation frequency, the positions of transmitter and array, and the simulated reflection orders are adjustable, enabling simulations of different setups. The outputs of the algorithm contain signal loss, AoA, travelled distance and reflection order for each simulated ray. The algorithm was implemented in a Matlab® framework with visual feedback, focusing on minimizing CPU load and memory pressure. An example of a simulated 5 m by 5 m room with brick walls is presented in Figure 3.4. The simulation of this room with fourth order reflections on a 2.3 GHz Intel® Core i5 2415M mobile CPU with 8 GB of RAM, takes 0.17 seconds.

3.2.4 Wall Permittivity

The execution of the ray tracing algorithm requires knowledge of the relative permittivity (i.e. the dielectric constant) of the walls. Therefore, a literature

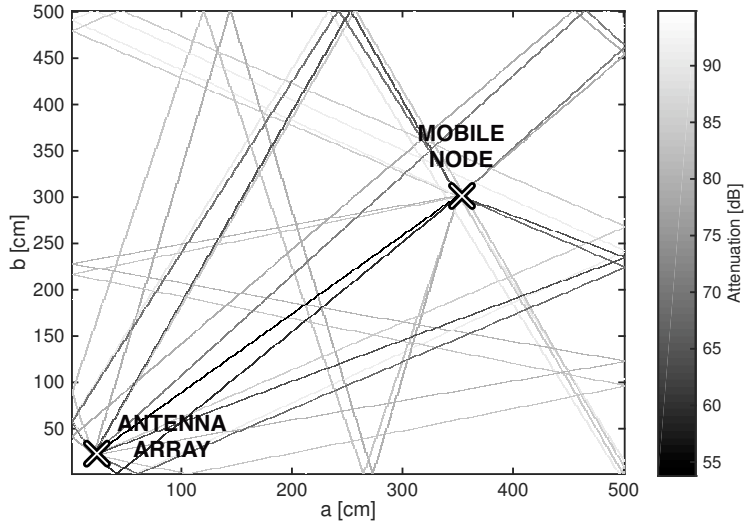

Figure 3.4: Simulated rays in a room of 5 m by 5 m with brick walls

study was performed focusing on material properties in the 2.4 GHz and 5 GHz ISM bands. The considered building materials include concrete, bricks and plasterboard. The electromagnetic properties of these popular building materials have been examined extensively. However, when examining the permittivity of the considered materials, a considerable variation can be observed across different studies. For concrete walls at 2.4 GHz, relative permittivity were found from 2.3 up to 12 [SLD08, SRFb$^+$11, Lim12, YBWT12, OMHS13, THAD11, SJRMB02]. These values depend on the age, composition, humidity, etc. An analysis of these results pointed out that 8.0 is a valid compromise. The values for bricks showed to be more consistent, with the relative permittivity ranging from 3.82 to 4.75 [CnPHGS01, CS02, Lim12, THAD11, SJRMB02]. The dielectric constant of plasterboard (i.e. drywall) was found to be between 2 and 2.8 [CnPHGS01, CS02, Lim12, THAD11, SJRMB02], so a value of 2.4 was selected for simulations. Wood was not considered in the simulations, but according to previous research, the electromagnetic properties are comparable to plasterboard properties. The same literature study was repeated for the 5 GHz band. However, the differences between ε_r values in the 2.4 GHz and 5 GHz band are inconsistent and usually smaller than the differences that can be observed among papers. Therefore, the same values are used in both frequency bands: $\varepsilon_{r,\text{concrete}} = 8.0$, $\varepsilon_{r,\text{brick}} = 4$ and $\varepsilon_{r,\text{plasterboard}} = 2.4$.

3.2.5 Multipath Simulations

The proposed method for simulating specular reflections of smooth surfaces has been evaluated extensively in literature. Measurement campaigns indicated that the combination of Fresnel equations and a free space path loss model form an adequate approximation of real-world reflections for common building materials in the frequency range of interest [LFR96]. Most simulators are used for calculating RSS values or power delay profiles, which indicate the received power as a function of time. However, the setup and evaluation of the envisioned localization system requires detailed insights in specular reflection characteristics. On this matter, no suitable research results were found, so ray tracing simulations were performed in various environments at 2.4 GHz and 5 GHz. For each test, four reflection orders are simulated, the antenna array is positioned in a corner of the room, as depicted in Figure 3.4, while the mobile transmitter is positioned in 2500 uniformly distributed grid positions, independent of the room size. These simulations allow an evaluation of signal reflections as a function of room size, building materials, and operation frequency.

Room size

In a first series of simulations, the influence of the room size on the received rays is investigated. Figure 3.5 depicts the 2.4 GHz signal attenuation of the LOS signal till the fourth order reflection, for a room with brick walls of 3 m by 3 m (a), 5 m by 5 m (b) and 10 m by 10 m (c). The graph considers all simulated rays over all 2500 simulated transmitter positions. For each reflection order, a normalized histogram with a 0.5 dB resolution is plotted, representing a probability density function (PDF). A first noticeable phenomenon is the stronger attenuation of signals as the room size increases, which can be explained by the generally longer paths from transmitter to receiver, leading to a greater free space loss. The increase of attenuation affects all reflections equally, since the size of the room does not influence reflection coefficients.

Wall Material

Figure 3.6 presents the influence of the wall material on the received rays. A room of 5 m by 5 m was simulated with concrete walls (a), brick walls (b) and plasterboard walls (c). Logically, LOS signal strength is not influenced by wall materials, so these signal levels are equal among the three simulations. On the other hand, it is clear that the signal strength of reflections is influenced by the used wall materials. Concrete is the best reflector, causing the PDF of different reflection orders to overlap to a considerable extent, making it difficult

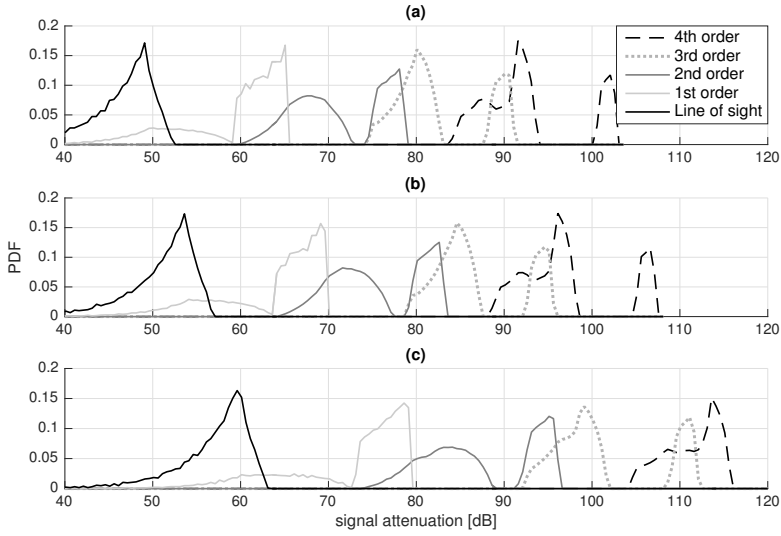

Figure 3.5: 2.4 GHz signal attenuation of incident rays for a 3 m by 3 m (a), 5 m by 5 m (b) and 10 m by 10 m (c) room with brick walls

to predict which reflections will be received. Brick walls are less reflecting, resulting in a less dense multipath. Plasterboard walls are the least reflecting, so reflected signals are strongly attenuated. Second order reflections in a 5 m by 5 m room can already exceed 90 dB attenuation.

Operation Frequency

Figure 3.7 depicts the influence of the operation frequency in a 5 m by 5 m room with brick walls. The PDF of the LOS and reflected signals are presented at 2.4 GHz (a) and 5 GHz (b). Since the relative permittivity of the walls was set at $\varepsilon_{r,\text{brick}} = 4$ for both frequencies, the reflection coefficient is frequency independent. Consequently, only the path loss changes with frequency, resulting in an overall shift of all PDF with -7 dB from 2.4 GHz to 5 GHz. This means that increasing the operation frequency has the same influence on ray signal strengths as increasing the room dimensions.

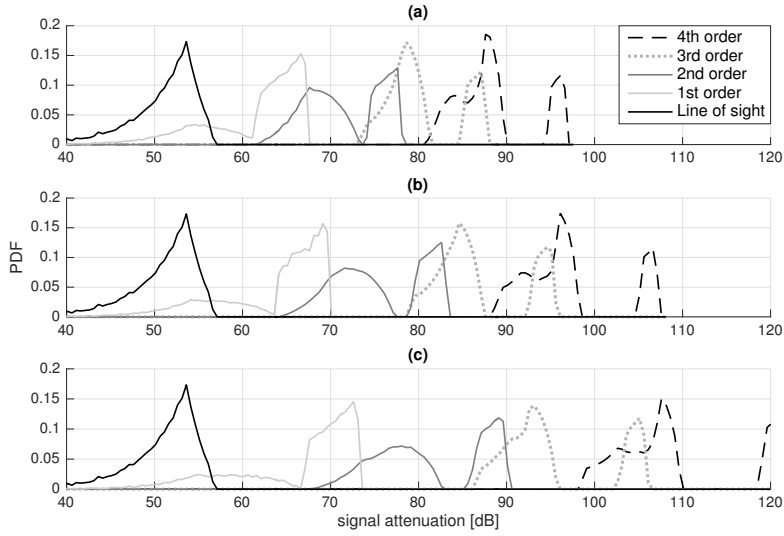

Figure 3.6: 2.4 GHz signal attenuation of impinging signals for a 5 m by 5 m room with concrete (a), brick (b) or plasterboard walls (c)

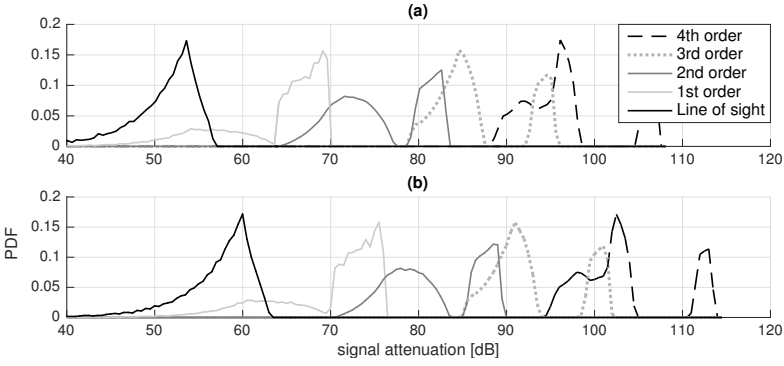

Figure 3.7: Signal attenuation of impinging signals for a 5 m by 5 m room with brick walls at 2.4 GHz (a) or 5 GHz (b)

Conclusions

First of all, simulating reflections up to the fourth order seems sufficient: in a rectangular room, this results in 40 reflected rays with attenuations up to > 100 dB. In large rooms with plasterboard walls, receiving high order reflections is unlikely. Here, the interference of strongly reflecting or scattering (metallic) objects could be problematic. This holds especially in the 5 GHz band, with overall weaker signals and specular reflections of smaller objects, following the Rayleigh criterion. In smaller concrete rooms localization might also be difficult, as many high reflection orders will be received, complicating the detection of first order reflections. These simulation results can be translated to hardware requirements. In large rooms and at 5 GHz, extra signal amplification can be crucial for a sufficient signal detection, although this does not solve the interference problem. In dense multipath environments (small rooms and/or concrete walls), larger arrays could help in distinguishing the large number of reflections.

3.3 Reference Data

As explained in Section 3.1.2, fingerprint vectors $\boldsymbol{f}_i$ are gathered in multipath simulations. These vectors are matched to a measurement vector $\boldsymbol{m}$ to find the location of a node. $\boldsymbol{m}$ represents the measured AoA data, which can consist of a (continuous) spatial spectrum or discrete angular values. A similar format is desired for the fingerprint vectors. Therefore, each fingerprint vector $\boldsymbol{f}_i$ consists of a (discrete or continuous) spatial spectrum $P_{\text{sim}}(\theta)$, which is generated by the multipath simulator. The result is a training data set $\mathcal{T}$, consisting of simulated spatial spectra.

The fingerprint vectors are only used for their AoA data and not for the overall signal power. Therefore, the simulated spatial spectra $P_{\text{sim}}(\theta)$ [dB] are normalized to angular probability density functions $P_{\text{PDF,sim}}(\theta)$, as described by Equation 3.9 and illustrated in the following sections. As a result, all fingerprints $\boldsymbol{f}_i$ have the same overall weight $\left(\int \boldsymbol{f}_i d\theta = 1\right)$, possibly simplifying matching algorithms.

$$P_{\text{PDF,sim}}(\theta) = \frac{P_{\text{sim}}(\theta) - \min[P_{\text{sim}}(\theta)]}{\int_{-90^\circ}^{90^\circ} P_{\text{sim}}(\theta) - \min[P_{\text{sim}}(\theta)] d\theta} \tag{3.9}$$

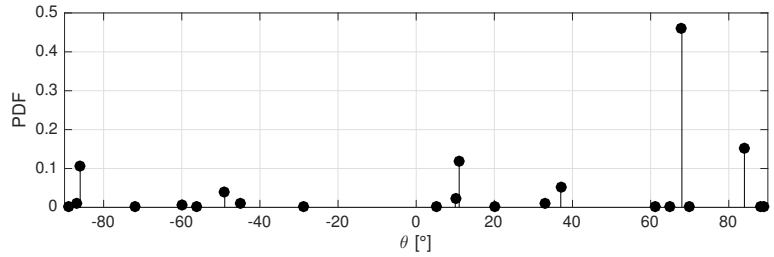

Figure 3.8: Fingerprint example of a normalized spatial spectrum of discrete ray traced values: $\boldsymbol{f}_{\text{raytrace,discrete},i}$

3.3.1 Discrete Ray Tracing Data

The most direct approach for composing a training vector, is the use of discrete outputs of the ray tracing algorithm. For each simulated ray, the signal attenuation L_{ray} and the AoA θ_{ray} is available. Plotting the signal attenuations for all simulated rays with $\theta \in [-90°, 90°]$ results in a simulated spatial spectrum with discrete peaks. The normalization of this discrete spectrum according to Equation 3.9 results in the fingerprints $\boldsymbol{f}_{\text{raytrace,discrete},i}$. Figure 3.8 depicts an example fingerprint, demonstrating a normalized discrete spectrum.

3.3.2 Artificial Spatial Spectrum Based on Ray Tracing

The spectrum with discrete ray tracing data forms a close representation of the multipath simulations. However, the measured data will often be represented as a continuous spatial spectrum, which can be considered as a spatially filtered power output of the array, as explained in Section 2.4.2. This difference between fingerprint and measurement vectors could form an additional challenge for the matching algorithm. Therefore, a method is presented to artificially create a spatial spectrum from discrete ray tracing data, without applying AoA algorithms.

The goal is to achieve a result that resembles an MVDR spatial spectrum. MVDR was selected because it generally outperforms beamscan, as explained in Section 2.4.2. In order to create the artificial spatial spectrum, the discrete ray tracing spectrum is circularly convolved with a filter window $h(\theta)$, as expressed in Equation 3.11. For the calculation of the circularly convolved spectrum $P_{\text{PDF,circonv}}(\theta)$, a periodic discrete spectrum is defined: $P_{\text{PDF,raytrace,discrete},T}(\theta)$.

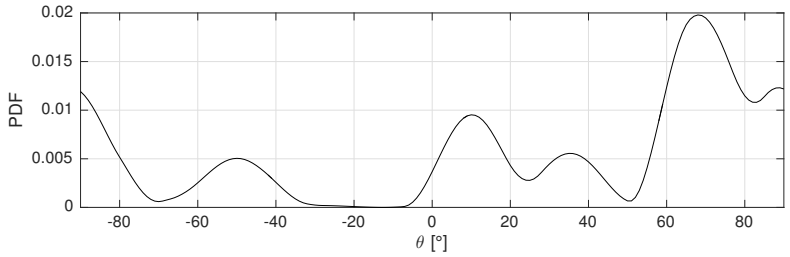

Figure 3.9: Fingerprint example of an artificial spatial spectrum, created by the circular convolution of discrete ray traced values with a Hanning window: $\boldsymbol{f}_{\text{raytrace,circonv},i}$

$$P_{\text{PDF,discrete},T}(\theta - 90^\circ + k \cdot 180^\circ) = P_{\text{PDF,discrete}}(\theta - 90^\circ) \tag{3.10}$$

$$P_{\text{PDF,circonv}}(\theta) = \left[\left(P_{\text{PDF,discrete},T} * h\right)(\theta)\right]_{\theta \in [-90^\circ, 90^\circ]} \tag{3.11}$$

Because the MVDR spatial filter weights w_{MVDR} depend on the received data, the filter shape and bandwidth are variable and difficult to determine [SM05]. Therefore, the shape of the filter window $h(\theta)$ of the artificial spectrum was empirically chosen. A Hanning window was selected for its limited side lobes and zeros at the end points of the window, preventing discontinuities after the convolution. The width of the window was empirically fixed as $W = 180^\circ/(M - K_{ss} - 1)$, following Equation 2.28. Figure 3.9 depicts an artificial spatial spectrum $\boldsymbol{f}_{\text{raytrace,circonv},i}$, which was created with the proposed method.

$$h(\theta) = \frac{1}{2}\left(1 - \cos\left(\frac{360^\circ \theta}{W}\right)\right)_{\theta \in [0, W]} \tag{3.12}$$

3.3.3 Simulated MVDR Spectrum

Another way to generate reference data is by processing the discrete ray tracer outputs with a simulation model of an antenna array, followed by an AoA estimation. The goal of this approach is to obtain fingerprints that resemble the measured spatial spectra more closely. Therefore, the MVDR algorithm was selected, generating the $P_{\text{PDF,MVDR}}(\theta)$ spatial spectra. The beamscan algorithm was omitted in this context because of its reportedly inferior performance.

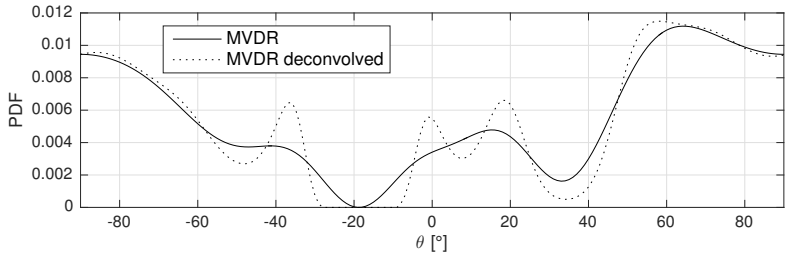

Figure 3.10: Fingerprint example of a simulated MVDR spatial spectrum and its deconvolution: $\boldsymbol{f}_{\mathrm{MVDR},i}$ and $\boldsymbol{f}_{\mathrm{MVDR,deconv},i}$

ESPRIT and MUSIC were not considered either, as they only generate discrete AoA values instead of a spatial spectrum. Discrete AoA values are already generated by the ray tracer, making the subspace based methods redundant for fingerprint generation.

In order to generate $P_{\mathrm{PDF,MVDR}}(\theta)$, the ray tracer outputs are processed by a simulation model of an antenna array, followed by an MVDR AoA estimator. The developed simulation environment takes advantage of the Matlab® phased array toolbox to create a model of the antenna array and simulate the output signals, followed by an MVDR AoA estimation. Forward-backward averaging is applied in all situations, since it does not have any negative consequences. The amount of spatial smoothing (K_{ss}) is always considered equal to the amount of smoothing in $\boldsymbol{m}$. Figure 3.10 depicts an MVDR spatial spectrum $\boldsymbol{f}_{\mathrm{MVDR},i}$, computed by a simulation framework that consists of the ray tracer, phased array model and AoA estimator. The simulated system is configured with directional patch antennas, $f_c = 2.4$ GHz, $M = 10$, $N = 1201$ and $K_{\mathrm{ss}} = 5$.

Deconvolved MVDR Spectrum

A general problem with AoA estimation methods is their inability to distinguish closely spaced sources. In a spatial spectrum, this can be observed as wide unpronounced peaks, due to the combination of multiple beams. A possible solution can be found in image processing theory, as deconvolution techniques are applied to deblur pictures. The same method can be used in spatial spectra to create more pronounced narrow peaks [Yan17].

The spatial spectrum is considered a convolution, as presented in Equation 3.11. With a known spatial spectrum and filter window $h(t)$, it should be possible to recover the original power distribution with narrow peaks by applying a deconvolution. However, two constraints complicate this procedure. First of all,

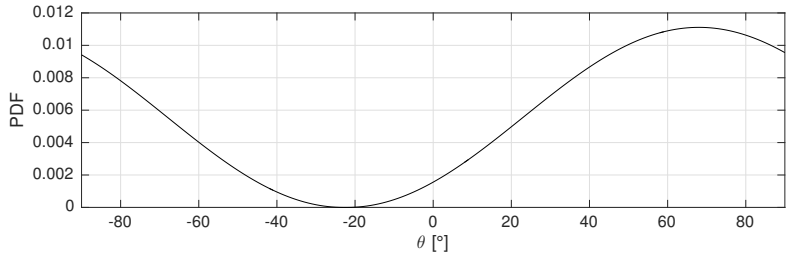

Figure 3.11: LOS fingerprint example: $\boldsymbol{f}_{\mathrm{LOS},i}$ for $\theta_{\mathrm{LOS}} = 68°$

deconvolution is a challenging calculation. In this research, the Richardson-Lucy algorithm is used with 10 iterations. Furthermore, a perfect knowledge of $h(t)$ is required. As explained before, this function remains unknown in MVDR beamformers. Therefore, the same Hanning window of Section 3.3.2 was selected empirically. Figure 3.10 demonstrates an MVDR deconvolution $\boldsymbol{f}_{\mathrm{MVDR,deconv},i}$, clearly manifesting narrowed peaks.

3.3.4 LOS Reference - Benchmark

In order to assess the performance of the proposed multipath assisted methods, a benchmark localization system is used. For fair comparison, this standard method relies on the same fingerprint based localization framework with $\boldsymbol{f}_i$ and $\boldsymbol{m}$ vectors, but only LOS directions are considered. The fingerprint vectors $\boldsymbol{f}_{\mathrm{LOS},i}$ are given by the $P_{\mathrm{sim,LOS}}(\theta)$ spatial spectra, as represented in Equation 3.13 and depicted in Figure 3.11. This function can be considered as the circular convolution of a discrete LOS peak with a 180° wide Hanning window.

$$P_{\mathrm{sim,LOS}}(\theta) = \frac{1}{2}\left(1 + \cos\left(\frac{\theta - \theta_{\mathrm{LOS}}}{2}\right)\right)_{\theta\in[-90°,90°]} \tag{3.13}$$

3.4 Measurement Data

The measurement vector $\boldsymbol{m}$ is the result of an AoA estimation technique, transforming the measured phase and amplitude information to the angular domain. Again, the vector can be represented as a discrete or continuous spatial spectrum, depending on the applied algorithm. The MVDR, MUSIC and ESPRIT estimators are considered in different configurations. The Beamscan

algorithm is omitted because of its inferior performance, which has been covered extensively in literature. Unlike fingerprint vectors, measurement vectors do not require normalization to a probability density function. However, a transformation to strictly positive values $\hat{P}(\theta) \in [0, 1]$ might simplify the matching algorithms and make plots more illustrative. Measurement processing is performed by the developed Matlab® localization framework, which is supported by the phased array toolbox. Forward backward averaging is applied in all situations, while the amount of spatial smoothing K_{ss} is selectable.

3.4.1 MVDR

The MVDR measurement vector $\boldsymbol{m}_{\text{MVDR}}$ represents a standard MVDR spatial spectrum $P_{\text{MVDR}}(\theta)$, which can be matched to the fingerprint vectors. The peaks in the MVDR spectrum indicate the AoA values, which can be represented as a discrete spatial spectrum $\boldsymbol{m}_{\text{MVDR,peaks}}$. This discrete spectrum can be circularly convolved with a Hanning window, as explained in Section 3.3.2. The result is again a continuous spatial spectrum, but it is characterized by more narrow peaks than the original $\boldsymbol{m}_{\text{MVDR}}$ vectors. The MVDR based measurement vectors are depicted in Figure 3.12a.

As explained in Section 3.3.3, another method to obtain a sharpened spatial spectrum with (more) narrow peaks, consists of the deconvolution of the MVDR spatial spectrum, resulting in $\boldsymbol{m}_{\text{MVDR,deconv}}$. The deconvolved spectrum can exhibit more peaks, which results in more discrete peaks in $\boldsymbol{m}_{\text{MVDR,deconv,peaks}}$. This discrete spectrum can again be circularly convolved, resulting in $\boldsymbol{m}_{\text{MVDR,deconv,peaks,circonv}}$. A deconvolved MVDR spectrum and its derivatives are illustrated in Figure 3.12b.

3.4.2 MUSIC and ESPRIT

The MUSIC and ESPRIT methods are generally used for high-resolution AoA estimation. As described in Section 2.4.3, these algorithms produce discrete angular outputs and no spatial spectrum. As a result no signal powers are assigned to the estimated angles, making weak reflections equally important to a LOS connection. A solution for this problem consists of combining the subspace based method with an MVDR spatial spectrum. In this approach, MUSIC or ESPRIT is used to find the discrete AoA values, while the signal powers (which can be considered as weights) for these particular angles are taken from the MVDR spatial spectrum. The result is a measurement vector $\boldsymbol{m}_{\text{MUSIC,peaks}}$ or $\boldsymbol{m}_{\text{ESPRIT,peaks}}$, representing a discrete power spectrum as displayed in Figure 3.13. This figure only depicts MUSIC results, which are

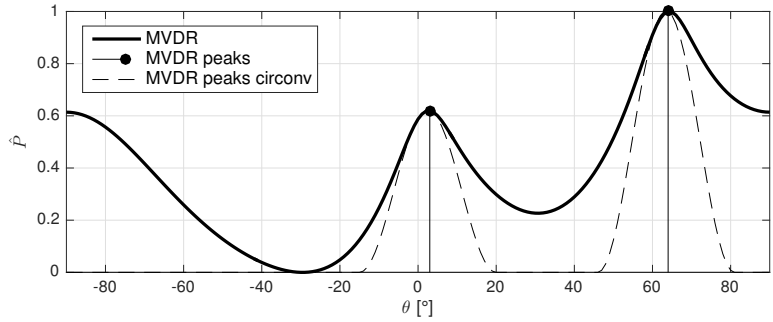

(a) MVDR based: $\boldsymbol{m}_{\mathrm{MVDR}}$, $\boldsymbol{m}_{\mathrm{MVDR,peaks}}$ and $\boldsymbol{m}_{\mathrm{MVDR,peaks,circonv}}$

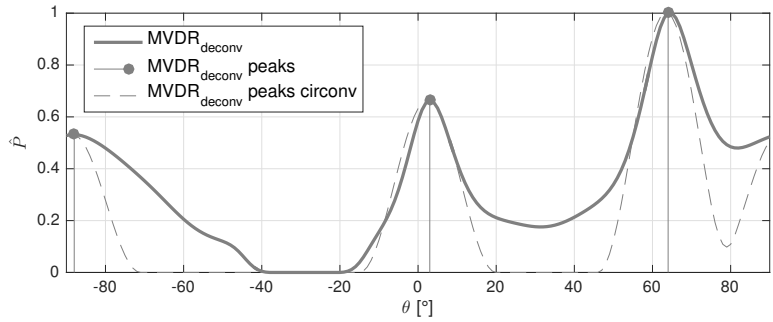

(b) Deconvolution based: $\boldsymbol{m}_{\mathrm{MVDR,deconv}}$, $\boldsymbol{m}_{\mathrm{MVDR,deconv,peaks}}$ and $\boldsymbol{m}_{\mathrm{MVDR,deconv,peaks,circonv}}$

Figure 3.12: Example measurement vectors based on an MVDR spatial spectrum

nearly identical to the ESPRIT vectors. A continuous version of the spectrum is created by the circular convolution with a Hanning window, as proposed in Section 3.3.2, resulting in $\boldsymbol{m}_{\mathrm{MUSIC,peaks,circonv}}$ or $\boldsymbol{m}_{\mathrm{ESPRIT,peaks,circonv}}$.

3.4.3 LOS Measurement - Benchmark

Classical AoA localization systems rely solely on the LOS direction, which is considered the strongest peak in the spatial spectrum. This approach is adopted for the localization benchmark, selecting only the strongest peak of the MVDR spatial spectrum as a discrete angle, resulting in measurement vector $\boldsymbol{m}_{\mathrm{LOS}}$, which is depicted in Figure 3.14.

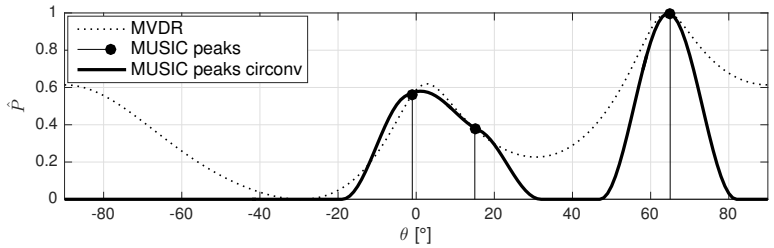

Figure 3.13: Example of MUSIC measurement vectors: $\boldsymbol{m}_{\text{MUSIC,peaks}}$ and $\boldsymbol{m}_{\text{MUSIC,peaks,circonv}}$

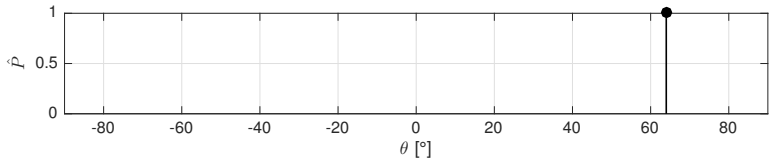

Figure 3.14: LOS measurement example: $\boldsymbol{m}_{\text{LOS}}$

3.5 Matching Algorithm

As described in Section 2.5, the kNN algorithm is an established method for position estimation in a fingerprinting system. This section describes a similar approach, tailored for the proposed localization framework.

The kNN method performs weighted averaging of k position estimates in order to achieve a higher resolution than the coarse training grid. However, the proposed multipath assisted system uses simulated training data with a much finer grid than survey based systems. Therefore, the averaging step is redundant, resulting in a 1NN approach. In order to find the nearest neighbor, the match between the measurement vector $\boldsymbol{m}$ and each fingerprint $\boldsymbol{f}_i$ is rated. Two matching algorithms are presented, relying on correlation coefficients or dot products of vectors.

3.5.1 Correlation Coefficients

The Pearson correlation coefficient $r_{\text{corr}}(i)$ can be used as a means for rating the resemblance between $\boldsymbol{m}$ and $\boldsymbol{f}_i$, as proposed in [dGBCK14]. A value close to 1 expresses high correlation, 0 means no correlation and -1 stands for negative

correlation. The absolute signal strength does not affect these values, since only the shape of the curves is considered.

$$\begin{aligned} r_{\text{corr}}(i) &= \frac{\text{cov}(\boldsymbol{f}_i, \boldsymbol{m})}{\sqrt{\text{var}(\boldsymbol{f}_i) \cdot \text{var}(\boldsymbol{m})}} \\ &= \frac{\int_{-90^\circ}^{90^\circ} (\boldsymbol{f}_i - \overline{\boldsymbol{f}_i}) \cdot (\boldsymbol{m} - \overline{\boldsymbol{m}}) d\theta}{\sqrt{\int_{-90^\circ}^{90^\circ} (\boldsymbol{f}_i - \overline{\boldsymbol{f}_i})^2 d\theta \cdot \int_{-90^\circ}^{90^\circ} (\boldsymbol{m} - \overline{\boldsymbol{m}})^2 d\theta}} \end{aligned} \tag{3.14}$$

3.5.2 Dot Product

$r_{\text{corr}}(i)$ relies on the covariance and variance of $\boldsymbol{m}$ and $\boldsymbol{f}_i$. These calculations involve a normalization of the vectors with their mean values. However, $\boldsymbol{f}_i$ represents a PDF, which is already strictly positive and normalized, as described by Equation 3.9. Also, $\boldsymbol{m}$ is a strictly positive function. Therefore, the normalization with mean values can be considered redundant. Also, the variance terms in the denominator can be eliminated. The remaining function $r_{\text{dotprod}}(i)$ is a simple dot product of $\boldsymbol{m}$ and $\boldsymbol{f}_i$, as described by Equation 3.15. The outcome is a strictly positive number that represents the similarity between $\boldsymbol{m}$ and $\boldsymbol{f}_i$. The omission of the $\text{var}(\boldsymbol{f}_i)$ term forms the strongest difference with the correlation based method.

$$r_{\text{dotprod}}(i) = \int_{-90^\circ}^{90^\circ} \boldsymbol{f}_i \cdot \boldsymbol{m} d\theta \tag{3.15}$$

3.5.3 Spatial Probability Density Function

The obtained coefficients $r_{\text{corr}}(i)$ and $r_{\text{dotprod}}(i)$ can be scaled linearly to the Spatial Probability Density Functions (SPDF) $r_{\text{SPDF,corr}}(i)$ and $r_{\text{SPDF,dotprod}}(i)$, representing the probability for each position $\boldsymbol{p}_i$.

$$r_{\text{SPDF,corr}}(i) = \frac{r_{\text{corr}}(i) + 1}{N_f + \sum_{i=1}^{N_f} r_{\text{corr}}(i)} \tag{3.16}$$

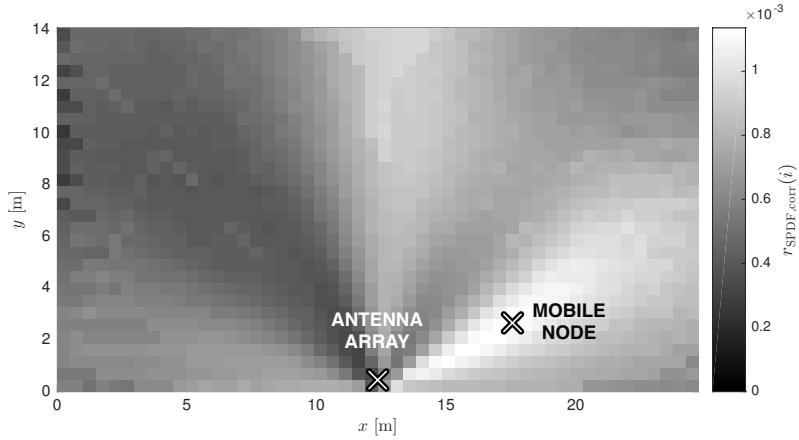

Figure 3.15: Example SPDF, based on the correlation coefficients of $\boldsymbol{m}_{\mathrm{MVDR}}$ and $\boldsymbol{f}_{\mathrm{raytrace,circonv},i}$

$$r_{\mathrm{SPDF,dotprod}}(i) = \frac{r_{\mathrm{dotprod}}(i)}{\sum_{i=1}^{N_f} r_{\mathrm{dotprod}}(i)} \tag{3.17}$$

The calculation of an SPDF is useful for each type of fingerprint vectors and measurement vectors, except when $\boldsymbol{m}$ and $\boldsymbol{f}_i$ both represent a discrete PDF. In this case, the dot products would fail when discrete peaks are not exactly aligned. Figure 3.15 depicts an example SPDF, based on the correlation coefficients of $\boldsymbol{m}_{\mathrm{MVDR}}$ and $\boldsymbol{f}_{\mathrm{raytrace,circonv},i}$. For this test, an experiment was performed in a 14.10 m by 24.70 m room with an $N_f = 1500$ reference grid. Figure 3.16 presents an example outcome of a LOS benchmark algorithm, based on the dot product of $\boldsymbol{m}_{\mathrm{LOS}}$ and $\boldsymbol{f}_{\mathrm{LOS},i}$.

Following Equation 2.30, the position estimate $\tilde{\boldsymbol{p}} = \boldsymbol{p}_j$ is determined by the highest value of the SPDF. However, it should be noted that a LOS benchmark SPDF for a single antenna array cannot be used for location estimation, as only one angular component is measured. The resulting outcome is a line or beam, as illustrated by Figure 3.16.

$$j = \arg \max_{i \in \{1,\ldots,N_f\}} r_{\mathrm{SPDF}}(i) \tag{3.18}$$

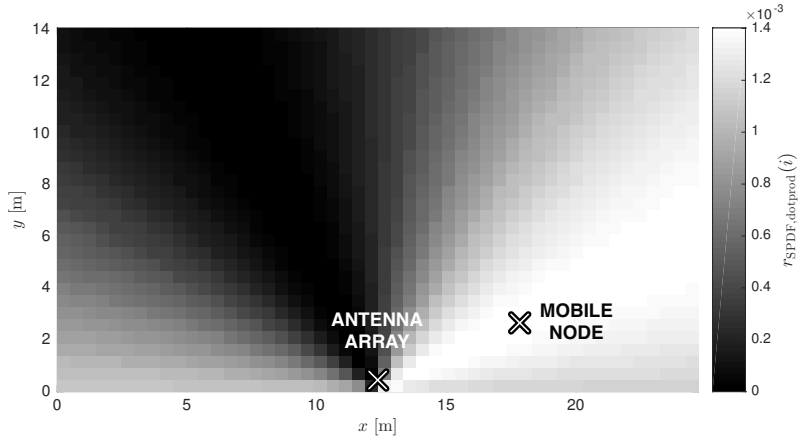

Figure 3.16: Example SPDF, based on the dot product of $\boldsymbol{m}_{\mathrm{LOS}}$ and $\boldsymbol{f}_{\mathrm{LOS},i}$

3.6 Multi-Anchor Configurations

Previous sections focused on the algorithms for localizing a mobile node with a single anchor system. However, a room can be equipped with multiple (Q) antenna arrays in order to increase the localization accuracy. In this case, the localization approach remains largely the same. For each of Q antenna arrays, a set of training data $\mathcal{T}_q$ is generated ($q \in \{1, \ldots, Q\}$). The position vectors $\boldsymbol{p}_i$ are the same across all sets of training data. An SPDF $r_{\mathrm{SPDF},q}(i)$ is calculated for each array, based on $\boldsymbol{m}_q$ and $\boldsymbol{f}_{q,i}$. In the last step, all SPDF vectors are linearly combined with equal weights, as prescribed by Equation 3.19.

$$r_{\mathrm{SPDF}}(i) = \frac{1}{Q} \sum_{q=1}^{Q} r_{\mathrm{SPDF},q}(i) \tag{3.19}$$

Figure 3.17 illustrates how the results of two anchor nodes can be merged to a single SPDF vector to obtain a more confined location estimate.

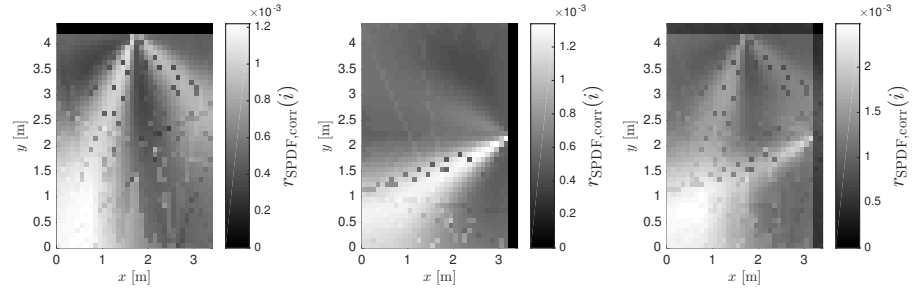

(a) SPDF for anchor 1 (b) SPDF for anchor 2 (c) Merged SPDF

Figure 3.17: Example of two merged SPDF vectors

3.7 Evaluation Criteria

3.7.1 Localization Error

The most straightforward measure to evaluate the performance of a localization system or algorithm is the localization error ϵ_{loc}. This quantity is defined as the euclidean distance between the estimated position $\tilde{\boldsymbol{p}}$ and the real position $\boldsymbol{p}$ of the mobile node. In order to compare localization errors in differently sized environments, the error can be normalized to the diagonal of the testing area, resulting in $\hat{\epsilon}_{\text{loc}}$, as explained in Section 2.6.6. Many localization systems converge to a single location estimate, making the localization error an adequate criterion for the assessment of the system performance.

However, the proposed multipath assisted localization technique is not a finalized system and intermediate results do not necessarily converge to a single position. For example, a single anchor approach could converge to two distinct positions. If the wrong position is selected, this results in a very large localization error, while the SPDF 'almost' predicts the correct position. In this case, the algorithm should still be considered very valuable, as auxiliary methods can easily result in a very accurate location estimate (e.g., dead reckoning techniques, an extra anchor node, etc.). This matter is illustrated by Figure 3.18, depicting an SPDF for a NLOS measurement, converging to two positions. The wrong one is selected as position estimate $\tilde{\boldsymbol{p}}$, resulting in a large localization error, undervaluing the performance of the algorithm.

Another shortcoming of localization errors is related to the benchmark algorithms. As explained in Section 3.5.3, no location estimate $\tilde{\boldsymbol{p}}$ can be determined for a single anchor node system with the LOS benchmark approach.

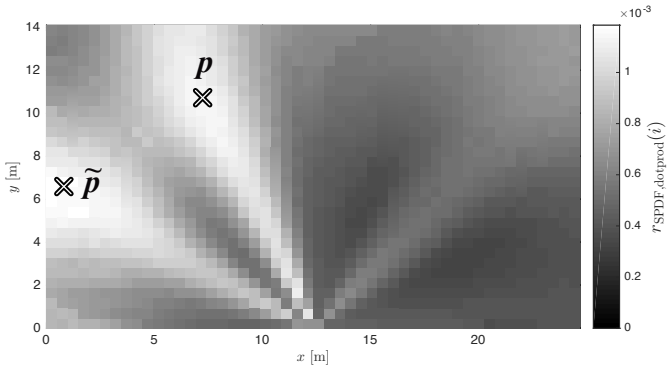

Figure 3.18: SPDF example for a NLOS measurement, resulting in a large localization error ϵ_{loc} and a small surface interval.

As such, it is impossible to compare the multipath assisted algorithms to the LOS benchmark method.

3.7.2 Surface Interval

In order to overcome the ϵ_{loc} related problems, a new measure is proposed for rating the accuracy of the system. The 'Surface Interval' (SI) is a dimensionless quantity between 0 and 1, representing the percentile of the SPDF that contains the real position $\boldsymbol{p}$, as expressed in Equation 3.20. Hence, SI indicates the fraction of the room surface that should be isolated to contain $\boldsymbol{p}$. Obviously, an SI value close to zero represents a high accuracy.

$$SI = \mathrm{P}\left(r_{\mathrm{SPDF}}(i) > r_{\mathrm{SPDF}}(\boldsymbol{p})\right) \tag{3.20}$$

3.7.3 Overall System Accuracy

The $\hat{\epsilon}_{\mathrm{loc}}$ and SI parameters provide information on a single position estimation. However, for an overall accuracy assessment in a certain environment, multiple localization tests are performed along a uniformly distributed grid of mobile node positions in the room. As a result, the $\hat{\epsilon}_{\mathrm{loc}}$ and SI values can be represented on a floor plan. Figures 3.19a and 3.19b demonstrate these results for a 9 x 5 test grid in a 14.10 m by 24.70 m room. This method forms a useful tool for the spatial representation of the accuracy, but a precise comparison of localization systems is impossible with this approach. Therefore, a Cumulative Density Function

(CDF) can be used for the representation of $\hat{\epsilon}_{\mathrm{loc}}$ and *SI* values, as depicted in Figures 3.19c and 3.19d. However, when a large number of configurations is evaluated, the CDF approach is inadequate. Therefore, the CDF functions are reduced to just three values: the 50^{th} percentile P50 (i.e. the median value), the 95^{th} percentile P95, and the mean value. A listing of P50, P95 and mean values of the $\hat{\epsilon}_{\mathrm{loc}}$ and *SI* parameters forms an ideal tool for the evaluation and comparison of system accuracies. As an example, Table 3.1 lists the equivalent values for Figure 3.19.

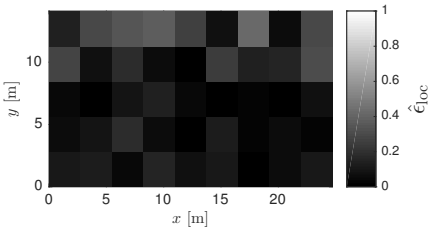

(a) Spatial distribution: $\hat{\epsilon}_{\mathrm{loc}}$

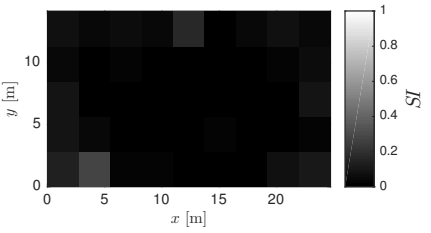

(b) Spatial distribution: *SI*

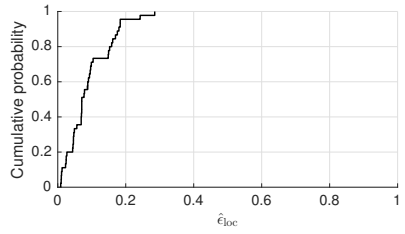

(c) CDF: $\hat{\epsilon}_{\mathrm{loc}}$

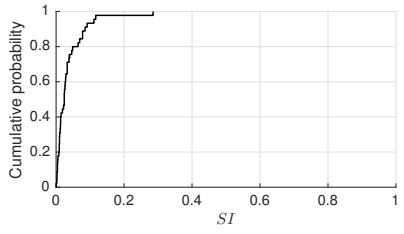

(d) CDF: *SI*

Figure 3.19: Example of the spatial distribution and CDF of $\hat{\epsilon}_{\mathrm{loc}}$ and *SI* values. Localization algorithm based on the correlation coefficients of $\boldsymbol{m}_{\mathrm{MVDR}}$ (LOS, $K_{\mathrm{ss}} = 5$) and $\boldsymbol{f}_{\mathrm{raytrace,circonv},i}$

The P50 and P95 surface intervals form an objective tool for the evaluation of localization accuracy: a P50 = 0.50 or P95 = 0.95 value indicates a completely random localization algorithm. In another respect, if 50% (or 95%) of the SPDF should be selected for a 50% (or 95%) probability of including position $\boldsymbol{p}$, the system can be considered useless.

The localization errors $\hat{\epsilon}_{\mathrm{loc}}$ are not omitted in the evaluations because they still provide the most tangible measure of localization accuracy. Also they enable the comparison to localization systems in literature. Throughout this work, the 'accuracy' or 'performance' of localization algorithms is described. These terms

Table 3.1: Example of the mean, P50 and P95 values of $\hat{\epsilon}_{\text{loc}}$ and *SI* for the results of Figure 3.19

$\hat{\epsilon}_{\text{loc}}$			*SI*		
mean	P50	P95	mean	P50	P95
0.118	0.086	0.374	0.039	0.017	0.134

form a general reference to the $\hat{\epsilon}_{\text{loc}}$ and *SI* parameters. The 'robustness' of a system denotes the immunity to adverse influences (e.g., NLOS connections).

3.8 Conclusions Concerning the Proposed Localization Method

This chapter introduced a system for indoor multipath-assisted localization with AoA measurements. The approach is inspired by recent related research and established AoA techniques. The proposed multilateral system operates in the 2.4 GHz and 5 GHz bands and allows single anchor node operation. For the anchors, linear antenna arrays are assumed, positioned close to the walls. The localization process involves an offline and an online phase, in analogy to common fingerprinting systems.

In the offline phase, a reference set of training data is generated through multipath simulations. Therefore, a 2D ray tracing tool is developed according to the image method, simulating LOS and specularly reflected signal components in a rectangular room. A literature study on the material permittivity of common building materials (concrete, brick and plasterboard) in the 2.4 GHz and 5 GHz band allows simulations of reflected signal powers in various environments. For the calculation of fingerprint vectors $\boldsymbol{f}_i$, various options are suggested. The most straightforward approach includes the simulated signal components as a discrete spatial spectrum. By circularly convolving this spectrum with a hanning window, an artificial continuous spectrum is obtained. Another representation consists of a simulated MVDR spatial spectrum, which can be 'sharpened' by a deconvolution with a Hanning window. For comparison purposes, a LOS benchmark fingerprint is included.

In the online phase, an AoA measurement vector $\boldsymbol{m}$ is composed. Therefore, the MVDR, MUSIC and ESPRIT algorithms are considered, in combination with circular convolutions or deconvolutions with a Hanning window. As a result, 11 variations of $\boldsymbol{m}$ exist, including one LOS benchmark for comparison.

In order to estimate a location, the measurement vector $\boldsymbol{m}$ is matched to the fingerprints $\boldsymbol{f}_i$ by means of a matching algorithm. Two options are proposed, relying respectively on correlation coefficients or dot products. The result is a spatial probability density function that leads to the estimated location. In multi-anchor configurations, these SPDFs can be combined linearly.

For the evaluation of the localization accuracy, two quantities are proposed. $\hat{\epsilon}_{\mathrm{loc}}$ represents the localization error, relative to the room diagonal. The surface interval *SI* is a newly introduced quantity, expressing the percentile of the SPDF that contains the mobile node position $\boldsymbol{p}$. In large-scale tests, the P50, P95 and mean values of $\hat{\epsilon}_{\mathrm{loc}}$ and *SI* are compared.

A thorough evaluation of the proposed system can be found in Chapter 5, providing a step-by-step selection process for finding the most accurate matching algorithm and the best representation of $\boldsymbol{f}_i$ and $\boldsymbol{m}$. These tests are performed with real-world measurement data, obtained in field tests. The experimental setup for these AoA measurements is described in Chapter 4.

Chapter 4

Experimental Setup

In order to test and evaluate the algorithms of chapter 3 with data obtained in real-world situations, a measurement setup is designed and built. First of all, the requirements of the measurement system are determined in section 4.1. Possible analog and digital beamformer topologies are studied and tested in section 4.2. The final setup is discussed in section 4.3, describing a synthetic antenna array with a moving antenna. Section 4.4 contains a detailed description of array characteristics, including an assessment of cable phase deviation. Also, the antenna selection and its influence on AoA estimation performance is studied in this section. Section 4.4.4 contains a theoretical discussion of mutual coupling between array elements, followed by an evaluation of the designed system. In Section 4.5, the system is evaluated in multipath conditions. First, the detection of specular reflections is tested, followed by the evaluation of an AoA fingerprinting approach. The conclusions of this chapter can be found in section 4.6.

4.1 Requirements

Given the 2D simplification of the localization approach, the measurement setup should consist of a horizontally omnidirectional mobile transmitter and a uniform linear antenna array, delivering phase and amplitude information of the receiver channels. Although there is a link with MIMO communication systems (e.g., 802.11ac, LTE, UMTS, etc.), no communication capabilities are required for the evaluation of the proposed AoA localization algorithms. Therefore, unmodulated carrier frequencies are used in this early research stage, allowing

a simpler hardware setup. The focus of the hardware design is on features and flexibility, rather than building a finalized deployable system. The specifications of the antenna array can be summarized as follows:

- Only receive beamforming
- No communications
- Digital output of phase and amplitude information for each receiver channel, allowing processing in Matlab®
- Multiband operation (preferably 2.4 GHz and 5 GHz bands)
- Sampling frequency: of minor concern in this research stage, as it only influences the duration of the measurement campaign
- Size: large enough for receiving a sufficient amount of multipath components, but small enough to allow an effortless and economically justified installation. For example: a configuration for receiving one LOS component and four first order reflections ($L = 5$), combined with four spatial smoothing operations ($K_{\text{ss}} = 4$), requires a ten-element array ($M = 10$), according to Equation 2.28.
- Dynamic range: if the system is only aimed at LOS and first order reflected components, the required dynamic range can be determined by the multipath simulations of Section 3.2.5. For operation in all simulated environments, a dynamic range of 53 dB is required. However, a larger dynamic range could facilitate the reception of more multipath components in larger rooms.
- Flexible antenna positioning ($\lambda/2$ inter-element spacing in each frequency band)
- Directional antennas minimize the sensitivity to backside impinging signals, and also reduce the influence of objects or walls behind the array

The presented requirements only form a guideline for the hardware design choices. No strict minimum values are imposed for the antenna front-to-back ratio, array size, dynamic range, etc. These parameters can initially be overvalued, followed by an evaluation of their influence on AoA or location estimation.

4.2 Topologies

Receive beamformers can be found in a variety of applications, ranging from radar to communication systems. A study of possible architectures leads to two distinct design choices [BZR08, MW08], represented in Figure 4.1.

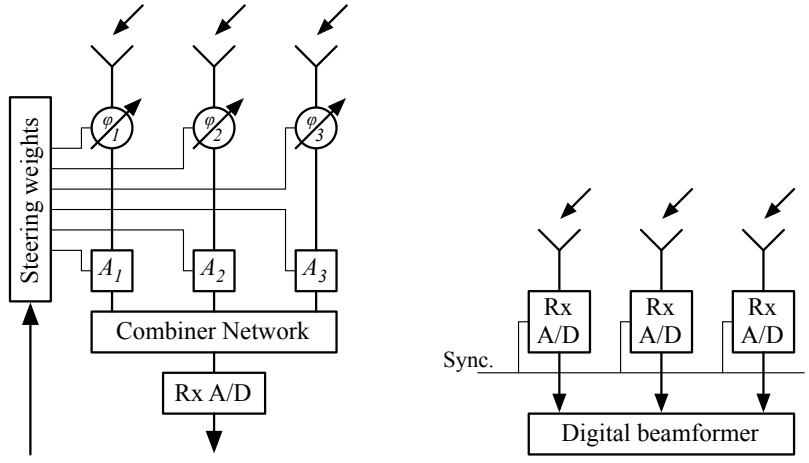

(a) Analog beamformer (b) Digital beamformer

Figure 4.1: Beamformer topologies

In analog beamformers, phase and amplitude weights are applied to each analog receiver channel with dedicated hardware, before combining all signals in a combiner network. The resulting beamformer output can be sampled with a single channel A/D converter. It is clear that this type of beamformer is not compatible with the proposed algorithms of chapter 2, given the absence of per-channel phase and amplitude information. For non-parametric algorithms, spatial spectra could be measured by applying complex weight factors. However, processing would occur during the measurements, preventing post measurement adaptations. Furthermore, this type of setup requires an intense effort in analog design, which is beyond the scope of this research.

Digital beamformers convert each receiver channel to the digital domain. This requires multiple synchronized A/D circuits in order to obtain time synchronized samples of each channel. The application of complex weight factors, the combination of channels and other signal processing steps are performed digitally. This approach splits the measurement and localization process, allowing intensive post measurement evaluations and optimizations of the localization algorithms. The digital beamforming topology still allows

a broad range of radio implementations for obtaining per-channel phase and amplitude information. A dedicated design with discrete components can be flexible and cost effective, excluding unnecessary functions. For example, each channel can be equipped with a Low Noise Amplifier (LNA), followed by a zero-IF receiver of which the output is sampled. However, this requires an intensive effort in RF design. Another option is the use of RF lab equipment, reducing design efforts and guaranteeing measurement accuracy, however at a high cost. In order to test the localization algorithms in a realistic MIMO communication system, a multi-channel software defined radio system can be used. This approach is irrelevant in the current phase, but can be considered in future research.

Figure 4.2a represents a digital beamforming setup that is conceived with a combination of dedicated components and lab equipment. At the transmitter side, a signal generator transmits a 2.470 GHz unmodulated signal. At the receiver side, each channel contains an ADL5521 [Ana13] LNA, realizing a 13 dB amplification. Also, AD8347 chips [Ana05] are used as mixers to bring received signals to an Intermediate Frequency (IF) of 10 MHz. At this frequency, phase differences and amplitudes can easily be measured with basic lab equipment, such as an oscilloscope. This is demonstrated in Figure 4.2b, depicting two channels. The experiment clearly indicates the feasibility of measuring the phase difference of RF signals, related to the antenna positions. However, measurement quality quickly degrades as the distance between transmitting and receiving antennas increases. Also, the number of channels is limited by the number of inputs on the measurement device. Therefore, a more accurate and flexible setup is proposed in the next paragraph.

4.3 Measurement Setup

Typical antenna arrays for receive beamforming sample the signals of multiple antennas simultaneously. Multiple synchronized receiver channels are required in such a setup, increasing the cost and complexity of hardware, and possibly affecting the accuracy of the system. Another disadvantage consists of mutual coupling between the antennas in the array, reducing AoA estimation performance [SSJ13]. For indoor localization and indoor propagation research purposes, a more accurate, flexible and less complex setup might be desirable. Therefore, a synthetic (sometimes called ‘virtual’) linear antenna array is proposed. This means that a single antenna is linearly translated during the measurements, picking up signals with different phases at different positions. Phase measurements are always performed relatively to a reference signal, which can be provided by an extra fixed antenna or a wired connection to

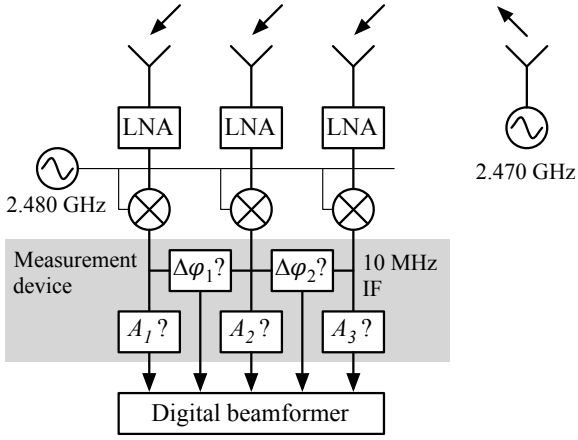

(a) Digital beamformer setup: block diagram

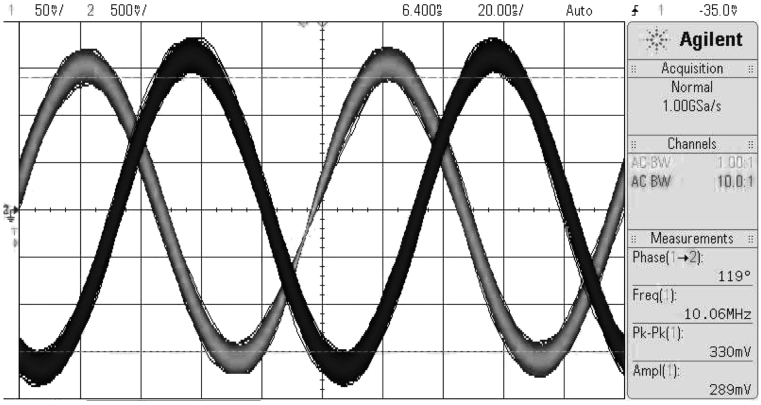

(b) Oscilloscope measurement of two phase shifted channels

Figure 4.2: Digital beamforming implementation

the mobile transmitter. Similar examples can be found in synthetic aperture radars [BZR08]. Also, an example was presented in [BLM+07], describing a circular synthetic array for GNSS purposes. In [TJL+10], a virtual URA is used for indoor channel sounding at 3 GHz. In contrast to expensive and complex multi-channel antenna arrays, this synthetic approach only requires one or two receiver channels. While the setup is not suitable for MIMO communication testing, it can be used for localization and indoor propagation tests in static environments. This means that the environment and transmitter position should not change during the measurements, which is only a minor drawback

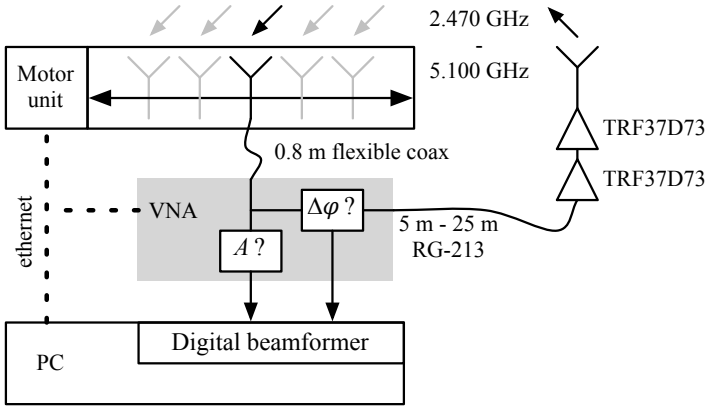

Figure 4.3: Schematic representation of the synthetic antenna array for AoA purposes

in this research phase. However, the synthetic approach is not compatible with real-world situations with a moving mobile node. In this case, a multi-channel array is required to sample all array elements simultaneously.

Figure 4.3 presents the hardware setup that is used for all further measurements and evaluations. It consists of two antennas, connected to an R&S® ZVH-8 vector network analyzer. The transmitting antenna represents the mobile node that is to be localized, while the receiving antenna is linearly translated by a motor unit. For the control and synchronization of antenna movements and network analyzer measurements, a PC running Matlab® is used. All measurement and control communications are performed over an ethernet network.

For each antenna measurement, the vector network analyzer is configured at the frequency of interest, gathering 1201 samples with zero span. In contrast to common antenna arrays, no phase differences are measured between array elements. Instead, the S_{21} parameters between transmitting and receiving antenna are measured for each position of the array antenna. This means that a wired connection is provided between the vector network analyzer and the mobile node. A wired mobile node is currently considered acceptable, given the early stage of this research. Since the transmitter and receiver antenna are both connected to the network analyzer, all measurements are synchronized to the stationary mobile node position, eliminating further steps for the synchronization of array channels. If future tests require the removal of the wired connection, a stationary phase locked antenna can be added to the synthetic array for reference purposes.

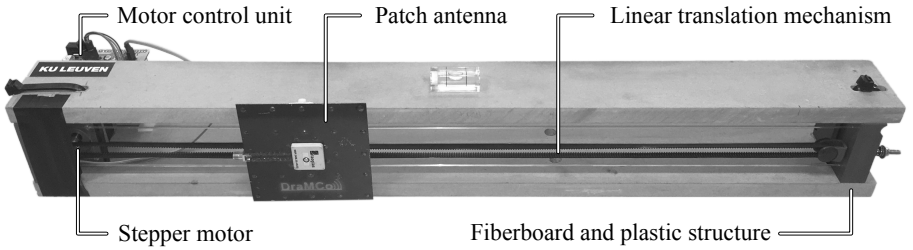

Figure 4.4: Synthetic antenna array setup

4.4 Characterization and Evaluation

4.4.1 Synthetic Array

A picture of the constructed synthetic antenna array is given in Figure 4.4. The motion controller consists of an ATmega328P microcontroller, a W5100 ethernet controller and a DRV8848 stepper motor driver. A linear motion is achieved with a stepper motor and a timing belt. The antenna positions can be set with a 169 µm precision, representing 0.50° phase precision at 2.47 GHz and 1.03° at 5.10 GHz. The total active width of the array is 548 mm, which is wide enough for 10 antenna measurements with a half-wavelength spacing at 2.47 GHz, or 19 antenna positions at 5.10 GHz. However, in this research just 10 positions with $\lambda/2$ spacing are used at 5.10 GHz to assure comparability with 2.47 GHz results. The size of the array was pragmatically chosen following the requirements of section 4.1, enabling a significant amount of signals that can be distinguished, while maintaining a workable size of the setup. The 2.47 GHz and 5.10 GHz ISM frequencies were selected for the minimal amount of interference from wireless communication systems in the considered test environments. As illustrated in Figure 4.4, the mechanical setup consists of plastic and fiberboard parts, minimizing the impact on signal propagation and antenna characteristics.

4.4.2 Cables

An important and easily overlooked aspect of the system consists of RF cabling. In contrast to traditional AoA systems, the mobile transmitter is wired to a network analyzer, requiring a long cable connection. In order to obtain accurate results, this cable should exhibit a low attenuation and high shielding effectiveness at the used frequencies, allowing a precise measurement of antenna signals without the cables themselves radiating. In this setup, a 5 m to 25 m

RG-213 coax is used, with 1.5 dB to 8.5 dB attenuation at 2.47 GHz and 2.7 dB to 18.1 dB attenuation at 5.10 GHz. Less lossy alternatives include LMR-400®, Ecoflex® 10 Plus, etc. In order to compensate for the signal losses, two TRF37D73 RF gain blocks are cascaded, achieving 37.4 dB and 25.2 dB amplification at respectively 2.47 GHz and 5.10 GHz [Tex14]. These amplifiers are positioned close to the mobile antenna instead of close to the network analyzer, boosting the radiated power while preventing excessive leakage of the long coaxial cable.

Another important cable is the short flexible connection between the moving antenna of the synthetic array and the network analyzer. This coaxial cable is flexed during measurements, possibly changing cable characteristics. Bending the cable alters its cylindrical shape and consequently also the electrical length, producing phase instability [MW08, Lam90]. The phase of the flexible cable in the setup was evaluated for antenna positions over the complete array width. The deviation from the mean phase at 2.47 GHz and 5.10 GHz is depicted in Figure 4.5. All phase measurements fall in a 0.24° interval at 2.47 GHz and a 0.97° interval at 5.10 GHz, as depicted in Figure 4.5. Better phase stable cables exist, but given the limited phase change (comparable to antenna movement accuracy), no significant influence on AoA estimation is expected in the evaluated setup. Since this cable connection is thin and flexible, it exhibits a higher attenuation per unit of length compared to more sturdy alternatives: 1.3 dB/m at 2.47 GHz and 2.6 dB/m at 5.10 GHz. Therefore, its length was limited to just 0.8 m, keeping the network analyzer close to the antenna array and requiring a long cable to the mobile node.

4.4.3 Antenna Selection vs. Array Performance

As explained in chapter 3, the array is always positioned against a wall of the room. Therefore, no open field conditions can be assumed. Instead, the walls possibly contain unknown metal structures, influencing antenna characteristics. This boundary condition is considered in the evaluation of the array and the selection of antenna elements. At the side of the mobile transmitter, a standard horizontally omnidirectional 2.4 GHz and 5 GHz dual band antenna (ACA-4HSRPP-2458) is used, generating a vertically polarized electric field. At the receiving array, two antenna options are evaluated: the same omnidirectional antenna and a directional patch antenna. The directional antenna was designed to limit negative influences of the nearby wall, and also minimize signals impinging on the back of the antenna. As stated before, these signals cannot be distinguished from the signals that impinge on the front, reducing system performance. The directional antenna is based on the Taoglas® WDP.2458.25.4.B.02 dual band (2.4 GHz and 5 GHz) ceramic patch [Tao15]

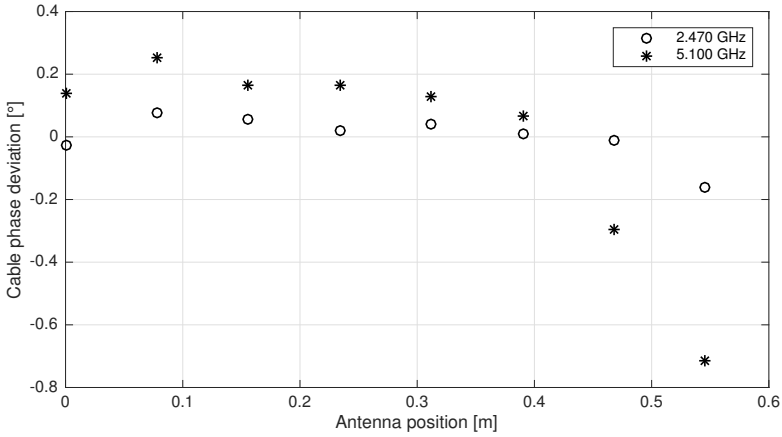

Figure 4.5: Phase deviation introduced by coax flexure with antenna movements

and is depicted in Figure 4.4. A dual band antenna was selected because it enables localization testing in both bands, without replacing antennas. The patch is mounted on a 100 mm x 100 mm conductor-backed coplanar waveguide with 50 Ω feed line [Sim01]. The radiation patterns at 2.47 GHz and 5.10 GHz were evaluated in an anechoic room. Figure 4.6 depicts the 0° elevation cut of the vertically polarized radiation pattern at both frequencies. The measured front-to-back ratio is 8.8 dB at 2.47 GHz and 7.5 dB at 5.10 GHz, providing a substantial attenuation of signals that impinge on the backside of the array. At 2.47 GHz, a half power beam width of 125° is obtained, while 50° is obtained at 5.1 GHz. As a result, signals impinging at the sides of the array field of view will see an unwanted significant reduction. An improvement of antenna characteristics can be achieved through further antenna development, however this is currently no research goal.

AoA Estimation Performance

In order to evaluate the AoA estimation capabilities of the array for the omnidirectional antenna and the directional patch antenna, four scenarios are considered. In the first test, the array with the patch antenna is placed in an anechoic room and the AoA of a LOS signal (θ_{LOS}) varies from $-90°$ to $90°$ in $5°$ steps. These AoA values are estimated with an MVDR algorithm. After this test in an ideal environment, a worst-case test scenario is considered: the antenna array is placed against a metal fence in an open space, as presented

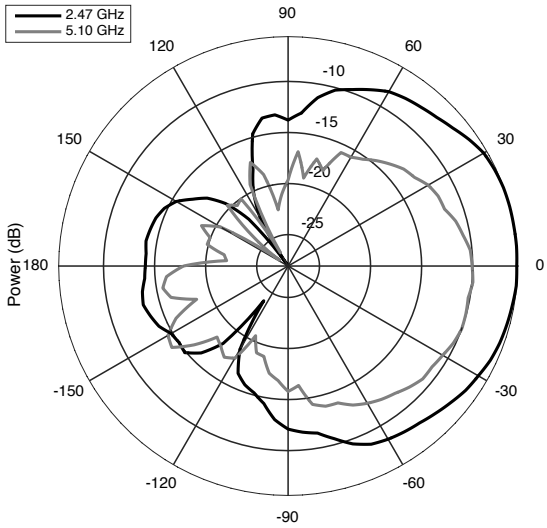

Figure 4.6: 0° elevation, vertically polarized radiation pattern of the patch antenna (0°=broadside)

in Figure 4.7. The omnidirectional transmitter is placed 4 m away from the array on 37 positions with 5° spacing, covering the complete $\{-90°, ..., 90°\}$ field of view. In this setup, the array is first equipped with the omnidirectional antenna. In order to observe the influence of the fence, a second evaluation is performed with pyramidal RF absorbers (Eccosorb® VHP-8 [Eme10]) placed between the array and the fence, reducing reflections and influences on antenna characteristics. This effect makes the setup more preferable from a technical point of view, however given the price and dimensions of pyramidal RF absorbers, a more cost efficient and compact alternative was tested: the directional patch antenna.

Figure 4.8 depicts an example of the MVDR spatial spectra for a θ_{LOS} of $-15°$ in the four considered configurations. In these tests, no spatial smoothing was applied. In the anechoic room, a sharp peak can be distinguished in the spectrum. The patch antenna against the metallic fence also results in a clear peak. However, the setup with an omnidirectional receiver clearly underperforms, an effect that can be mitigated with RF absorbers.

For the overall evaluation and comparison of the performance, two criteria are studied. The first and most straight-forward criterion is the error of the estimated θ_{LOS} direction, denoted as $\epsilon(\tilde{\theta}_{\mathrm{LOS}})$. This can simply be defined as the difference between the real θ_{LOS} of the impinging signal, and the estimated

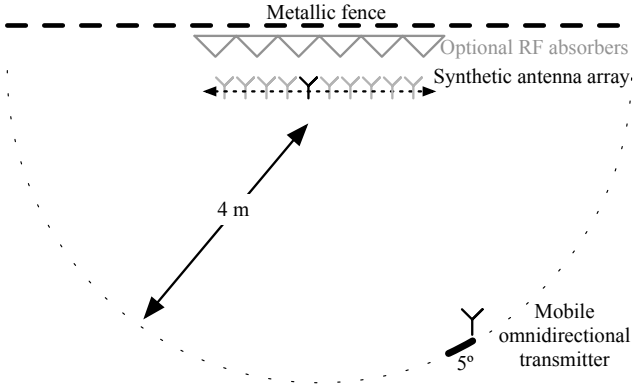

Figure 4.7: Test setup for the performance evaluation of the synthetic antenna array

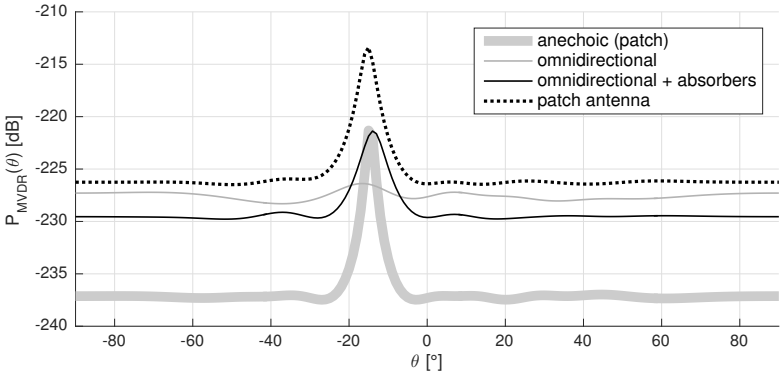

Figure 4.8: Example MVDR spatial spectra for a θ_{LOS} of $-15°$ in four test configurations at 2.47 GHz

$\tilde{\theta}_{\text{LOS}}$ value (i.e. the largest peak in the spatial spectrum), as expressed in Equation 4.1.

$$\tilde{\theta}_{\text{LOS}} = \arg \max_{\theta \in \{-90°,\ldots,90°\}} [P_{MVDR}(\theta, \theta_{\text{LOS}})] \tag{4.1}$$

$$|\epsilon(\theta_{\text{LOS}})| = |\theta_{\text{LOS}} - \tilde{\theta}_{\text{LOS}}| \tag{4.2}$$

Figure 4.9 depicts the AoA estimation errors for a 2.47 GHz and 5.10 GHz configuration. The results clearly demonstrate that an array of omnidirectional antennas positioned against a wall results in large errors over the complete field of view, resulting in highly inaccurate AoA estimation, especially in the 2.47 GHz case. Results improve significantly when absorbers are added or when a directional patch antenna is used. The $< 180°$ half power beam width of the directional antenna can be noticed in these results, with larger errors at the sides of the field of view. Table 4.1 summarizes the mean values of all θ_{LOS} estimation errors $\overline{|\epsilon(\theta_{\text{LOS}})|}$, confirming the conclusion that the patch antenna outperforms the omnidirectional antenna. However, these mean values should not be considered as a sound evaluation criterion: some tests exhibit AoA estimation errors close to 180° at the sides of the field of view. These large errors skew mean values, but they do not necessarily represent system underperformance, as $-90°$ and 90° are theoretically indiscernable. Therefore, a second evaluation criterion is introduced.

The second criterion studies the shape of the spatial spectrum instead of the position of the highest peak. Since only one signal impinges on the array, there should be a single sharp peak in the spatial spectrum. However, the structure of the array and the metallic fence might degrade performance, introducing wider and even extra peaks in the spatial spectrum, as presented in Figure 4.8. In order to evaluate this phenomenon, all spatial spectra are first normalized to values between 0 and 1, denoted as $\hat{P}_{MVDR}(\theta, \theta_{\text{LOS}})$. For each θ_{LOS} measurement, the mean value of the normalized spectrum is calculated, as expressed in Equation 4.3. The resulting value of $\overline{\hat{P}_{MVDR}}(\theta_{\text{LOS}})$ represents the surface beneath the normalized curve and should be as low as possible, indicating a single sharp peak.

$$\overline{\hat{P}_{MVDR}}(\theta_{\text{LOS}}) = \frac{1}{180} \cdot \int_{-90°}^{90°} \frac{P_{MVDR}(\theta, \theta_{\text{LOS}}) - \min_{\theta}[P_{MVDR}(\theta, \theta_{\text{LOS}})]}{\max_{\theta}[P_{MVDR}(\theta, \theta_{\text{LOS}}) - \min_{\theta}[P_{MVDR}(\theta, \theta_{\text{LOS}})]]} d\theta \tag{4.3}$$

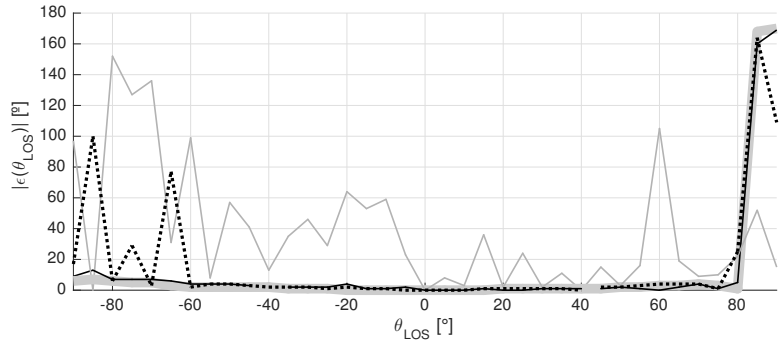

(a) 2.47 GHz

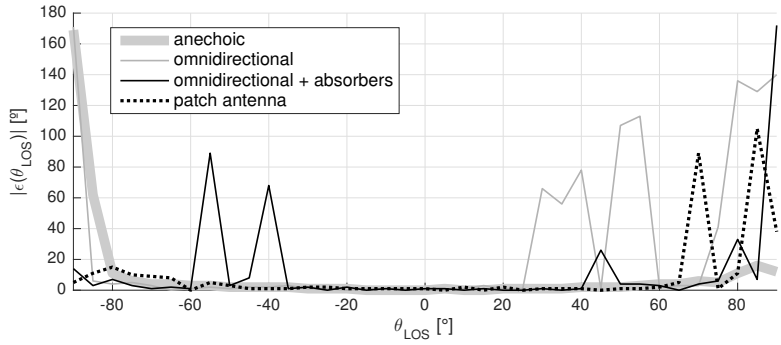

(b) 5.10 GHz

Figure 4.9: AoA estimation errors $|\epsilon(\theta_{\text{LOS}})|$ for three antenna configurations

$\overline{\hat{P}_{MVDR}(\theta_{\text{LOS}})}$ can be studied for each setup with Figure 4.10. The graphs illustrate that the accuracy of each configuration decreases towards the sides of the field of view. Also, the superior performance in an anechoic room is clearly demonstrated at 2.47 GHz and 5.10 GHz. In order to facilitate a further comparison of $\overline{\hat{P}_{MVDR}(\theta_{\text{LOS}})}$ values for each configuration, these values are averaged over all θ_{LOS} angles. This results in a single value for each configuration, denoted as $\overline{\overline{\hat{P}_{MVDR}(\theta_{\text{LOS}})}}$.

At 2.47 GHz, the setup with an omnidirectional antenna exhibits the highest $\overline{\hat{P}_{MVDR}(\theta_{\text{LOS}})}$ values, indicating poor performance due to multiple (wide) peaks in the spatial spectrum. This is improved by adding RF absorbers. The setup with a patch antenna even performs slightly better than the setup with absorbers. At 5.10 GHz, the results are less pronounced, so the mean values in Table 4.1

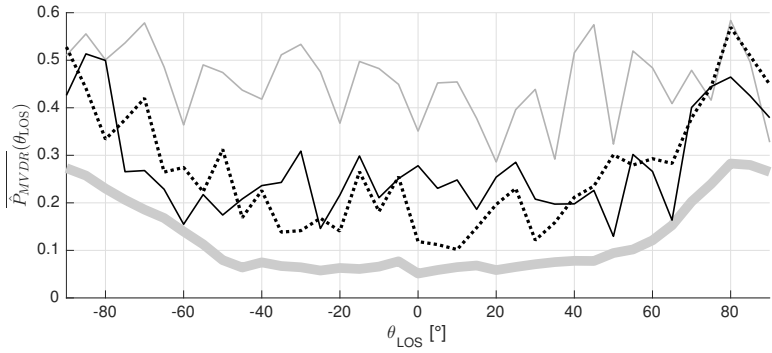

(a) 2.47 GHz

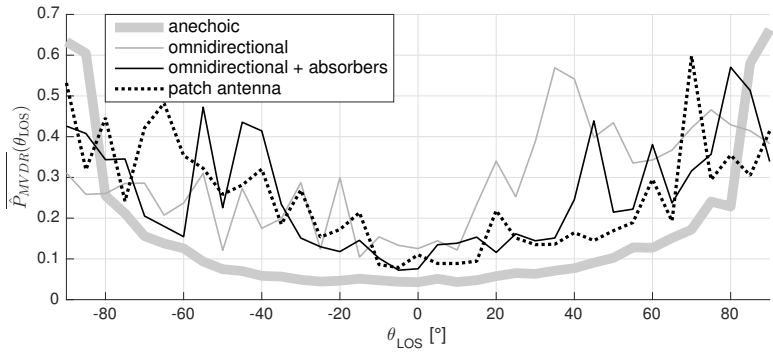

(b) 5.10 GHz

Figure 4.10: $\overline{\hat{P}_{MVDR}(\theta_{\mathrm{LOS}})}$ in the four test configurations

are studied, leading to the same conclusion: the setup with a patch antenna performs best. Table 4.1 also illustrates that the measurements against the metallic fence yield better results at 5.10 GHz than at 2.47 GHz. This does not necessarily mean that the system always performs better in the 5 GHz band. Instead, the metallic fence might just have a more detrimental effect in the 2.4 GHz band. This hypothesis is supported by the superior results of the 2.47 GHz setup in the anechoic room.

The most important conclusion is clearly illustrated by $\overline{|\epsilon(\theta_{\mathrm{LOS}})|}$ and $\overline{\hat{P}_{MVDR}(\theta_{\mathrm{LOS}})}$ values in Table 4.1: AoA estimation accuracy is significantly improved by using a patch antenna instead of an omnidirectional antenna. These results can be attributed to the directivity of the antenna.

Table 4.1: Evaluation of array AoA estimation performance in four test setups at 2.47 GHz and 5.10 GHz

	2.47 GHz		5.10 GHz	
	$\overline{\lvert\epsilon(\theta_{\mathrm{LOS}})\rvert}$	$\overline{\overline{\hat{P}_{MVDR}(\theta_{\mathrm{LOS}})}}$	$\overline{\lvert\epsilon(\theta_{\mathrm{LOS}})\rvert}$	$\overline{\overline{\hat{P}_{MVDR}(\theta_{\mathrm{LOS}})}}$
omnidirectional	38.43°	0.4552	29.35°	0.2901
omni. + absorbers	11.57°	0.2744	12.68°	0.2560
patch	15.65°	0.2702	9.14°	0.2509
anechoic	11.00°	0.1258	9.32°	0.1558

4.4.4 Mutual Coupling

In common receiving phased array systems, the impinging wavefronts are sampled by multiple receiver channels, as explained in section 2.4. For the calculation of AoA values, algorithms rely on accurate phase and amplitude measurements. However, physical antenna arrays suffer from mutual coupling, an interaction between antenna elements that alters array characteristics [SSJ13]. When a signal impinges on an antenna, a current is generated. This current again produces an electromagnetic field that influences nearby antennas and vice versa. This effect influences antenna impedances, radar cross sections, array steering vectors, radiation patterns and resolutions. As a result, mutual coupling can heavily affect the performance of phased array systems. For example, communication systems suffer from reduced interference suppression as unwanted signals cannot be nulled efficiently. In AoA localization systems, antenna coupling has been identified as a main contributor to AoA estimation errors [YNH12].

The synthetic antenna array that is used in this research consists of a single antenna, preventing negative mutual coupling effects. This makes the setup an ideal instrument for a hardware independent evaluation of localization algorithms, delivering ideal samples of the impinging wavefronts. However, mutual coupling could be added artificially to emulate a common multi-channel array and evaluate system performance in these conditions.

Various methods have been studied for the compensation of mutual coupling [LHL09]. The goal of these methods is the removal of the coupling effect from measurement values. The Conventional Mutual Impedance Method (CMIM) relies on the calculation of a mutual impedance by considering the array in transmitting mode, with open-circuit antenna termination. The Receiving Mutual Impedance method (RMIM) assumes known Z_L antenna terminations for an array in receive mode. The full-wave method relies on a known plane wave excitation of the array antennas and knowledge of antenna parameters in order

to calculate a compensation matrix for the calculation of uncoupled antenna voltages. A fourth method involves calibration of the array manifold. By applying a distortion matrix, a 'true' array manifold can be achieved. Thorough evaluations in [HL06] and [LHL09] indicated superior performance for the RMIM method.

RMIM method

In this research, the RMIM method is applied inversely: instead of counteracting mutual coupling, it is artificially added to the ideal measurement values. Therefore, the Receiving Mutual Impedance (RMI) $Z_t^{k,i}$ is introduced, expressing the influence of array element i on element k in receive mode [LH10].

In a common M-element ULA, all antennas are terminated with a Z_L load. Therefore, the induced currents I_k result in the antenna voltages V_k:

$$V_k = Z_L I_k \tag{4.4}$$

Also, the antenna voltage can be expressed as the sum of the induced voltage due to the impinging wavefront (U_k), and the voltage due to antenna coupling (W_k).

$$V_k = U_k + W_k \tag{4.5}$$

The voltage W_k in array element k is calculated as the sum of all coupling induced voltages:

$$W_k = Z_t^{k,1} I_1 + Z_t^{k,2} I_2 + \ldots + Z_t^{k,k-1} I_{k-1} + Z_t^{k,k+1} I_{k+1} + \ldots + Z_t^{k,N} I_N \tag{4.6}$$

Combining the equations 4.4, 4.5 and 4.6 results in matrix Equation 4.7, expressing the relationship between U_k and V_k. This equation is normally used to remove the mutually coupled voltage components from the measured antenna voltages V_k, leading to U_k, depending only on the impinging wavefronts. In this research the equation is used inversely, calculating V_k by artificially adding antenna coupling.

$$\begin{bmatrix} 1 & -\frac{Z_t^{1,2}}{Z_L} & \dots & -\frac{Z_t^{1,N-1}}{Z_L} & -\frac{Z_t^{1,N}}{Z_L} \\ -\frac{Z_t^{2,1}}{Z_L} & 1 & \dots & -\frac{Z_t^{2,N-1}}{Z_L} & -\frac{Z_t^{2,N}}{Z_L} \\ \vdots & \vdots & \ddots & \vdots & \vdots \\ -\frac{Z_t^{N-1,1}}{Z_L} & -\frac{Z_t^{N-1,2}}{Z_L} & \dots & 1 & -\frac{Z_t^{N-1,N}}{Z_L} \\ -\frac{Z_t^{N,1}}{Z_L} & -\frac{Z_t^{N,2}}{Z_L} & \dots & -\frac{Z_t^{N,N-1}}{Z_L} & 1 \end{bmatrix} \times \begin{bmatrix} V_1 \\ V_2 \\ \vdots \\ V_{N-1} \\ V_N \end{bmatrix} = \begin{bmatrix} U_1 \\ U_2 \\ \vdots \\ U_{N-1} \\ U_N \end{bmatrix} \tag{4.7}$$

Remark that ULA structures with identical array elements are symmetrical. Due to antenna reciprocity, the following equality holds: $Z_t^{k,i} = Z_t^{i,k}$. Furthermore, the RMI values for equally spaced antennas are equal: $Z_t^{1,2} = Z_t^{2,3} = \dots$ and $Z_t^{1,3} = Z_t^{2,4} = \dots$ etc. Therefore, an M-element ULA only requires the determination of $M-1$ RMI values.

In order to determine the RMI values, three voltages should be measured: V_k, V_i and U_k. The measurement setup contains a transmitter, generating a plane wave that impinges on the array under 0°. For the measurement of V_k and V_i, two identical receiver elements are required at positions i and k. For the synthetic antenna array, this requires a temporary addition of a second element. The measurement of U_k is performed with a single receiver element. Consequently, the $Z_t^{k,i}$ values can be calculated with the following equation:

$$Z_t^{k,i} = \frac{V_k - U_k}{I_i} = \frac{V_k - U_k}{V_i} Z_L \tag{4.8}$$

RMI measurement

The RMI was evaluated for the synthetic array with patch antenna at 2.47 GHz for 9 distinct inter-element distances, according to the previously explained method. The resistance R_t and reactance X_t values are depicted in Figure 4.11. The general trend of the curves shows similarity to the damped oscillating R_t and X_t values for dipoles, as reported in [HL06]. However, for the patch antennas larger RMI values can be remarked: $R_t = 30\ \Omega$ at 0.5λ distance, while dipoles exhibit $R_t < 20\ \Omega$ for $> 0.2\lambda$ distance. This can be attributed to the specific antenna design, affecting the current distribution and mutual coupling.

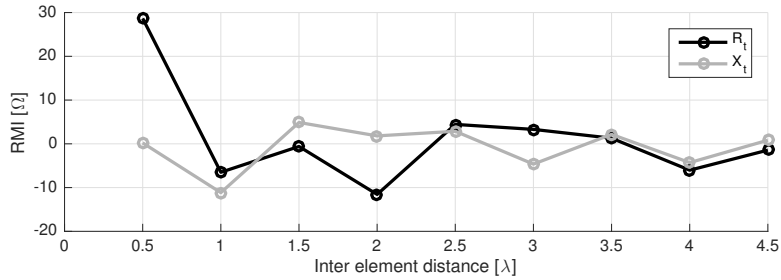

Figure 4.11: Measured receiving mutual resistance (R_t) and receiving mutual reactance (X_t) for the 2.47 GHz synthetic array.

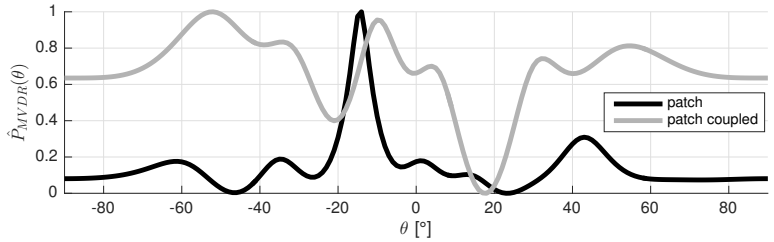

Figure 4.12: Example normalized MVDR spatial spectra for a $-15°$ θ_{LOS} in a 2.47 GHz patch antenna test configuration with and without mutual coupling

AoA estimation accuracy with mutual coupling

The measured RMI values are used for the evaluation of array performance in case of mutual coupling. Therefore, patch antenna tests of section 4.4.3 are evaluated with and without antenna coupling. Two types of spatial spectra are calculated for this setup, relying on U_k voltages (no coupling) or V_k voltages (with artificially added coupling). Figure 4.12 demonstrates the detrimental effect of antenna coupling on AoA estimation: due to the presence of multiple strong peaks in the spatial spectrum, accurate AoA estimation of the LOS component is impossible.

Figure 4.13 presents $|\epsilon(\theta_{\mathrm{LOS}})|$ and $\overline{\hat{P}_{MVDR}}(\theta_{\mathrm{LOS}})$ parameters for the coupled and uncoupled configuration. The coupled configuration exhibits very large AoA estimation errors over the whole field of view. Also $\overline{\hat{P}_{MVDR}}(\theta_{\mathrm{LOS}})$ values present severe underperformance of the coupled system. These inferior results were obtained in a setup with only LOS connections, as described in section 4.4.3. As the system is aimed at indoor NLOS multipath environments, mutual coupling

should be considered as a major concern in realistic multi-channel antenna arrays, requiring appropriate countermeasures. Spatial smoothing could improve results, as antenna coupling introduces correlation between array channels. Another option is the use of a mutual coupling elimination method like RMIM, as discussed before. The effectiveness of these methods cannot be tested in the current hardware setup, as the same methods are used for artificially adding mutual coupling. Therefore, further testing will exclude the effect of antenna coupling. The evaluation of the localization system performance with non-synthetic antenna arrays and coupling compensation methods (e.g., orthogonal polarization of neighboring antennas) is considered future work.

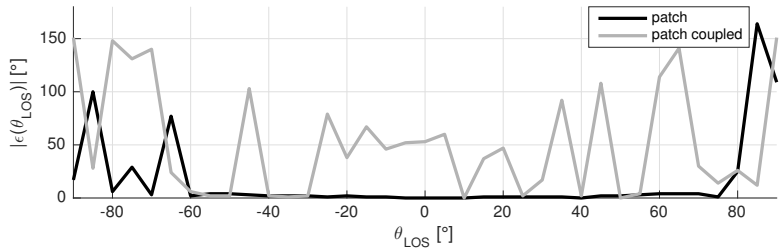

(a) AoA estimation errors $|\epsilon(\theta_{\mathrm{LOS}})|$

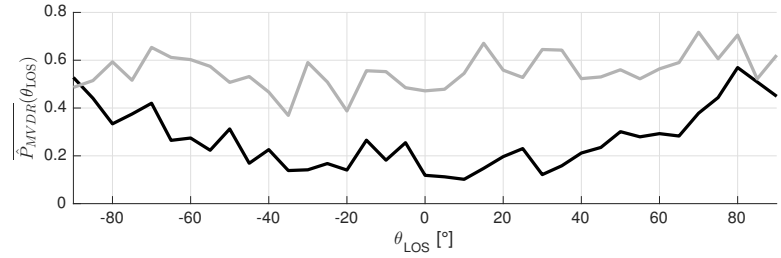

(b) Mean values of the normalized spectra: $\overline{\hat{P}_{MVDR}}(\theta_{\mathrm{LOS}})$

Figure 4.13: Evaluation of coupled and uncoupled patch antenna configurations

4.5 Feasibility for AoA Multipath-Aided Localization

Before evaluating the proposed AoA multipath assisted system, two tests are performed to assess the feasibility of the approach with the conceived synthetic

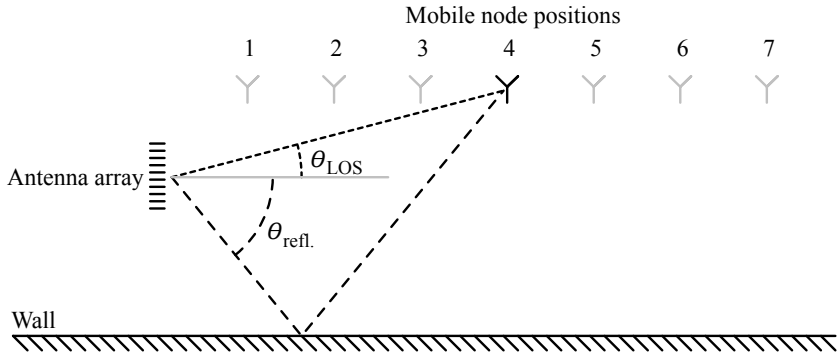

Figure 4.14: Test setup for the evaluation of wall reflections

array. While previous array evaluations focused on the detection of LOS signals, the following tests take multipath components into account.

4.5.1 Multipath Detection

Figure 4.14 presents a measurement setup in an open space with a single reflecting wall. The aim of this setup is to evaluate the discoverability of the first order specular reflection, which is assumed to produce the second highest peak in the MVDR spatial spectrum. The tests are performed at 2.47 GHz and 5.10 GHz in a setup with a brick wall and a concrete wall. The mobile node is positioned in 7 distinct positions, resulting in strictly negative θ_{LOS} angles and a variety of positive $\theta_{\text{refl.}}$ angles, as listed in Table 4.2.

The AoA estimation errors of the first order reflections $|\epsilon(\theta_{\text{refl.}})|$ are listed in Table 4.2. These values illustrate how closely the expected reflection angles $\theta_{\text{refl.}}$ line up with the second highest peaks in the spatial spectra. For the calculation of MVDR spatial spectra, 5 spatial smoothings were applied. This configuration yields the best results, which is further elaborated in Section 4.5.2 and Section 5.2.4.

For the three closest positions of the mobile node ($\theta_{\text{refl.}} \geq 59°$), large AoA estimation errors can be observed. However, for $\theta_{\text{refl.}} < 59°$, AoA estimation of the reflected components can be considered successful. These findings are in line with the results of Figure 4.9, describing reduced performance at the sides of the field of view. In the $\theta_{\text{refl.}} < 59°$ domain, the brick wall produces very accurately detectable reflections at 2.47 GHz and 5.10 GHz, resulting in $|\epsilon(\theta_{\text{refl.}})| \leq 2°$. With a concrete wall, slightly larger AoA errors are observed, despite the larger material permittivity. A possible source of these inferior results could be found

in metallic reinforcement structures or other material inhomogeneities, causing additional scattered multipath components. In the frequency domain, slightly inferior results can be observed at 5.10 GHz with respect to the 2.47 GHz results. This conclusion is drawn from the $\theta_{\text{refl.}} < 59°$ results for a concrete wall, despite the limited number of measurements. A reason for the reduced performance at 5.10 GHz is found in the shorter wavelength, which results in a higher sensitivity to structural imperfections. Overall, the tests indicate that specular reflections can be detected with the synthetic antenna array, which is a necessary condition for the further evaluation of the system.

Table 4.2: Evaluation of AoA estimation performance of first order reflections in two test setups at 2.47 GHz and 5.10 GHz

		Mobile node positions						
		1	2	3	4	5	6	7
θ_{LOS} [°]		-45	-27	-19	-14	-12	-10	-8
$\theta_{\text{refl.}}$ [°]		79	68	59	52	45	40	36
		$\lvert\epsilon(\theta_{\text{refl.}})\rvert$ [°]						
2.47 GHz	Brick	56	2	1	2	0	2	1
	concrete	36	2	32	5	2	3	5
5.10 GHz	Brick	127	1	98	2	0	1	1
	Concrete	34	140	4	7	7	2	4

4.5.2 AoA Fingerprinting

The second feasibility test focuses on localization in a dense multipath environment. The test investigates if consistent and unique channel information can be obtained across multiple positions in a room. Therefore, a fingerprinting system is set up: training data is collected in an offline phase, followed by localization testing in an online phase. Training data consists of a set of MVDR spatial spectra, acquired along a grid before operation ($\boldsymbol{f}_i = P_{\text{MVDR}}(\theta)$). In the online phase, a new MVDR spectrum ($\boldsymbol{m} = P_{\text{MVDR}}(\theta)$) is obtained and correlated to the reference set $\mathcal{T}$ of spatial spectra. The location with the highest correlation coefficient is considered as the estimated position. This fingerprinting system exhibits a lot of similarity to the proposed multipath assisted localization approach. However, a labor intensive training phase is applied instead of ray tracing simulations, which is similar to the work presented in [GCGM09, RWK16, KWC13]. The results do not only provide information about the suitability of the hardware setup, but they also provide useful insights with regards to the proposed localization approach.

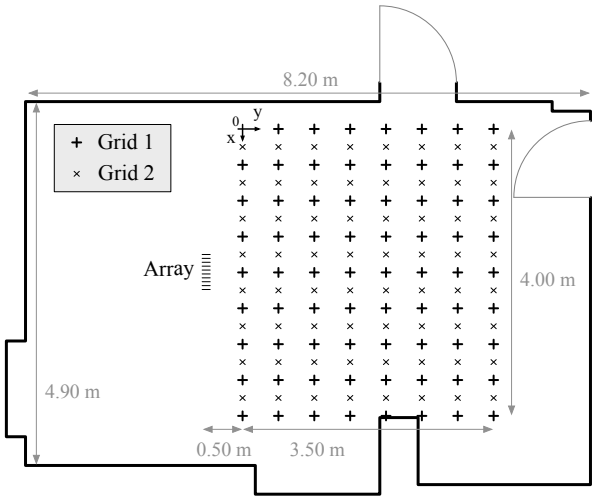

Figure 4.15: Test setup for the evaluation of an AoA fingerprinting system

Measurement setup

For the evaluation of the proposed system, a test area was considered in an empty room of 4.90 m x 8.20 m, as depicted in Figure 4.15. The building structure includes a variety of materials, e.g., plasterboard walls, pillars of reinforced concrete, metal doors and heaters, etc. guaranteeing a rich multipath environment that forms a unique propagation path for each possible location of the mobile node. The test area in this room consists of 2 grids with respectively 9x8 and 8x8 positions for the mobile node in a rectangular 4.00 m x 3.50 m area, denoted as grid 1 and grid 2. In order to evaluate the system, three test scenarios are considered. For each scenario, the 9x8 grid (grid 1) was used to generate a reference database of 72 spatial spectra. In the first test scenario, localization is evaluated for grid 1, i.e. the spatial spectra are obtained again on the same 9x8 grid that was used for the reference data. This approach is identical to the evaluations in [GCGM09, RWK16, OIS13] and can be considered as an ideal situation. The second test involves a less favorable scenario with NLOS connections. Therefore, LOS signals are obstructed with RF absorbers [Eme10]. In the third scenario, LOS measurements are performed along an 8x8 grid (grid 2) as demonstrated in Figure 4.15. This means that the system is tested for off-grid positions. All tests are performed with the synthetic antenna array in a 2.47 GHz configuration.

Table 4.3: Overall localization errors (in m) as a function of spatial smoothing operations in an AoA fingerprinting system

	K_{ss}	0	1	2	3	4	**5**	6	7	8
$\lvert\epsilon_{\text{loc}}\rvert$ [m]	Mean	1.72	1.57	1.66	1.40	1.20	**1.13**	1.13	1.19	1.28
	P50	1.58	1.46	1.55	1.12	1.00	**0.90**	1.00	1.03	1.12
	P95	3.79	3.58	3.54	3.41	3.21	**3.01**	3.35	3.01	3.01

Evaluation

Before evaluating the system accuracy in the three test scenarios, the optimal amount of spatial smoothing over all scenarios is determined. Given the limited number of antennas M, this is a trade-off between AoA accuracy (increases with more decorrelations K_{ss}) and the number of directions that can be detected L (reduced by the number of decorrelations). In order to study the effects of spatial smoothing, the localization errors for all the test scenarios (a total of 208 measurement points) and all possible K_{ss} values (0 to 8) are listed in Table 4.3. For these tests, the amount of spatial smoothing operations in reference data and measurement data was always considered equal. Table 4.3 lists the mean, 50th percentile (P50) and 95th percentile (P95) values of the localization errors (in m). The largest errors can clearly be observed for the lowest amount of spatial smoothing, resulting in a median localization error of 1.58 m for $K_{\text{ss}} = 0$. As K_{ss} increases, a higher localization accuracy is achieved. The errors reach a minimum for $K_{\text{ss}} = 5$, with a median error of 0.90 m and a maximum of four detectable multipath components ($L = 4$). Further increasing the amount of spatial smoothing results in higher localization errors, which is a result of insufficient multipath information ($L = 1$ for $K_{\text{ss}} = 8$). The outcome of 5 spatial smoothing operations is in line with the results of Section 5.2.4.

The accuracy of the fingerprinting system with $K_{\text{ss}} = 5$ is studied in Table 4.4 for each setup, listing the normalized localization errors $|\hat{\epsilon}_{\text{loc}}|$. Normalization is performed along the diagonal of the 3.5 m x 4.0 m testing area. It is clear that an ideal situation (on-grid, LOS) yields the best results with a 11.4% normalized median error and a 15.9% mean normalized error, which is a vast improvement over the 21.6% median value and 26.1% to 29.2% mean values that were reported in [GCGM09, RWK16]. In NLOS conditions, the median error almost doubles to 21.0%, providing information on possible real-world performance. Off-grid LOS localization errors present a clear degradation of accuracy in comparison to the on-grid setup, indicating the importance of a fine reference grid. This aspect is expected to be resolved in the proposed

Table 4.4: Localization errors (in m) in different setups, with $N = 5$

	Setup	mean	P50	P95
$\lvert\hat{\epsilon}_{\text{loc}}\rvert$	LOS, on-grid	0.159	0.114	0.465
	NLOS, on-grid	0.268	0.210	0.601
	LOS, off-grid	0.213	0.170	0.580

localization system, as ray tracing simulations can produce a fine reference data set. The P95 values of normalized localization errors exceed 46%. For applications demanding a highly reliable localization accuracy, extra antenna arrays and post processing algorithms (e.g., dead reckoning, Kalman filtering, etc.) could provide an outcome [MLVC09].

Overall, the AoA fingerprinting tests demonstrate the feasibility of exploiting the multipath for localization purposes with the developed synthetic antenna array at 2.47 GHz. In this setup, the optimal amount of spatial smoothing was fixed as $K_{\text{ss}} = 5$. In LOS on-grid conditions, the system outperforms previously reported solutions. Off-grid measurements indicated the importance of a fine reference grid.

4.6 Conclusions Concerning the Experimental Setup

This chapter presented a hardware implementation for AoA measurements. Analog and digital beamformers are studied and evaluated. Driven by flexibility, measurement accuracy and low design complexity, a synthetic antenna array is conceived. The system consists of a vector network analyzer and a single receiver antenna that moves across multiple positions. The uncomplicated setup provides highly accurate and flexible phase and amplitude measurements for AoA estimation. The setup is designed for indoor AoA research purposes only. It is not aimed at communication testing and the mobile transmitter is not wireless.

Various design parameters are investigated and highlighted, including cable specifications, antenna selection and mutual coupling between antennas. A study of coax cable flexure during the measurements indicates sufficient phase stability. For longer cables in the setup, cable attenuation is verified. The complete setup is equipped with different antennas and tested in an anechoic room and against a metallic fence, showing underperformance when the synthetic array is

equipped with a dipole antenna. This negative effect is reduced significantly by using a directional patch antenna. Furthermore, the dual band patch antenna enables measurements in the 2.4 GHz and 5 GHz band without hardware adjustments. Inherent to the synthetic array design is the lack of mutual coupling between array elements, which is considered an asset in this research phase. Coupling emulations show a strong negative effect on AoA estimation accuracy, a phenomenon that should be addressed in future multi-channel setups.

The resulting measurement setup meets the stated requirements of an accurate and flexible multiband receive beamforming system for placement against a wall. Furthermore, the system is tested in multipath environments, revealing that specular reflections from a concrete or brick wall can be measured. Also, an AoA fingerprinting system is evaluated with this setup, demonstrating localization in various conditions. These results confirm the essential conditions for the evaluation of the proposed localization system: with the conceived setup, multipath signals are measurable and can be exploited for localization purposes. Chapter 5 relies on large-scale field tests with this hardware setup in order to test the proposed multipath assisted localization method, evaluate hardware parameters and investigate environmental influences.

Chapter 5

System Performance

In previous chapters, AoA measurement hardware was presented and localization algorithms were proposed and theoretically discussed. This chapter brings both aspects together, enabling the assessment of localization performance in real-world situations. The measurements are performed in six different test environments, presented in Section 5.1. The first evaluations aim to find the best performing configuration of the localization algorithms in Section 5.2. Next, Section 5.3 studies the accuracy of ray tracing simulations. Section 5.4 investigates multiple hardware parameters of the antenna array and their effect on localization accuracy. The influence of antenna coupling is covered, followed by a study of the number of array elements and the number of array snapshots. In Section 5.5, localization results are compared for various single and multi-array configurations. Section 5.6 focuses on environmental influences such as floor and ceiling reflections, building materials and room sizes. All these evaluations are performed in the 2.4 GHz band, therefore a separate Section 5.7 is added for the discussion of system performance in the 5 GHz band. In Section 5.8, results of both frequency bands are combined. In Section 5.9, the achieved localization accuracies are compared to the results in scientific literature. This chapter concludes with a summary of the obtained results in Section 5.10.

5.1 Test Environments

In order to test, evaluate and configure the localization system, measurements are performed in multiple rectangular rooms. These test environments are

subdivided by measurement grids, uniformly distributing test positions of the mobile node. The selection of the rooms was based on the building materials, room sizes and overall measurement feasibility. In the selected areas, a variety of system configurations is tested, enabling the assessment of environmental influences and system parameters.

Figure 5.1 depicts the floor plans of all test setups, including the measurement grid, array positions and objects in the room. Three relatively small-sized rooms were selected for their varying building materials: TS_{brick}, $TS_{wallboard}$ and $TS_{concrete}$. These rooms are part of a larger building and contain some non-removable objects, representing realistic setups. Furthermore, three larger test setups were considered for the evaluation of room size influences: TS_{XL}, TS_{XXL} and TS_{XXXL}. These large rooms are empty sports halls with metal structures for basket ball rings attached to the walls. Each sports hall is connected to a storage area which possibly influences the propagation path. In order to minimize this effect, the arrays are always facing away from this area. Another -more practical- reason for this configuration is the limited cable length that prevented array positions against the shortest walls.

The antennas are always placed in the same horizontal plane at a height of 1.3 m, resulting in 0° elevation angles. Since ray tracing simulations only account for the walls of a rectangular room, the objects are not considered in multipath calculations and can therefore have an influence on system accuracy, causing extra multipath components. When obstacles are significantly lower than the antenna heights and feature a limited amount of metallic parts (e.g., tables), these objects are not expected to strongly interfere with the simulated multipath and can therefore be classified as 'unlikely influential'. Large objects and metal structures at antenna heights are more likely to influence the propagation channels and are classified as 'possibly influential'.

TS_{brick}: In the brick wall setup, a 4x6 measurement grid is established. For the reference set, a finer 0.11 m grid of 30x40 positions was simulated. In the setup, six array positions are considered: in the middle of each wall (A-D), in a corner under 45° (E_{45}), or in a corner along the room diagonal (E_{38}).

$TS_{wallboard}$: The wallboard setup is larger and contains more irregularities: a glass wall and a metallic whiteboard at antenna height. Four antenna positions are evaluated and a 4x7 measurement grid is applied. For ray tracing simulations, a 22x46 grid is used.

$TS_{concrete}$: This room with concrete walls has a square floor plan and no objects. A single array position is evaluated, leaving wall irregularities behind the array. For the measurements, a 5x5 grid is used. Reference set simulations are performed with a 38x38 grid.

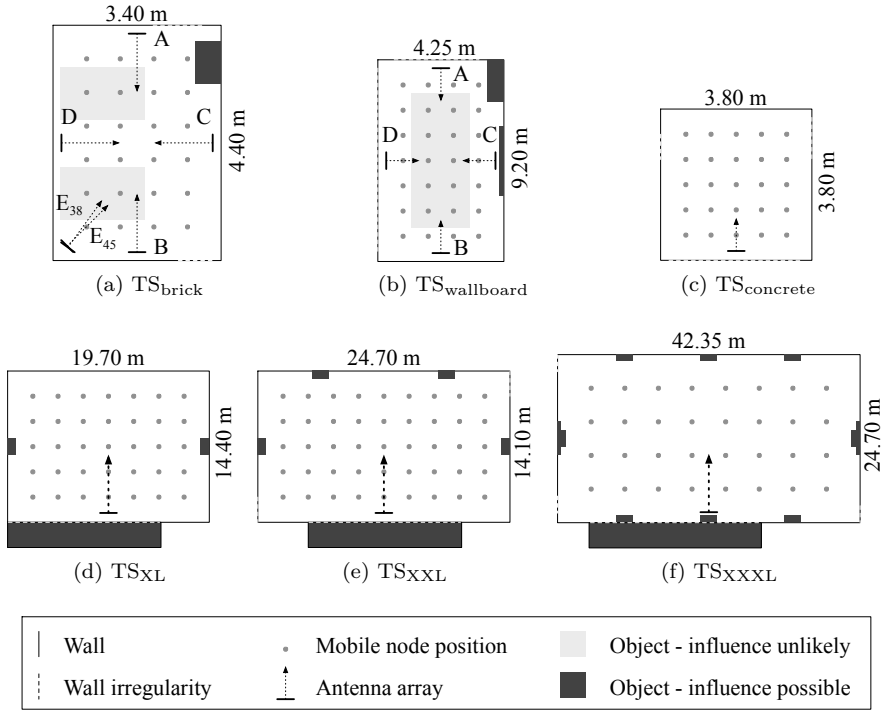

(a) TS_{brick} (b) $TS_{wallboard}$ (c) $TS_{concrete}$

(d) TS_{XL} (e) TS_{XXL} (f) TS_{XXXL}

Figure 5.1: Overview of the test environments

TS_{XL}: The smallest sports hall contains a 7x5 measurement grid and a 40x30 reference grid.

TS_{XXL}: A 9x5 measurement grid is used in this setup, with a reference grid of 50x30.

TS_{XXXL}: The measurement grid contains 8x4 positions and 84x50 reference grid points were simulated.

In all setups, measurements are performed at 2.47 GHz and 5.1 GHz with a 10-element $\lambda/2$ array configuration. Furthermore, for each position of the mobile node, a LOS and NLOS measurement is performed. In NLOS conditions, the LOS signal is blocked with Eccosorb VHP-8 absorbers [Eme10], attenuating the LOS component with at least 20 dB to 25 dB in the 2 GHz to 5 GHz band. In the small test setups, a single 0.6 m by 0.6 m absorber tile was used, while the larger rooms admitted a 1.2 m by 1.2 m absorber. The absorbing tiles are always placed between the transmitting and receiving antenna, blocking a 20° to 45° field of the omnidirectional mobile transmitter.

Literature research generally focuses on static NLOS situations [KWC13, TGdAG09, HPT+16], with experiments behind corners in complex indoor environments. Because these infrastructures are static, the NLOS channel characteristics can be fully known and exploited. In contrast to this, the new approach in this research emulates a dynamic situation where LOS conditions can turn to NLOS. This mimics real-world situations where moving people or furniture (temporarily) obstruct LOS connections. These environmental changes are unknown to the positioning system, so all localization tests are performed with the same reference data set $\mathcal{T}$, assuming LOS conditions. This approach is reproducible and enables a straight-forward comparison between LOS and NLOS results.

5.2 Selection of the Best Performing Localization Algorithm

Chapter 3 proposed multiple configurations for the localization algorithm. The presented method relies on a matching algorithm to rate the resemblance between a measurement vector $\boldsymbol{m}$ and a set of reference vectors $\boldsymbol{f}_i$. Measurement data is processed according to the MUSIC, ESPRIT and MVDR algorithms. This results in angular information in the form of a discrete or continuous angular PDF. For the MVDR based PDF, deconvolutions are performed in an effort to enhance the contrast of MVDR spatial spectra. For the sake of comparison with 'classical' AoA systems, an option was included that only takes the discrete direction of the strongest signal into account, assuming this to be the LOS signal. This brings the total amount of measurement representations to 11. For the reference dataset, again multiple representation methods are evaluated. First, the discrete outputs of a ray tracer are considered. These results are then circularly convolved with a Hanning window in order to resemble a spatial spectrum. Another method involves the MVDR algorithm to transform the discrete ray tracing data into a spatial spectrum. This spectrum can also be deconvolved in order to enhance contrast. A last option includes again a 'classical' approach, taking only the LOS direction into account. This brings the total number of representations for reference data $P_r(\theta)$ to five. Another variable in the localization algorithm is the amount of spatial smoothing operations in measurement and reference vectors. For a 10-element array, zero to eight spatial smoothings can be applied, representing nine extra options. With measurement and reference data available, the closest match should result in the location of interest. Two algorithms have been proposed to rate the resemblance between measurement and reference data. One option calculates the Pearson correlation coefficients $r_{\text{corr}}(i)$ between $\boldsymbol{m}$ and $\boldsymbol{f}_i$ for $\theta \in \{-90°, \ldots, 90°\}$.

Another method calculates the dot product of both functions, as explained in Section 3.5. Making all possible combinations of measurement data, reference data, spatial smoothings and matching algorithms, results in a total of 666 variants of the localization algorithm. In order to find the best performing configuration, a step by step approach is applied. First, the best of both matching algorithms is selected, followed by the best reference set, then the best measurement representation and finally the ideal amount of spatial smoothing. This method of stepwise elimination provides a clear insight in all factors of the localization algorithm. However, this elimination process also implies that whole groups of algorithms are left unstudied in the end. For example, choosing for the correlation based matching algorithm in the first step eliminates 333 variants of the algorithm. Therefore the configuration process concludes with a brute force comparison of all 666 variants to verify the end result.

For the evaluation of the algorithms, measurements from the three sports halls are considered: TS_{XL}, TS_{XXL} and TS_{XXXL}. This guarantees a data set of 122 LOS and NLOS measurement points, obtained in three similar real-world rectangular environments. Measurements are generally performed in the far field and LOS connections are easily interrupted with anechoic tiles, to facilitate the testing of NLOS performance. The evaluations rely on the mean, P50 and P95 values of normalized localization errors and surface intervals, presented in tables. This approach was preferred over graphical representations, given the vast amount of data.

5.2.1 Matching Algorithm

The evaluation of matching algorithms is performed separately for LOS and NLOS situations. All possible variants are considered for reference data, measurement data and spatial smoothing. As a result, two groups of 333 algorithms exist with only one distinction: one group encloses all localization algorithms based on Pearson correlation coefficients, while the other group uses the dot products. Considering the three test setups, each group contains $333 \times 122 = 40626$ localizations in LOS and NLOS conditions, from which mean, P50 and P95 values of normalized localization errors and surface intervals are calculated. These parameters are summarized in Table 5.1 and should only be used for mutual comparison. The absolute values do not represent the best achievable localization accuracy, since poorly performing algorithms are still included. Each step in the selection process should improve localization accuracy.

Table 5.1 indicates no clear winner when looking at the surface intervals in NLOS conditions. However, the superiority of the correlation based approach

Table 5.1: Comparison between correlation based and dot product based matching algorithms

		normalized error			surface interval		
		mean	P50	P95	mean	P50	P95
LOS	dot product	0.285	0.293	0.475	0.188	0.073	0.771
	correlation	0.231	0.212	0.485	0.186	0.068	0.790
NLOS	dot product	0.290	0.300	0.478	0.267	0.165	0.829
	correlation	0.251	0.238	0.506	0.267	0.169	0.837

becomes clear with the vastly improved mean and median values of localization errors in both LOS and NLOS conditions. A remarkable effect is that outliers are marginally larger for the correlation based approach, which is indicated by the P95 values. However this does not appear to significantly influence total system performance, as mean values follow the trend of median values. Following these findings, the correlation based approach was selected for further evaluations, eliminating all 333 dot product based algorithms.

5.2.2 Reference Data

For the next evaluation step, the same LOS and NLOS measurement data is used from TS_{XL}, TS_{XXL} and TS_{XXXL}. All correlation based algorithms are now divided according to the used reference data sets. Discrete ray tracing data is compared to a circular convolved version, MVDR spatial spectra and deconvolved MVDR spatial spectra. Table 5.2 demonstrates the poor performance of simulated MVDR spatial spectra as reference data in both LOS and NLOS conditions. Deconvolving the MVDR spatial spectra results in a slight improvement of localization errors, but on the other hand it also increases the surface interval. Overall, the use of simulated spatial spectra can be considered as a major step backwards in terms of localization performance, compared to ray tracing data. This can be explained by the loss of information that occurs in the process of simulating spatial spectra. Ray tracing data holds a pile of spatial information, which is transferred into simulated signals while adding noise. These signals are consequently processed in a simulated antenna array with simulated antennas. The simulated outputs of this array are then processed by AoA algorithms that inherently underperform in multipath environments because signals are correlated. The measurement results in Table 5.2 indicate that ray tracing data can be used without this lossy simulation chain. In both LOS and NLOS conditions, an artificial spatial spectrum based on the convolution of discrete ray tracing data with a Hanning window yields lower localization errors and better surface intervals than discrete ray tracing data.

Given these superior results, the circularly convolved ray tracing outputs are selected as a reference for further evaluations.

Table 5.2: Comparison of reference data sets

		normalized error			surface interval		
		mean	P50	P95	mean	P50	P95
LOS	raytrace discrete	0.219	0.199	0.458	0.094	0.049	**0.363**
	raytrace conv.	**0.184**	**0.153**	**0.434**	**0.085**	**0.038**	0.364
	MVDR	0.303	0.293	0.592	0.393	0.340	0.930
	MVDR deconv.	0.299	0.293	0.581	0.398	0.352	0.933
NLOS	raytrace discrete	0.246	0.226	0.504	0.194	0.118	**0.635**
	raytrace conv.	**0.207**	**0.190**	**0.433**	**0.188**	**0.107**	0.647
	MVDR	0.312	0.303	0.611	0.423	0.382	0.930
	MVDR deconv.	0.307	0.302	0.593	0.430	0.398	0.928

5.2.3 Measurement Data

With the selected matching algorithm (correlation based) and reference data (artificial spatial spectra, created with a circular convolution of discrete ray traced data with a Hanning window), the next step in the selection process is the evaluation of measurement vectors. Eleven variations of processing techniques have been investigated, with their respective results for the TS_{XL}, TS_{XXL} and TS_{XXXL} setups listed in Table 5.3. One of these options is the LOS benchmark, taking only a LOS reference into account, together with the strongest measured AoA in analogy to classical AoA localization systems. In this case, no localization errors are calculated, as a single antenna array cannot determine positions based on LOS connections alone. The surface interval however, is a valid means for comparison between all configurations.

The first and most important observation is that an unprocessed MVDR spatial spectrum results in the smallest localization errors and surface intervals in all circumstances. Performing a deconvolution of the MVDR spectrum results in marginally worse results and does not deliver the intended increased accuracy. Working with only the discrete peak values of the spatial spectrum means a further reduction of localization accuracy, most prominently indicated by the increased P95 surface intervals. Performing convolutions of these discrete values can slightly improve the results again. However, one can conclude that all post processing attempts to artificially improve MVDR spatial spectra can be considered as disadvantageous. This can be explained by the information loss inherent to these techniques.

Table 5.3: Comparison of measurement data processing

		normalized error			surface interval		
		mean	P50	P95	mean	P50	P95
LOS	**MVDR**	0.133	0.099	0.360	0.049	0.028	0.168
	- deconv	0.139	0.102	0.374	0.052	0.029	0.184
	- peaks	0.194	0.178	0.434	0.079	0.034	0.340
	- deconv peaks	0.194	0.170	0.439	0.088	0.037	0.385
	- peaks conv.	0.204	0.197	0.442	0.074	0.035	0.299
	- deconv peaks conv	0.193	0.178	0.439	0.075	0.033	0.316
	MUSIC peaks	0.191	0.167	0.423	0.107	0.045	0.486
	MUSIC peaks conv.	0.201	0.181	0.444	0.102	0.048	0.414
	ESPRIT peaks	0.192	0.168	0.425	0.115	0.045	0.500
	ESPRIT peaks conv.	0.202	0.179	0.444	0.111	0.049	0.488
	LOS benchmark	–	–	–	0.079	0.031	0.418
NLOS	**MVDR**	0.166	0.135	0.397	0.139	0.078	0.460
	- deconv	0.171	0.137	0.407	0.145	0.080	0.472
	- peaks	0.222	0.217	0.444	0.194	0.103	0.654
	- deconv peaks	0.212	0.206	0.427	0.205	0.121	0.680
	- peaks conv	0.233	0.233	0.451	0.182	0.100	0.618
	- deconv peaks conv	0.210	0.207	0.422	0.187	0.107	0.633
	MUSIC peaks	0.213	0.199	0.439	0.215	0.125	0.713
	MUSIC peaks conv.	0.219	0.208	0.440	0.199	0.118	0.683
	ESPRIT peaks	0.211	0.193	0.429	0.214	0.123	0.702
	ESPRIT peaks conv.	0.215	0.201	0.439	0.201	0.119	0.698
	LOS benchmark	–	–	–	0.210	0.105	0.718

MUSIC and ESPRIT based localization errors can be considered equal to each other, while the surface intervals indicate a slight advantage for MUSIC. In LOS conditions, the performance of these two algorithms in a multipath assisted approach lists worse than the LOS benchmark, which is a valid reason for abandonment in further tests.

As a conclusion, the MVDR spatial spectra without post processing are selected for the representation of measured AoA data in the localization algorithm. This has shown to exhibit supreme performance over all other options in both LOS and NLOS conditions, including the LOS benchmark.

5.2.4 Spatial Smoothing

The evaluation of matching algorithms, reference vectors and measurement vectors was performed for all possible spatial smoothings ($K_{\mathrm{ss}} \in [0, \ldots, 8]$). Therefore, the last step in the selection process requires the investigation of the optimal amount of spatial smoothing. The previously investigated variables of the localization algorithm are independent of the number of array elements. However, the amount of spatial smoothing operations is directly linked to the number of antennas, as explained in Section 2.4.4. As a consequence, this step should be seen as a specific optimization for 10-elements antenna arrays. Table 5.4 displays localization errors and surface intervals for all spatial smoothing options in a 10-elements array. For LOS benchmarks the best mean, P50 and P95 values over all possible spatial smoothings are listed. These best achievable LOS benchmark results offer an ideal means for evaluating the accuracy of the selected localization algorithm in comparison to a classical AoA approach.

Table 5.4: Comparison of spatial smoothings for a 10-element array

		normalized error			surface interval		
		mean	P50	P95	mean	P50	P95
LOS	$K_{\mathrm{ss}} = 0$	0.158	0.123	0.402	0.051	0.024	0.159
	$K_{\mathrm{ss}} = 1$	0.131	0.084	0.433	0.042	0.023	0.150
	$K_{\mathrm{ss}} = 2$	0.179	0.139	0.454	0.078	0.051	0.266
	$K_{\mathrm{ss}} = 3$	0.119	0.080	0.348	0.041	0.025	0.132
	$K_{\mathrm{ss}} = 4$	0.110	**0.073**	0.353	**0.037**	**0.021**	**0.104**
	$K_{\mathrm{ss}} = 5$	0.109	0.077	0.317	0.039	0.024	0.123
	$K_{\mathrm{ss}} = 6$	**0.108**	0.092	**0.270**	0.044	0.028	0.128
	$K_{\mathrm{ss}} = 7$	0.121	0.100	0.275	0.051	0.036	0.181
	$K_{\mathrm{ss}} = 8$	0.164	0.152	0.359	0.059	0.033	0.256
	Best LOS bench.	–	–	–	0.048	0.026	0.125
NLOS	$K_{\mathrm{ss}} = 0$	0.199	0.168	0.462	0.194	0.085	0.768
	$K_{\mathrm{ss}} = 1$	0.188	0.146	0.421	0.153	0.080	0.687
	$K_{\mathrm{ss}} = 2$	0.214	0.201	0.475	0.177	0.105	0.605
	$K_{\mathrm{ss}} = 3$	0.164	0.112	0.440	0.136	0.068	0.524
	$K_{\mathrm{ss}} = 4$	0.142	**0.108**	0.348	0.111	0.066	**0.351**
	$K_{\mathrm{ss}} = 5$	**0.138**	0.114	0.342	**0.106**	**0.062**	0.372
	$K_{\mathrm{ss}} = 6$	0.139	0.116	0.336	0.114	0.073	0.381
	$K_{\mathrm{ss}} = 7$	0.141	0.130	**0.285**	0.126	0.079	0.386
	$K_{\mathrm{ss}} = 8$	0.168	0.158	0.344	0.138	0.082	0.403
	Best LOS bench.	–	–	–	0.164	0.087	0.684

The lowest mean, P50 and P95 localization errors and surface intervals are highlighted in Table 5.4, indicating superior performance for four up to seven spatial smoothings, depending on the investigated parameter and test conditions. When the mean values are observed, the best amount of spatial smoothing averages at five. When the best amount of spatial smoothing is averaged for median and P95 parameters, a value of 4.75 is obtained. Therefore, the amount of spatial smoothing that is selected for all further 10-element array tests, is fixed at five. This value of K_{ss} guarantees better results than the best LOS benchmarks in all circumstances.

Since Table 5.4 is used for the last step in the selection process, all listed values indicate the absolute performance of the configured localization system. Five spatial smoothings result in a mean surface interval of 3.9% in LOS conditions, a clear improvement over the best LOS benchmark which was already as low as 4.8%. More significant results are obtained in NLOS situations, where the configured localization algorithm results in a mean surface interval of 10.6%. This result is a 35% improvement over the best possible mean surface interval of 16.4% for the best LOS benchmark. The NLOS P95 surface intervals exhibit an even stronger decrease, almost halving from 68.4% to 37.2%. This major improvement of P95 values indicates the increased reliability that can be achieved with the proposed localization algorithms.

5.2.5 Conclusions Concerning the Configuration of the Localization Algorithms

The step by step evaluation of all variables of the localization algorithm has led to an optimal solution. The result is based on 122 measurement positions in the $\mathrm{TS_{XL}}$, $\mathrm{TS_{XXL}}$ and $\mathrm{TS_{XXXL}}$ setups, providing a large consistent dataset. The smaller test setups were not considered for the optimization process, but extensive evaluations in these environments follow in Section 5.6.2. The final result of the optimization is based on a correlation based matching algorithm. The reference data is represented as an artificial spatial spectrum, which is created by the convolution of discrete ray traced data and a Hanning window. The measurements are processed with the MVDR algorithm, which results in a spatial spectrum. For measurement pre-processing, five spatial smoothings were applied, the optimal amount for a 10-element array.

The evaluation of all parameters of the localization system was performed by a step by step elimination process. All data is considered for the calculation of localization errors and surface intervals, but due to the elimination process, large groups are discarded at once (for example: all dot product algorithms). This means that not each configuration is evaluated separately. Therefore, a final

brute force evaluation was performed, ranking all 666 variants of the localization algorithm in LOS and NLOS conditions according to their mean surface interval. The five best results are listed in Table 5.5, confirming the previous findings of the step by step optimization. Furthermore, the best LOS benchmark result is listed in Table 5.5, indicating that the classical approach performs very well in LOS conditions, achieving the 19th position of 666 configurations. This finding confirms previous research, however the inclusion of multipath information demonstrates a further accuracy enhancement and allows single-anchor localization, which is impossible with the benchmark approach. In NLOS conditions, the superior performance of the proposed algorithms becomes much clearer. The best LOS benchmark ranks at position 145 of 666, proving that the new algorithms with simulated spatial information offer increased robustness of the localization system in realistic environments with NLOS situations.

Table 5.5: Listing of the five best configurations of the localization algorithm together with the highest ranked LOS benchmark. Ranking according to the mean *SI* values in LOS and NLOS situations

	#	matching	reference	measurement	K_{ss}	mean *SI*
LOS	1	correlation	raytrace conv.	MVDR	4	0.0368
	2	correlation	raytrace conv.	MVDR deconv.	4	0.0381
	3	correlation	raytrace conv.	MVDR	5	0.0388
	4	correlation	raytrace conv.	MVDR deconv.	5	0.0388
	5	correlation	raytrace conv.	MVDR	3	0.0407
	19	correlation	LOS conv.	MVDR LOS	5	0.0482
NLOS	1	correlation	raytrace conv.	MVDR	5	0.1062
	2	correlation	raytrace conv.	MVDR deconv.	5	0.1100
	3	correlation	raytrace conv.	MVDR	4	0.1112
	4	correlation	raytrace conv.	MVDR deconv.	4	0.1131
	5	correlation	raytrace conv.	MVDR	6	0.1137
	145	correlation	LOS conv.	MVDR LOS	6	0.1638

The superior performance of the proposed algorithms is visually represented in Figure 5.2, depicting the CDF of surface intervals for the best algorithm and the best LOS benchmark in LOS and NLOS conditions. In LOS situations, the proposed algorithms mainly reduce the largest surface intervals in comparison to the LOS benchmark. For NLOS situations, an overall performance improvement can be noticed.

The localization approach can also be evaluated in terms of computational complexity. As reported in Section 3.2.3, the Matlab® positioning framework runs on a 2.3 GHz Intel® Core i5 2415M mobile CPU with 8 GB of RAM. The computational load depends on the room geometry, therefore an example

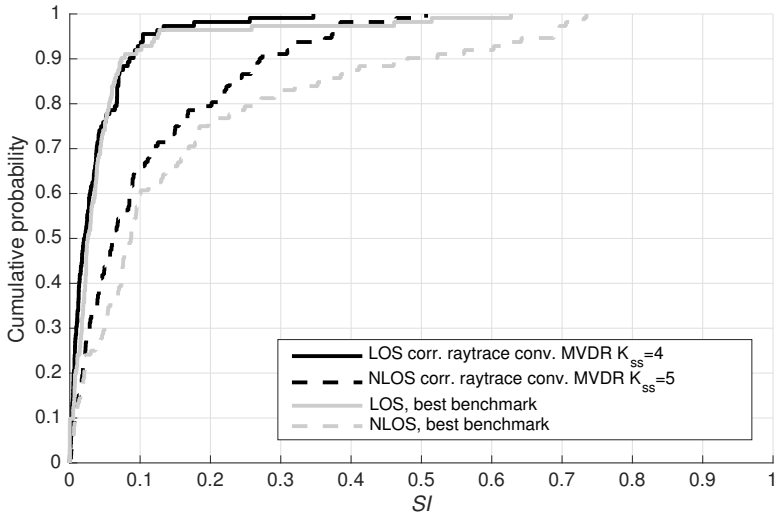

Figure 5.2: Cumulative probability of surface intervals for the best performing configuration of the localization algorithm and the best performing benchmark algorithm in LOS and NLOS conditions

configuration was selected for the following results: $\mathrm{TS}_{\mathrm{XXL}}$. The multipath simulation for a single fingerprint takes 0.770 s, so the offline generation of training data $\mathcal{T}$ for 1500 reference points takes less than 20 minutes. In the online phase, measurements are processed and matched to the training data, which takes only 0.005 s to 0.010 s. It is clear that the main computational burden is shifted to the offline phase, resulting in a swift localization process that could even be implemented in an embedded system. The limited processing times are the result of a thorough parallelization, however further improvements can be made by transforming the Matlab® testing framework into a dedicated solution.

5.3 Evaluation of Ray Tracing Simulations

The localization algorithm evaluates the match between a measurement and the reference dataset. The latter results from ray tracing simulations in the known infrastructure. Section 5.2 already illustrated that this multipath approach outperforms the LOS benchmark. This section specifically investigates the performance of the ray tracing method. First, simulated reference data is

compared to a classical fingerprinting approach with measured fingerprints. Next, the importance of simulating the correct wall characteristics (ε_r) is studied.

5.3.1 Reference Data: Ray Tracing vs. Measuring

In order to assess the value of the implemented multipath simulator, localization tests are performed with a measured reference set (cfr. fingerprinting, as presented in Section 4.5.2), a ray traced reference set, and a LOS benchmark set. The simulated reference data is considered valuable when its resulting localization accuracy approaches the accuracy for measured reference data. Poor performance is presented when the accuracy approximates the LOS benchmark performance.

The evaluations are performed in the $\mathrm{TS}_{\mathrm{brick,A}}$ test setup with a 4x6 measurement grid. Normally, the reference set in this setup is 30x40. This fine grid presents no problem for computer simulations and assures a high localization precision, however it would be practically unfeasible for building a measured reference grid of this size. Therefore, the reference grid is exceptionally set to a coarse 4x6 grid for this test, equally to the measurement grid. The measured, ray traced an LOS benchmark reference sets are all built along this 4x6 grid in order to maintain comparability. The measured reference grid consists of measured MVDR spatial spectra with $K_{ss} = 5$. Ray traced reference data contains the circularly convolved discrete multipath components as proposed in Section 5.2.2, and the benchmark only represents the LOS direction.

Table 5.6: Comparison of reference datasets in $\mathrm{TS}_{\mathrm{brick,A}}$, $K_{SS} = 5$

		normalized error			surface interval		
	Reference	mean	P50	P95	mean	P50	P95
LOS	Measured	0.120	0.113	0.320	0.083	0.042	0.300
LOS	Ray traced	0.102	0.113	0.320	0.096	0.042	0.483
LOS	LOS benchmark	–	–	–	0.135	0.042	0.708
NLOS	Measured	0.167	0.113	0.497	0.149	0.063	0.521
NLOS	Ray traced	0.119	0.113	0.361	0.175	0.042	0.729
NLOS	LOS benchmark	–	–	–	0.252	0.146	0.763

Table 5.6 lists the localization results for the three considered test situations in LOS and NLOS conditions. The localization errors indicate that simulated reference data yields similar results to the measured reference set in LOS conditions. In NLOS conditions, the ray traced data even results in the lowest localization errors, which can be attributed to the simulation of only specular

reflections, as explained in Section 3.2.3. The surface intervals also demonstrate the favorable results for ray traced reference data in LOS and NLOS conditions. P95 values are sligthly elevated, but the system clearly outperforms the LOS benchmark algorithms.

Overall, these results demonstrate the high value of ray traced reference datasets. Benchmark results are clearly exceeded, and the performance of measured datasets is approximated. All tests were performed with the same 4x6 measurement and reference grids. This means that only on-grid testing was performed. As demonstrated in Section 4.5.2, off-grid measurements result in a significant degradation of localization accuracy. However, this problem is prevented by the fine simulated reference grids in the proposed system.

5.3.2 Simulated Wall Materials

For the calculations of signal reflections, the permittivity of wall materials was studied in literature, as documented in Section 3.2.4. This section investigates the sensitivity of localization accuracy to variations in the simulated permittivity of wall materials. More specifically, three test setups are considered: $\text{TS}_{\text{wallboard}}$, TS_{brick} and $\text{TS}_{\text{concrete}}$. Every room is simulated three times: the wall permittivity is varied from wallboard ($\varepsilon_{r,wallboard} = 2.4$) to brick ($\varepsilon_{r,brick} = 4.0$) and concrete ($\varepsilon_{r,concrete} = 8.0$). These tests are all based on the same measurement data, with only reference data varying. The results are presented in Table 5.7, listing the mean surface intervals of the optimized localization algorithm in LOS and NLOS situations.

Table 5.7: Mean surface intervals as a function of the simulated wall materials in three different setups.

			Simulated material		
			wallboard	brick	concrete
Setup	LOS	$\text{TS}_{\text{wallboard}}$	**0.0701**	0.0704	0.0739
		TS_{brick}	0.0602	**0.0592**	0.0701
		$\text{TS}_{\text{concrete}}$	0.0380	0.0339	**0.0338**
	NLOS	$\text{TS}_{\text{wallboard}}$	0.1641	0.1616	**0.1586**
		TS_{brick}	0.1387	**0.1286**	0.1364
		$\text{TS}_{\text{concrete}}$	0.2588	0.2463	**0.2413**

The best localization performance can be achieved when the correct wall materials are simulated. Although this seems a logical result, it provides an indication of the correctness of the used wall permittivity and the implementation of the ray tracer. It also indicates that the over- or undervaluation of specular

reflections does not result in a better performance. One exception can be remarked in the NLOS wallboard setup, which performs better when concrete walls are simulated. A possible explanation for this phenomenon is that a simulation of wallboard walls results in very weak specular reflections. In NLOS environments, the localization algorithm heavily relies on these signal components, so overvaluing the specular reflections could result in better performance.

While the results in Table 5.7 generally indicate the best performance if the correct wall materials are simulated, it is also important to notice that the absolute deviation of the localization accuracy is very limited when the wrong material is simulated. In most of the cases, the mean surface interval changes less than 1%. This property is very beneficial for real-world environments, as building materials are often combined. A precisely modelled environment does not seem essential for obtaining good results. Section 5.2 demonstrated that the simulation of multipath components increases the accuracy of the localization system. This section indicates that the absolute signal strengths of all multipath components only have a limited influence on the system accuracy.

5.4 Evaluation of Array Hardware Parameters

Chapter 4 discussed multiple aspects of the antenna array design, but localization performance was not covered. This section investigates the influence of antenna coupling, the number of antennas and the number of array snapshots on the localization accuracy. Another important array parameter is the operation frequency. However, this is treated in the dedicated Section 5.7, discussing multiple aspects of 5 GHz operation.

5.4.1 Antenna Coupling

As explained in Section 4.4.4, the coupling between array elements has an adverse effect on AoA estimation accuracy. This logically affects the performance of the localization system, which is assessed in this paragraph. Figure 5.3 depicts an example of a measured indoor spatial spectrum with and without antenna coupling, as well as the corresponding artificial reference spectrum at the same position. The test was performed in LOS conditions in setup $\mathrm{TS_{XL}}$ at measurement position $(5, 3)$ and demonstrates the effect of antenna coupling. The spectrum without coupling shows clear resemblance to the simulated reference curve. When antenna coupling is taken into account, the most important peaks can still be recognized under similar angles. However,

the similarity to the reference spectrum is clearly reduced, as power levels are completely changed, indicating reflections that are stronger than the LOS peak. This is a trend that is seen over all measurements, confirming the results of Figure 4.13.

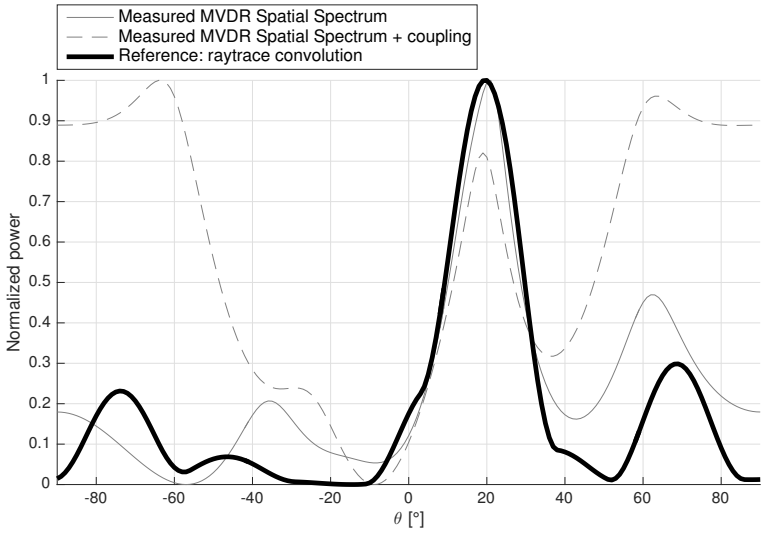

Figure 5.3: Example of the reference spectrum, measured spatial spectrum and measured spatial spectrum with antenna coupling in LOS conditions in setup $\mathrm{TS_{XL}}$, at position $(5, 3)$

In order to study the influence on the accuracy of the localization system, all $\mathrm{TS_{XL}}$, $\mathrm{TS_{XXL}}$ and $\mathrm{TS_{XXXL}}$ tests are performed with and without artificially adding coupling of the patch antennas. The resulting surface intervals and localization errors are listed for the optimized positioning algorithm (convolved ray tracing data, correlated with an MVDR based measurement vector) in Table 5.8.

The results without antenna coupling exhibit very low surface intervals and localization errors, considering the single anchor node setup. However, when antenna coupling is added, a clear deterioration of surface intervals and normalized localization errors can be observed in LOS and NLOS conditions. Surface intervals are more than doubled and localization errors also increase significantly. Interestingly, localization errors for LOS and NLOS configurations are similar when antenna coupling is included. This can be attributed to the strong negative effect on the LOS peak of the spatial spectrum, as demonstrated in Figure 5.3. Overall, the strong negative effect of antenna coupling follows

Table 5.8: Comparison of the accuracy of the optimized localization algorithm in a system with and without antenna coupling. LOS and NLOS tests in setup TS_{XL}, TS_{XXL} and TS_{XXXL}

		surface interval			normalized error		
		mean	P50	P95	mean	P50	P95
LOS	Without coupling	0.039	0.024	0.123	0.109	0.077	0.317
	With coupling	0.166	0.121	0.413	0.209	0.177	0.547
NLOS	Without coupling	0.106	0.062	0.372	0.138	0.114	0.342
	With coupling	0.252	0.178	0.732	0.188	0.173	0.401

the clear adverse effects on AoA accuracy that were reported in Section 4.4.4. This demonstrates that the measurement equipment with a flexible virtual antenna array is a valid setup for an unbiased investigation of multipath components. However, in real-world setups with non-synthetic antenna arrays, mutual coupling is clearly a design factor of major concern. As described in [LHL09], antenna coupling can be mitigated with compensation methods or even by dedicated antenna and array design. This falls out of the scope of this research and is considered future work. All further results in this book do not include antenna coupling because of its hardware dependency, as described in Section 4.4.4. Excluding this effect also guarantees a more justified comparison between results when hardware parameters change, for example at 2.47 GHz and 5.1 GHz.

5.4.2 Number of Array Elements

Most of the AoA evaluations are performed with a 10-elements array, which is the largest configuration that can be formed with the available setup at 2.47 GHz with $\lambda/2$ inter-element spacing. This section discusses the accuracy of the indoor localization system as a function of the number of array elements. Furthermore the relationship between the number of antennas, spatial smoothing and the localization accuracy is investigated. For these evaluations, the results of TS_{XL}, TS_{XXL} and TS_{XXXL} are merged, resulting in a data set of 122 positions to be localized. Evaluations are performed in LOS and NLOS conditions for both the benchmark algorithm and the optimal algorithm. All results are based on the same phase and amplitude measurements of a 10-element array, from which channels are eliminated to evaluate the performance with less antenna elements.

Figures 5.4a and 5.4b depict respectively the mean surface interval and mean normalized error as a function of the number of array elements. These results heavily depend on the applied amount of spatial smoothing. This parameter is

depicted in Figure 5.5. In Figures 5.4a and 5.4b only the best achievable results are presented. This means that for each point in these graphs, only the best result of all possible spatial smoothings is depicted.

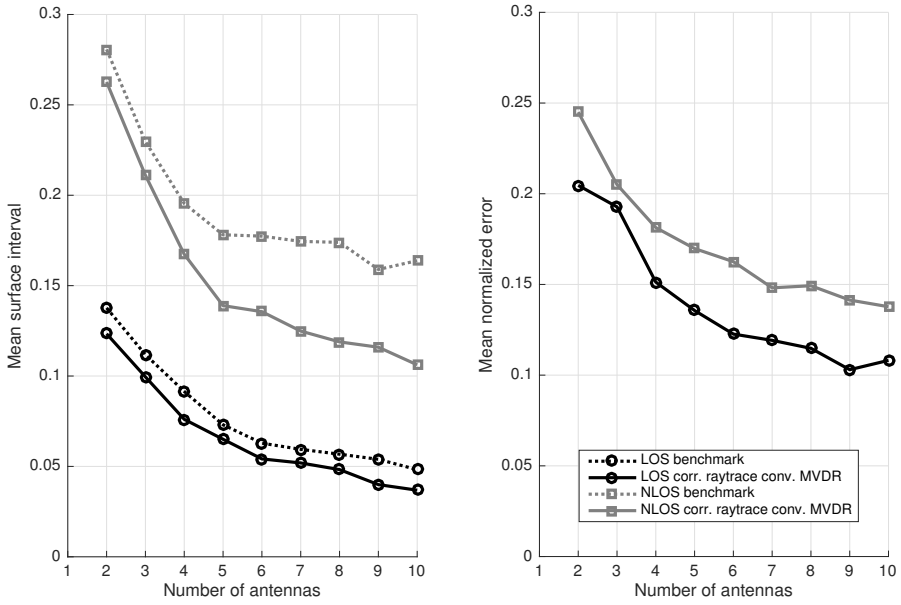

(a) (b)

Figure 5.4: Evaluation of the mean surface interval (a) and mean normalized errors (b) as a function of the number of array elements (M).

Figure 5.4a clearly illustrates how the proposed localization algorithm outperforms the standard benchmark algorithm in LOS and NLOS situations for any number of array elements. This effect is manifested most clearly in NLOS situations when the number of antennas increases, providing more multipath information. As soon as four antennas are used, the proposed algorithm performs equally or better than the benchmark algorithm that uses one more antenna in both NLOS and LOS situations. For localization systems with the benchmark approach and five or more antennas, this means that the array size can be cut without reducing the accuracy of the system, just by using the proposed localization algorithm. With five antennas, the proposed algorithm outperforms the benchmark algorithm in all NLOS configurations till 10 elements. Figure 5.4b confirms the previous conclusions. Logically, an increase in array size results

in a reduction of the localization errors. The graph also illustrates that LOS accuracies can be achieved in NLOS situations, if more antennas are added. This is also illustrated in Figure 5.4a, however this holds only for the proposed algorithm, which takes multipath components into account.

As already mentioned, the graphs in figures 5.4a and 5.4b only depict the best results of all possible spatial smoothings. Figure 5.5 indicates the optimal amount of spatial smoothing $K_{\mathrm{ss,optimal}}$ as a function of the number of antennas M. The optimization of spatial smoothing is a minimization of the mean surface intervals and the mean normalized localization errors in both LOS and NLOS situations. The discrete points can be approximated with a linear regression. The result of such a least-squares linear regression is expressed in Equation 5.1, taking all discrete points into account. Of course, only a discrete number of spatial smoothings can be performed, so if the equation is used for determining $K_{\mathrm{ss,optimal}}$ in a given setup, a rounded value should be used. Normally, the point $(2, 0)$ should be part of the curve, as spatial smoothing is impossible in 2-element arrays, following Equation 2.28. After rounding, the correct value is obtained. For $M = 10$, the results of Section 5.2.4 are confirmed.

$$K_{\mathrm{ss,optimal}}(M) = 0.600 \cdot M - 1.004 \tag{5.1}$$

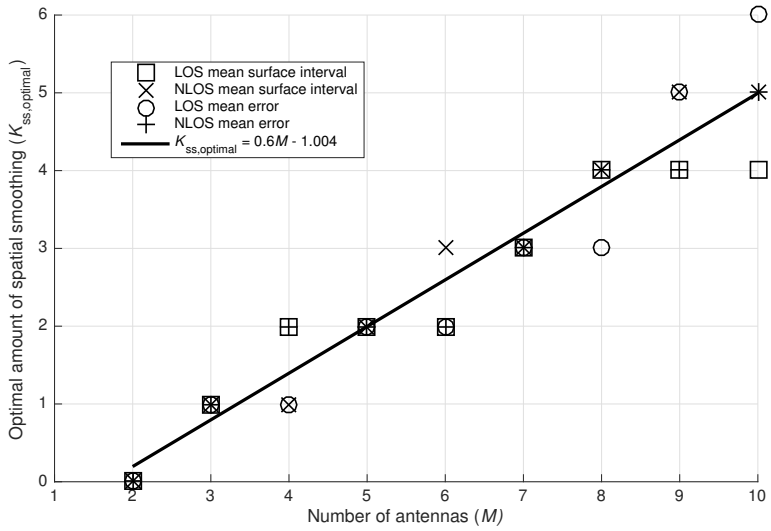

Figure 5.5: Optimal amount of spatial smoothing

5.4.3 Array Snapshots

Non-parametric methods for AoA estimation can be used to calculate a spatial periodogram, as expressed in Equation 2.16, in analogy to power spectral density estimators [MLVC09, SM05]. Such a spatial periodogram represents a large variance estimate of the spatial spectral density from the array output vector $r(t)$. In order to reduce the variance, N spatial periodograms can be averaged, resulting in a spatial spectrum $P(\theta)$ of N array snapshots 2.17, calculated with an N snapshots array correlation matrix $\tilde{\boldsymbol{R}}$. Logically, as more array snapshots are taken into account, spatial spectra should be more reliable and the accuracy of the localization system should increase. This section studies the mean surface interval as a function of the number of array snapshots N. Nine values were studied for N, ranging from 5 to 1201, which is the largest number of snapshots that can be acquired in one measurement with the used setup. For the evaluation, 1201 snapshots were measured, for lower values of N, data was simply omitted. Test setups $\mathrm{TS_{XL}}$, $\mathrm{TS_{XXL}}$ and $\mathrm{TS_{XXXL}}$ are considered, resulting in a dataset of 122 measurement locations.

Figure 5.6 presents the results of this evaluation in NLOS and LOS conditions for both the benchmark algorithm and the optimal algorithm. The graph reveals that the number of array snapshots hardly influences the accuracy of the tested localization system. Even for $N = 5$, excellent localization results can be achieved. Only the NLOS benchmark shows a small improvement at 64 snapshots. These results benefit the applicability of the system in real-world situations with a moving mobile node. Given the dynamic propagation conditions, fast sampling of a few snapshots is a requirement. A first explanation for these positive results lies in the high SNR that can be achieved with the designed virtual antenna array, by using a vector network analyzer, amplifiers and selecting a frequency at the boundaries of the 2.4 GHz ISM band (2.47 GHz).

A more in-depth explanation for the findings can be found in [VB95]. This paper discusses the performance of the MVDR estimator as a function of N and signal to noise ratio (SNR) for a 10-element $\lambda/2$ antenna array with two impinging signals. For the smallest number of array snapshots ($N = 20$) and the lowest SNR (10 dB), the reported standard deviation of AoA errors ($\sigma_{\epsilon_{\mathrm{AoA}}}$) is still smaller than 1°. As the number of samples increases to 1000, $\sigma_{\epsilon_{\mathrm{AoA}}}$ decreases further below 0.01° at 30 dB SNR. In some configurations (e.g., radar systems), this represents an important accuracy improvement. However in the considered localization system sub-degree AoA accuracy can be considered completely overdone. The designed system rather relies on the general resemblance of spatial spectra with some multipath components in the $-90° \ldots 90°$ range, without requiring exact AoA measurements.

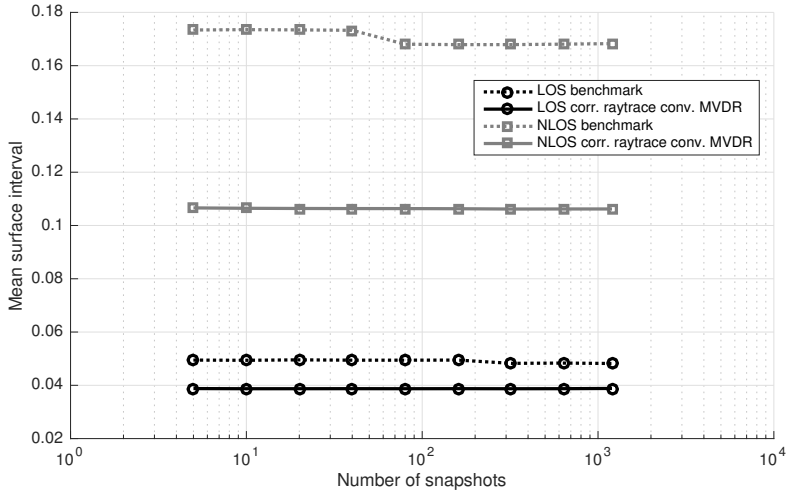

Figure 5.6: Mean surface intervals as a function of the number of array snapshots

5.5 Organization of Arrays

An important step in the configuration of the localization system consists of the placement of anchor nodes. As a precondition, only lateral positions are evaluated, i.e. close to the walls, in order to limit the impact of the system on the interior design. First, Section 5.5.1 evaluates multiple positions for an individual antenna array. Taking these results into account, the combination of antenna arrays is discussed in Section 5.5.2.

5.5.1 Single Array

This paragraph evaluates the position of an individual antenna array in a rectangular room. For this evaluation, test setup $\mathrm{TS}_{\mathrm{brick}}$ was considered with the array positioned in the middle of the shortest wall (positions A and B), in the middle of the longer wall (positions C and D), and in a corner of the room under 45° (position E_{45}) or along the room diagonal (position E_{38}). In each position, the surface intervals are evaluated for the benchmark and optimized algorithm in both LOS and NLOS conditions. The results are listed in Table 5.9.

The middle of a shorter wall appears to be the best location to place an antenna array. LOS and NLOS measurements clearly lead to this conclusion with the best

Table 5.9: Evaluation of array positions in test setup TS_{brick}

			surface interval			normalized errors		
	setup	algorithm	mean	P50	P95	mean	P50	P95
LOS	**short wall**	bench.	0.049	0.031	0.163	–	–	–
		optimal	**0.042**	**0.025**	0.148	**0.135**	**0.092**	**0.357**
	long wall	bench.	0.086	0.044	0.430	–	–	–
		optimal	0.076	0.047	0.234	0.177	0.162	0.394
	corner 45°	bench.	0.049	0.037	**0.132**	–	–	–
		optimal	0.101	0.078	0.345	0.183	0.154	0.513
	corner 38°	bench.	0.084	0.042	0.410	–	–	–
		optimal	0.101	0.058	0.496	0.220	0.180	0.604
NLOS	**short wall**	bench.	0.168	0.110	0.531	–	–	–
		optimal	**0.109**	**0.037**	0.547	**0.145**	**0.106**	0.405
	long wall	bench.	0.181	0.125	0.532	–	–	–
		optimal	0.148	0.111	**0.399**	0.172	0.148	**0.387**
	corner 45°	bench.	0.199	0.085	0.797	–	–	–
		optimal	0.151	0.108	0.471	0.178	0.121	0.447
	corner 38°	bench.	0.179	0.119	0.514	–	–	–
		optimal	0.192	0.113	0.564	0.179	0.128	0.452

mean and P50 surface intervals and localization errors over all configurations. Placing the antenna array against a longer wall results in a significant increase of surface intervals and localization errors. For this effect, multiple explanations can be given. First of all, the accuracy of AoA estimation decreases towards the sides of the field of view, i.e. close to $-90°$ and $90°$, as presented in Section 4.4.3. Placing the antenna array against a longer wall will result in more signals that impinge at larger angles. Figures 5.7b and 5.7d illustrate the intuitive explanation that moving the array from the shorter to the longer wall, will result in a shift of LOS signals towards the sides of the field of view. For uniformly distributed measurement positions (i.e. the measurement grid), this means a larger density of impinging LOS signals at the sides of the field of view. Figures 5.7a and 5.7c illustrate a similar finding for first order reflections. One can see that these reflections are generally pushed to the end of the field of view as the array is placed against the longer wall. A last interesting remark is that the angles of the first order reflections show a larger variation ($\Delta\theta$) when the array is placed against the shorter wall. These first order reflections contain valuable information on the location of the mobile node. More variation in their angles ($\Delta\theta$) results in a more accurate estimation of their location, due to the limited resolution of the antenna array.

Given the inferior results at the sides of the field of view, one could decide

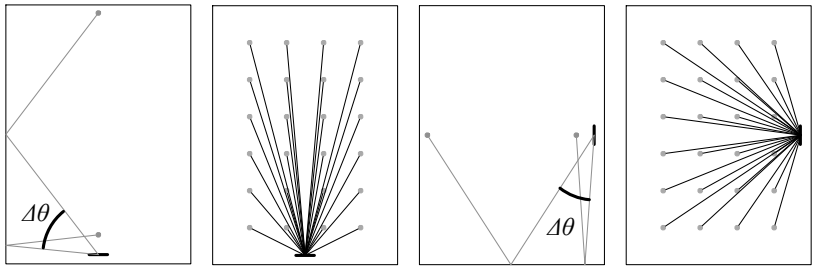

Figure 5.7: AoA for an array placed against the shorter wall (a,b) or the longer wall (c,d)

to restrict the angles of impingement. This could be achieved by placing the antenna array in a corner of the room, preventing angles from impinging at $\pm 90°$. In this configuration, two logical choices can be made. One option places the array under an angle of 45°, limiting the incident angles symmetrically around 0°, from $-45°$ to 45°. Another position is along the room diagonal (38° in the considered setup), splitting the room in two equally sized parts. The results for these configurations are listed in Table 5.9. A first significant observation is that benchmark algorithms clearly outperform the optimized algorithms in LOS situations. In NLOS conditions this effect is less conclusive. These unexpected results could be explained because all multipath components are concentrated in a limited part of the field of view, making it more difficult to distinguish individual signal directions. Therefore it seems to be more effective to focus solely on the strongest signal component, particularly in LOS situations. Increasing the inter-element distance of the antenna array to λ would increase its resolution and enable a better distinction of multipath components. However, such a setup would be very large (1.22 m for a 10-elements ULA at 2.47 GHz) and inappropriate for use in a room corner. Also, the reduced performance that previously occurred around $\pm 90°$ will now occur around $\pm 45°$. An ideal experimental setup for corner based arrays would involve a dedicated directional array element design, which would be beneficial from an antenna coupling point of view. When comparing the arrays under 45° and 38°, slightly better results can be noticed for the 45° configurations. However, the most important conclusion of this evaluation is that the optimal array position is the middle of the shorter wall. Placing the arrays in a corner of the room results in a serious increase of surface intervals and should be avoided.

5.5.2 Dual Array Combinations

The previous paragraph focussed on the best location of an individual antenna array in a rectangular room. However, multiple antenna arrays can be combined in order to maximize localization performance and robustness. For these combinations, one cannot simply assume that the best overall performance will be achieved by combining the best individual results. This paragraph investigates the combination of two antenna arrays in a rectangular room.

In a classical AoA approach with two antenna arrays, a location is determined by the intersection of two LOS directions. This means that every position on the line between the two arrays is theoretically unresolvable because there is no single point of intersection. In order to enhance performance, the line between the two arrays should be as short as possible. The ultimate solution from this point of view would consist of placing the arrays very close to each other. However, as arrays move closer to each other, the two intersecting LOS lines become one line without any intersection points. It is clear that this problem will require a trade-off. This design choice is also influenced by the individual performances, as explained in the previous paragraph. Placing the arrays against the longer walls of a rectangular room might be advantageous from a combinational point of view, but the individual array information will be less accurate. It is clear that an experimental approach is the most reliable method for obtaining clear insights in the positions of two antenna arrays in a rectangular room.

Table 5.10 lists the performance of different array combinations for dual LOS and dual NLOS connections in the TS_{brick} test setup. The benchmark and optimal (correlation of convolved ray tracing data and measured MVDR spatial spectrum) algorithms are investigated. For the array combinations, three types are considered: orthogonal arrays ($TS_{brick,AC,AD,BC,BD}$), facing arrays located in the middle of the shorter wall ($TS_{brick,AB}$) and facing arrays in the middle of the longer wall ($TS_{brick,CD}$). Array positions in a corner of the room were omitted in these evaluations, given the unfavorable results that were reported in paragraph 5.5.1.

In LOS conditions, no best array positions or localization algorithm can be isolated: orthogonal arrays and facing arrays against the shorter wall both generate good results. Notably, the benchmark algorithms perform very well, a logical result as two LOS connections result in a clear point of intersection. NLOS tests give a better indication of the preferable setup. When looking at the normalized localization errors, a clear winner can be selected: the orthogonal arrays with the optimized algorithm. This configuration is selected for its low localization errors (mean NLOS localization error is 8.5% of the room diagonal)

Table 5.10: Combination of array positions in test setup TS_{brick}

			surface interval			normalized error		
	setup	algorithm	mean	P50	P95	mean	P50	P95
dual LOS	**Orthogonal**	bench.	0.033	0.007	0.222	0.051	**0.033**	0.194
		optimal	**0.018**	0.009	0.071	0.048	0.037	0.122
	Facing, short wall	bench.	**0.018**	**0.006**	0.078	**0.045**	0.036	**0.099**
		optimal	0.019	0.009	**0.059**	0.052	0.047	0.131
	Facing, long wall	bench.	0.056	0.015	0.241	0.055	0.033	0.198
		optimal	0.027	0.014	0.107	0.053	0.042	0.139
dual NLOS	**Orthogonal**	bench.	0.105	0.055	0.350	0.102	0.074	0.281
		optimal	0.061	0.026	0.203	**0.085**	**0.059**	**0.227**
	Facing, short wall	bench.	0.112	0.075	0.369	0.158	0.098	0.424
		optimal	**0.056**	**0.022**	**0.196**	0.106	0.077	0.283
	Facing, long wall	bench.	0.131	0.089	0.440	0.127	0.113	0.280
		optimal	0.089	0.071	0.292	0.111	0.110	0.237

and particularly good surface intervals in LOS and NLOS conditions.

5.5.3 Antenna Distribution

The previous paragraph focused on increasing the localization accuracy by adding an extra 10-element antenna array, which is an effective yet costly operation. This paragraph investigates how the accuracy can be enhanced with restrictions on the cost of the system and complexity of hardware. More specifically, the best setup with one 10-element array (array against a shorter wall of the room), is compared to a setup with two 5-element ULAs, located on orthogonal walls. This solution requires the same amount of receiver channels, however increased performance could be achieved due to their spatial separation, similar to distributed antenna communication systems [CVC+16]. For the 5-element and 10-element arrays, respectively two and five spatial smoothings were applied, following the results of Section 5.4.2.

Table 5.11 presents the results of this experiment in the TS_{brick} setup. The results clearly indicate that two 5-element arrays offer a significantly higher localization accuracy over a single 10-element array. This effect is the strongest in LOS conditions, with halved localization errors and strongly decreased surface intervals. In (dual) NLOS conditions the same conclusions hold, yet less pronounced: localization errors are slightly improved but surface intervals remain inconclusive due to contradictory mean and median values.

Table 5.11: Comparison of one 10-element array with two 5-element arrays in test setup TS_{brick}

			surface interval			normalized error		
	setup	algorithm	mean	P50	P95	mean	P50	P95
LOS	1x10	benchmark	0.049	0.031	0.163	–	–	–
		optimal	0.042	0.025	0.148	0.135	0.092	0.357
	2x5	benchmark	0.040	0.010	0.220	0.075	0.043	0.289
		optimal	0.025	0.013	0.089	0.061	0.045	0.162
NLOS	1x10	benchmark	0.168	0.110	0.531	–	–	–
		optimal	0.110	0.037	0.547	0.145	0.106	0.405
	2x5	benchmark	0.125	0.067	0.432	0.116	0.086	0.269
		optimal	0.094	0.055	0.280	0.106	0.095	0.270

The results in Table 5.11 also confirm the value of multipath information, as a 10-element array clearly benefits from the optimized localization algorithm. This is most prominently illustrated by the NLOS surface intervals. In 5-element arrays the achievable improvement from multipath information is less explicit, as only two signal components can be distinguished with the given amount of spatial smoothings.

As a conclusion, it is fair to state that multiple small spatially distributed arrays offer a more robust solution than setups that rely on one large array. When a quick and less intrusive installation is desired, a system with a single large array can be applied in combination with the optimized localization algorithm.

5.5.4 Subarrays

All 2.4 GHz localization experiments in this research rely on the same 10-element $\lambda/2$ ULA. Given Equation 2.5, the calculated far field distance is 4.92 m. One of the boundary conditions for AoA estimation is far field operation, since the impinging wavefront is supposed to be planar. It is clear that this assumption is not always applicable in indoor environments, especially in small rooms. However, previous tests have proven that the setup can produce satisfying results. These results were generally achieved with five spatial smoothing operations, splitting the array into six 5-element subarrays and averaging their spatial covariance matrices as explained in Section 2.4.4. Because of the reduced size of the subarrays, the effective array aperture decreases and a new far field distance of 0.97 m is achieved. It must be noted that this boundary should be considered as a rule of thumb approximation and not a discrete line. The array

aperture also depends on the angle of incidence, and the far field evolves into the near field via a transition region [SAZ07].

This paragraph describes an alternative method for decreasing the far field distance, exploiting as much information as possible without averaging spatial covariance matrices of subarrays. The proposed method splits the 10-element array into five 6-element subarrays. However, the results of every subarray are processed independently, resulting in a localization system with five very closely spaced 6-element arrays. The position of every subarray is shifted over a $\lambda/2$ distance and two spatial smoothings are applied following the results of Section 5.4.2, enabling the estimation of up to three signal components. The calculated far field distance of the subarrays is 0.55 m. As demonstrated in Figure 5.8a, increased performance is expected in the vicinity of the array, i.e. in small rooms. In larger setups, no advantages are foreseen because all subarrays will have similar outputs, as depicted in Figure 5.8b.

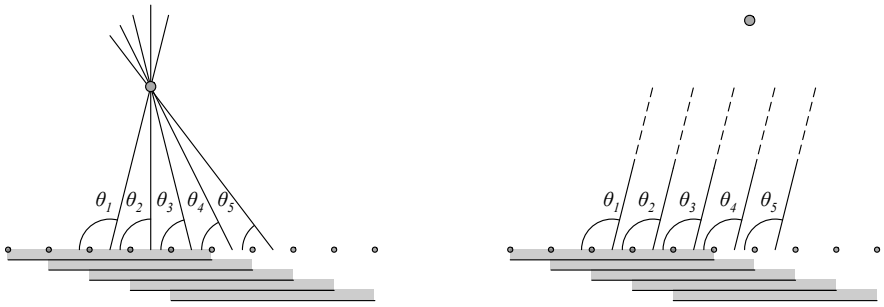

(a) Nearby node position (b) Remote node position

Figure 5.8: LOS example of localization with five subarrays

The performance of the subarray based approach was evaluated in the smallest available room: $\mathrm{TS}_{\mathrm{concrete}}$. The results are summarized in Table 5.12, comparing the performance of a single 10-element array with five 6-element subarrays. Surface intervals indicate that the standard approach with a single 10-element array outperforms the proposed method with five 6-element subarrays. The localization errors are less conclusive, showing slightly improved results in LOS situations and very poor NLOS results. As a conclusion, the proposed method can be labelled unsatisfactory because it fails to bring an overall increase in localization accuracy, in fact it is even more computationally intensive, requiring the execution of localization algorithms for each subarray. The inferior performance of the system can be attributed to the limited amount of signal components that can be detected by a subarray, which is probably insufficient in a dense multipath environment. In the evaluated system, subarrays can distinguish

a maximum of three multipath directions after two spatial smoothings, while the single 10-element approach involves five signal decorrelations and detects up to four signals.

Table 5.12: Comparison of one 10-element array with five 6-element subarrays in test setup $TS_{concrete}$

			surface interval			normalized error		
	setup	algorithm	mean	P50	P95	mean	P50	P95
LOS	1x10	benchmark	0.038	0.026	0.093	–	–	–
		optimal	0.044	0.037	0.138	0.145	0.109	0.352
	5x6	benchmark	0.182	0.130	0.701	0.232	0.223	0.489
		optimal	0.061	0.038	0.200	0.128	0.109	0.450
NLOS	1x10	benchmark	0.298	0.254	0.736	–	–	–
		optimal	0.239	0.150	0.825	0.238	0.219	0.552
	5x6	benchmark	0.320	0.263	0.878	0.291	0.277	0.569
		optimal	0.272	0.145	0.928	0.291	0.256	0.592

5.5.5 Multiple Arrays

Previous paragraphs focused on the use of a single antenna array or dual arrays for localization purposes in rectangular rooms. However, localization accuracy can be further increased by adding more arrays to the room. This results in more spatial information and increases the chance on receiving LOS signals. Following the results of Section 5.5.1, only arrays in the middle of the walls are preferred, leading to a test environment TS_{brick} with maximum four antenna arrays (positions A, B, C and D). This section compares the performance of systems with one to four 10-element antenna arrays in all possible combinations of LOS and NLOS connections. In each configuration, an optimal array placement is preferred. In one-array setups, the array is placed against a shorter wall (A or B). In 2-array setups only orthogonal arrays are considered (AC, CB, BD and DA), following the results of Section 5.5.2. For 3-array setups a similar optimization process was completed, revealing no noticeable preference between the 'short-long-short' or 'long-short-long' wall configuration in 3xLOS and 3xNLOS conditions. Therefore, all possible 3-array configurations are included in this test (ACB, BDA, CAD and DBC). In 4-array tests, only one configuration remains: ABCD. For each system, the influence of NLOS connections is investigated by gradually increasing the number of NLOS connections from zero to maximum.

Figure 5.9 provides an overview of all test results. Mean, P50 and P95 values of surface intervals and normalized localization errors are presented in six separate graphs. Each graph contains results for the benchmark algorithm (plus-signs) and the optimized algorithm (dots, connected by a line). The lines interconnect the results with an equal number of NLOS connections: zero (i.e. only LOS connections) to four. The discussion of these graphs is split into three parts, treating the influence of the number of arrays, (N)LOS connections, and a comparison between the optimized and benchmark algorithm. In the discussions, a situation with only LOS or only NLOS connections is called respectively an all-LOS or all-NLOS situation.

Number of Arrays

The results of the optimized localization algorithms can be observed as a function of the number of arrays, providing some insight in the expected accuracy of different setups. In the next analysis, we take all results into account, including the worst all-NLOS configurations. One-array systems clearly exhibit the poorest performance in terms of surface intervals and localization errors. Mean localization errors amount 14% of the room diagonal (0.78 m in the considered setup), giving a general estimation of the location. The potential performance of the algorithms is illustrated by P50 surface intervals under 4%. However, the one-array setup is not highly reliable with P95 localization errors of 40% of the room diagonal (2.22 m in the considered setup) and P95 surface intervals up to 54%.

Increasing the number of antenna arrays vastly improves performance. Adding just a second array almost halves the P95 values of normalized localization errors to 23% and mean values stay below 9% (0.50 m in the setup). As more arrays are added to the system, further accuracy improvements can be noticed, however the rate of improvement decreases with more arrays. The 4-array setup represents a very accurate and reliable system, which is demonstrated by surface intervals and localization errors. P95 surface intervals stay below 13% and P95 normalized localization errors do not exceed 15%. The median localization error for this setup never exceeds 4.2% of the room diagonal (0.23 m). In a real-world localization system, an even higher performance is expected, as 4xNLOS situations are unlikely and post-processing techniques (e.g., dead reckoning, particle filters, Kalman filters, etc.) can be applied, depending on the application.

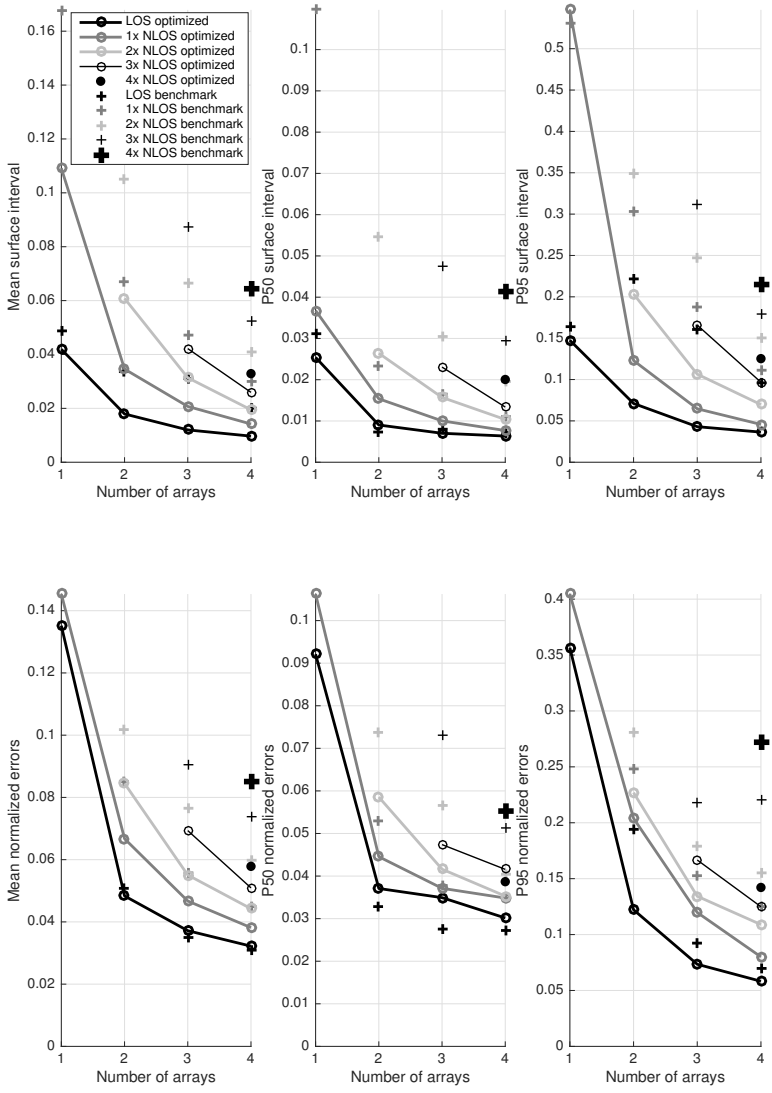

Figure 5.9: Evaluation of system performance for multiple antenna arrays with all-LOS to all-NLOS connections.

NLOS Connections

Intuitively, LOS situations can be expected to yield the best results. This statement can be underpinned with an analysis of LOS and NLOS connections in Figure 5.9. The graphs clearly illustrate that an all-LOS situation always performs best. As soon as two arrays are used, good results are obtained in LOS conditions. Adding more arrays is mainly useful to account for NLOS connections. When two LOS connections are available, mean normalized localization errors under 5% can be expected, as well as P95 values under 12% (0.67 m in the setup). An important remark is that having an additional array with a NLOS connection is always better than having no additional array at all. So generally, NLOS connections still provide useful information that increases the accuracy instead of deteriorating system performance.

All-NLOS scenarios clearly influence surface intervals, with mean values tripling in comparison to the all-LOS scenario. Also in localization errors, an obvious influence can be remarked. The only solution for maximizing the accuracy in an all-NLOS scenario consists of using as much arrays as possible. With four arrays, it is possible to achieve P95 localization errors below 14% (0.83 m in the setup).

Optimized vs. Benchmark Algorithm

Previous discussions of Figure 5.9 only considered the results of the optimized localization algorithm. The benchmark results are also depicted, enabling an interesting assessment of the new algorithm in comparison to the benchmark. The figure shows that the new algorithm outperforms the benchmark in surface intervals and localization errors (with a specific exception of all-LOS P50 localization errors). Benchmark algorithms regularly exhibit double surface interval values, demonstrating their inferior performance. In localization errors, the differences are sligthly less explicit, but they lead to the same conclusion: taking multipath effects into account leads to more accuracy than the classical AoA approach. More specifically, the proposed localization algorithm can achieve similar or better results with less antenna arrays. In several cases, a two-array system with the new algorithm performs better than a 4-array approach with the conventional algorithms, possibly halving hardware and installation costs. Examples of this statement can be seen in all-NLOS localization errors.

In a 4-array system with all-NLOS connections and the benchmark algorithm, P95 normalized localization errors of 27% can be observed. This 1.50 m P95 uncertainty in a 3.4 m x 4.4 m room can be considered unsatisfactory, given the

expensive setup of a 4-array localization system. This result also demonstrates the unsuitability of the benchmark algorithm for NLOS localization.

5.6 Environmental Influences

In previous paragraphs, it has been shown that the performance of the localization system depends on many configurable parameters, e.g., the localization algorithm, the spatial distribution and amount of antennas, etc. This paragraph focuses on the influence of environmental parameters, which obviously cannot be adjusted. Section 5.6.1 investigates the influence of floor and ceiling reflections, while section 5.6.2 provides an analysis of wall materials and room sizes.

5.6.1 Floor and Ceiling Reflections

As discussed in Section 3.2.3, 2D ray tracing simulations are performed to generate a reference dataset of spatial spectra. The 2D simulations are a perpendicular projection of the three-dimensional space on the floor, reducing the complexity of the ray tracer. Signals that are reflected by the floor or the ceiling result in the same floor projection as the signals that did not undergo these reflections [JLW+01]. As a result azimuth angles are not influenced.

However, as reported by [Ben08] and explained in Section 2.1, impinging signals with a non-zero elevation angle will negatively affect the angular estimation. This is caused by the linear antenna array estimating broadside angles instead of azimuth angles. These angles are only equal under the assumption of 0° elevation angles. Furthermore, floor and ceiling reflections can interfere constructively or destructively, affecting the received power levels under certain azimuth angles. These effects have an influence on the measured spatial spectra, possibly reducing localization accuracy. In order to investigate the importance of these effects, tests were performed with and without shielding of floor and ceiling reflections in test setup $TS_{brick,A}$. Table 5.13 presents the surface intervals and normalized localization errors of these tests. First, the standard setup of 24 measurement locations was evaluated without shielding, for the benchmark algorithm as well as the optimized localization algorithm (correlation of raytrace convolution and measured MVDR spatial spectrum). This test was performed twice in exactly the same way (unshielded 1 and unshielded 2), doubling the amount of data and illustrating the repeatability of results. The last two lines of Table 5.13 list the results for a setup with shielded floor and ceiling reflections. For the shielding of these reflections, a 0.6 m by 1.2 m screen of RF absorbers [Eme10] was placed

under and above the antenna array, restricting the received elevation angles from −30° to 30°. The smallest elevation angle of a first order floor/ceiling reflection in this setup is 45° so the created field of view of the antenna array is considered appropriate for the experiment.

Table 5.13: Influence of floor and ceiling reflections in a LOS test setup $TS_{brick,A}$

		surface interval			normalized error		
		mean	P50	P95	mean	P50	P95
Unshielded 1	benchmark	0.037	0.030	0.095	–	–	–
	optimal	0.035	0.027	0.079	0.128	0.100	0.354
Unshielded 2	benchmark	0.063	0.026	0.267	–	–	–
	optimal	0.030	0.018	0.108	0.098	0.063	0.296
Shielded	benchmark	0.151	0.066	0.557	–	–	–
	optimal	0.052	0.034	0.236	0.145	0.096	0.400

The results in Table 5.13 unexpectedly reveal an increase in surface intervals and localization errors when floor and ceiling reflections are blocked. For this counterintuitive result, two explanations could be given: or the floor and ceiling reflections have a substantial beneficial influence on the localization accuracy, or the construction of RF absorbers has a stronger negative effect than the floor and ceiling reflections. The most credible explanation is the latter of both causes, as absorbers are mounted on a construction of plastic and cardboard, placed on less than a wavelength distance from the antenna array. Given this vicinity to the array, antenna properties can be expected to be influenced. It must be noted that surface intervals for the unshielded configuration are already exceptionally low, with P95 values of 7.9% and 10.8%. Also the localization errors in an unshielded configuration can be considered very low with median values of only 10.0% and 6.3% of the room diagonal. Given this precondition and the fact that the shielding construction (consisting of just plastic, cardboard and anechoic tiles) has a negative effect on the performance of the system, we can conclude with reservation that floor and ceiling reflections hardly influence the performance of the system and that the 2D ray tracing approach seems valid.

An important side note in this respect is that all tests were performed with the transmitting and receiving antennas in the same horizontal plane (1.3 m height), ensuring 0° elevation angles for major multipath components (LOS and wall reflections). When transmitting and receiving antennas have different heights, broadside angles will not be equal to azimuth angles. This will degrade performance because the antenna array estimates broadside angles, while the ray tracer only simulates azimuth angles (which is inherent to the 2D approach). This effect was not further investigated and is considered as future work. If

necessary, the effect could be mitigated by using a 2D antenna array, which is able to estimate azimuth and elevation angles.

5.6.2 Wall Materials and Room Size

In order to enable a solid analysis of environmental parameters, tests were performed in a range of environments. The results are listed in Table 5.14, presenting differences across rooms with different sizes and wall materials. Section 5.5.1 led to an ideal array position in the middle of the shortest wall. However, practical limitations required measurements in TS_{XL}, TS_{XXL} and TS_{XXXL} to be performed with the antenna array against the longer wall. In order to keep results comparable, measurement results in TS_{brick} and $TS_{wallboard}$ are presented for short wall array positions (A and B), as well as longer wall array positions (C and D). For test setup $TS_{concrete}$, this is not an issue because of its square shape.

Wall materials

Table 5.14 presents the LOS and NLOS results of three relatively small rooms, built with different wall materials: $TS_{concrete}$, TS_{brick} and $TS_{wallboard}$. In LOS situations, $TS_{concrete}$ presents the best results, with mean normalized errors of only 10.2% and particularly low surface intervals: 8.9% of the room area can be marked with a 95% certainty. However, this result completely inverses in NLOS conditions, as the setup suddenly exhibits worst performance. With P50 localization errors of 21.9% of the room diagonal, the system can be considered underperforming in a 1-array configuration. An explanation for this phenomenon was found by analyzing measured spatial spectra and reference data. Due to the small room dimensions and concrete walls, very strong specular reflections are received, as simulated in section 3.2.5. These strong reflections, together with a powerful LOS connection, result in a spatial spectrum that closely matches the reference data at the proper position, explaining the exceptional results in LOS tests. In NLOS conditions however, the LOS signal becomes undetectable while powerful specular reflections remain. In this case, the most powerful reflection can be mistakenly interpreted as the LOS signal, resulting in large localization errors.

In TS_{brick} and $TS_{wallboard}$, reflections are more attenuated. This means that the interrupted LOS connection might be weak, but it can still be detectable in the spatial spectrum between the other weak signal components, which explains the superior results in NLOS tests. The slightly poorer LOS performance in TS_{brick} and $TS_{wallboard}$, compared to the LOS $TS_{concrete}$ results can be

Table 5.14: Evaluation of localization performance in all test setups

				surface interval			normalized errors		
	setup		algorithm	mean	P50	P95	mean	P50	P95
LOS	$TS_{concrete}$		bench.	0.043	0.027	0.092	–	–	–
			optimal	0.034	0.030	0.089	0.102	0.066	0.255
	TS_{brick}	A,B	bench.	0.049	0.031	0.163	–	–	–
		C,D		0.086	0.044	0.430	–	–	–
		A,B	optimal	0.042	0.025	0.148	0.135	0.092	0.357
		C,D		0.076	0.047	0.234	0.177	0.162	0.394
	$TS_{wallboard}$	A,B	bench.	0.101	0.046	0.594	–	–	–
		C,D		0.123	0.049	0.575	–	–	–
		A,B	optimal	0.076	0.040	0.305	0.129	0.078	0.419
		C,D		0.065	0.039	0.233	0.121	0.104	0.301
	TS_{XL}		bench.	0.031	0.028	0.095	–	–	–
			optimal	0.033	0.021	0.108	0.118	0.073	0.328
	TS_{XXL}		bench.	0.051	0.029	0.127	–	–	–
			optimal	0.039	0.017	0.134	0.118	0.086	0.374
	TS_{XXXL}		bench.	0.063	0.023	0.461	–	–	–
			optimal	0.048	0.028	0.156	0.112	0.093	0.319
NLOS	$TS_{concrete}$		bench.	0.295	0.244	0.723	–	–	–
			optimal	0.241	0.152	0.658	0.232	0.219	0.549
	TS_{brick}	A,B	bench.	0.168	0.110	0.531	–	–	–
		C,D		0.181	0.125	0.532	–	–	–
		A,B	optimal	0.109	0.037	0.547	0.145	0.106	0.405
		C,D		0.148	0.111	0.399	0.172	0.148	0.387
	$TS_{wallboard}$	A,B	bench.	0.188	0.126	0.613	–	–	–
		C,D		0.206	0.108	0.569	–	–	–
		A,B	optimal	0.162	0.102	0.601	0.157	0.122	0.474
		C,D		0.167	0.059	0.577	0.140	0.143	0.287
	TS_{XL}		bench.	0.167	0.080	0.693	–	–	–
			optimal	0.110	0.089	0.274	0.153	0.142	0.431
	TS_{XXL}		bench.	0.163	0.091	0.615	–	–	–
			optimal	0.112	0.067	0.385	0.119	0.097	0.285
	TS_{XXXL}		bench.	0.177	0.079	0.696	–	–	–
			optimal	0.093	0.053	0.377	0.148	0.124	0.342

explained by the (limited) presence of objects in these rooms. For example, $TS_{concrete}$ is a completely empty room, while $TS_{wallboard}$ is equipped with a metallic whiteboard against a wall, resulting in very strong reflections for specific locations of the mobile node. This is demonstrated by increased P95 surface

intervals in $TS_{wallboard}$. A similar increase is not present in P50 surface intervals, illustrating the selective influence of non-LOS-obstructing objects in a room.

Overall, concrete walls can be considered as great reflectors at 2.47 GHz, which is an advantage in LOS localization, but seriously affects NLOS performance. Tests with wallboard and brick walls revealed no significant mutual differences that can be attributed to the wall material. Median normalized localization errors around 8% were reported in LOS conditions. Thanks to the optimized localization algorithm and array placement, these median errors increase only slightly to approximately 11%.

Room size

The results in Table 5.14 can also be used for an analysis of room sizes. Therefore, TS_{brick} results are compared to the large test setups TS_{XL}, TS_{XXL} and TS_{XXXL}, as these rooms are equipped with brick walls. Due to practical limitations, the antenna array was placed against the longer walls, requiring a comparison to $TS_{brick\ C,D}$.

The normalized localization errors of TS_{XL}, TS_{XXL} and TS_{XXXL} in LOS conditions (mean values around 11%) are significantly lower than in setup $TS_{brick\ C,D}$. Also the surface intervals for the larger rooms are generally better than in smaller rooms. However, the advantages of the optimal algorithm over the benchmark algorithm are limited. This demonstrates the weak multipath signals in spacious environments, leaving most of the information in a clear LOS component. In smaller rooms, a denser multipath can be expected, explaining the inferior results in these environments as the 10-element array with five spatial smoothings can distinguish maximum four signals. Among the larger test setups, no significant differences can be remarked. This means that a room of 14.4 m by 19.7 m is large enough to mitigate dense multipath phenomena (i.e. reducing higher order reflections), while a room of 24.7 m by 42.35 m is still small enough to obtain sufficient signal to noise ratios of the most important multipath components.

The same conclusion can be drawn in NLOS situations, as the results of TS_{XL} are also similar to the results of TS_{XXXL}. Using the optimal algorithm vastly improves the P95 surface intervals of the benchmark algorithm, resulting in a reduction of mean surface intervals from 17% to 11%. This is again an improvement over the $TS_{brick\ C,D}$ results. Furthermore, it illustrates that the most important multipath components can still be received and form a significant contribution to the localization process.

As a conclusion, we can state that high localization accuracies can be achieved in

large rooms. In a room of 24.7 m by 42.35 m, median localization errors of 9% of the room diagonal can be obtained in LOS conditions, as well as exceptional P50 surface intervals below 3%. NLOS situations cause only minimal performance degradation, with median normalized errors of 12% and surface intervals of 5%. In small rooms, localization accuracy is generally lower. This is likely the result of a denser multipath.

5.7 5 GHz Evaluation

All previous experiments were performed in the 2.4 GHz ISM band. However, the same tests can be performed in the 5 GHz ISM band, resulting in less than half the array size for an equal number of $\lambda/2$ spaced elements. Shifting towards a higher frequency not only reduces the size of the array and the antennas, it also changes propagation characteristics. The free space path loss is a function of the frequency, specular reflections only occur in flat surfaces with respect to the wavelength, and also scattering and diffraction are wavelength dependent [Bar03]. Therefore, all 2.47 GHz measurements are also performed with a 10-element 5.1 GHz $\lambda/2$ array configuration. The analysis of the results is similar to the 2.47 GHz evaluation but less extensive and with a focus on the comparison with 2.47 GHz results.

5.7.1 Selection of the Best Performing Localization Algorithm

The study of all parameters of the localization algorithm leads to the same conclusions as Section 5.2. However, results are less explicit and some minor inconsistencies exist. These properties are also illustrated by the 'brute force' evaluation of all 666 algorithms in Table 5.15, making an extensive step-by-step demonstration with dedicated tables for each parameter redundant. The evaluation of the localization algorithm can be summarized as follows:

- Matching algorithm: the correlation based approach shows slightly better results than the dot product based algorithms. However, results are not always consistent, which is demonstrated by the dot product based results in the top 5 of best algorithms.
- Reference data: the circularly convolved ray tracing data can generally be considered as the best reference set. In some singular circumstances, the discrete ray tracing data performs slightly better.
- Measurement data: the MVDR spatial spectrum and its deconvolution are well matched. No clear winner can be specified, as mean, median

and P95 localization errors and surface intervals are very close and often contradictory. Following the 2.4 GHz results, the clean MVDR spatial spectrum was selected because it requires less processing and yields similar results.

- Spatial smoothing: similar to the 2.4 GHz tests, the best results are generally obtained at 4, 5, or 6 spatial smoothings. A remarkable result is the exceptional performance for $K_{\mathrm{ss}} = 1$ in LOS conditions. However, this result does not occur in NLOS conditions, justifying the selection of $K_{\mathrm{ss}} = 5$.

Table 5.15: Listing of the five best configurations of the localization algorithm together with the highest ranked LOS benchmark in a 5.10 GHz configuration. Ranking according to the mean surface intervals in LOS and NLOS situations.

	#	matching	reference	measurement	K_{ss}	mean *SI*
LOS	1	correlation	raytrace conv.	MVDR deconv.	1	0.1034
	2	dot product	raytrace discr.	MVDR deconv.	5	0.1045
	3	correlation	raytrace conv.	MVDR	1	0.1055
	4	dot product	raytrace discr.	MVDR deconv.	4	0.1055
	5	correlation	raytrace conv.	MVDR deconv.	4	0.1068
	341	correlation	LOS conv.	MVDR LOS	4	0.2873
NLOS	1	correlation	raytrace conv.	MVDR	4	0.2605
	2	correlation	raytrace conv.	MVDR	5	0.2614
	3	correlation	raytrace conv.	MVDR deconv.	6	0.2622
	4	correlation	raytrace discr.	MVDR deconv.	6	0.2629
	5	correlation	raytrace conv.	MVDR deconv.	4	0.2633
	348	correlation	LOS conv.	MVDR LOS	2	0.3859

The 2.4 GHz conclusions for the localization algorithm remain valid in the 5 GHz band for 10-element arrays: the correlation of circularly convolved ray traced data with a measured MVDR spatial spectrum with 5 spatial smoothing operations is a well-performing configuration for the localization system in both LOS and NLOS situations. Overall performance of the system is significantly lower than 2.4 GHz configurations, a phenomenon that will be investigated further in Section 5.7.2. However, the results clearly demonstrate the superiority of the proposed algorithm over the benchmark approach: in LOS conditions, mean surface intervals are reduced from 29% to 11%. In NLOS situations, mean surface intervals decrease from 39% to 26%. This means that NLOS performance of the optimal algorithm is better than LOS performance of the benchmark algorithm.

5.7.2 Environmental Influences

Table 5.14 presented the influence of environmental parameters on the localization performance in the 2.4 GHz band. These results are not applicable at 5.10 GHz, given the influence of the operation frequency on propagation characteristics. Table 5.16 lists the localization results of all test setups at 5.10 GHz, enabling an assessment of the influence of wall materials and room sizes, as well as a comparison to 2.47 GHz results.

Wall material

In LOS situations in $TS_{concrete}$, TS_{brick} and $TS_{wallboard}$, the accuracy of the system is very similar to the 2.47 GHz configuration. Exceptionally low surface intervals can be remarked, with median values under 4% for the optimized algorithm. In the $TS_{wallboard}$ LOS setup, an increase of P95 surface intervals can be noted. This could be attributed to room furniture, similar to the 2.47 GHz findings in Section 5.6.2. The mean localization errors in the 5.10 GHz LOS setup range between 12% and 17%, which is similar to the 2.47 GHz results. One notable difference exists in the localization errors in the $TS_{concrete}$ setup, demonstrating larger errors at 5.10 GHz (mean values of 17% instead of 10%). This could be attributed to small inhomogeneities in the room structure, causing scattering at shorter wavelengths.

In NLOS situations, 5.10 GHz results are considerably different from 2.47 GHz findings. $TS_{concrete}$ exhibits similar underperformance in 2.47 GHz and 5.10 GHz configurations. However, the TS_{brick} and $TS_{wallboard}$ setups present significantly increased surface intervals and localization errors at 5.10 GHz. These results could be explained by the larger size of the absorbing obstacle, with respect to the wavelength. This means that the LOS component might still be weakly detectable at 2.47 GHz, due to diffraction around the corners of the obstacle. At 5.10 GHz, diffraction should be less explicit, resulting in better LOS obstruction. This is demonstrated by the mean benchmark surface intervals $> 25\%$ for all test setups. In this context, the effectiveness of the optimal algorithm is clearly demonstrated in TS_{brick} and $TS_{wallboard}$, halving many of the benchmark P50 surface intervals.

As a conclusion, concrete environments exhibit worst overall performance. Better results are achieved in brick and wallboard room setups, but no clear winner can be selected. In general, LOS performance of 2.47 GHz and 5.10 GHz systems in the smaller test setups is similar. In NLOS situations, the 2.47 GHz approach is a better option, at least because LOS connections are less easily obstructed at 2.47 GHz due to the larger wavelength.

Table 5.16: Evaluation of localization performance in all test setups at 5.10 GHz

				surface interval			normalized errors		
	setup		algorithm	mean	P50	P95	mean	P50	P95
LOS	$TS_{concrete}$		bench.	0.030	0.026	0.060	–	–	–
			optimal	0.043	0.033	0.111	0.166	0.110	0.567
	TS_{brick}	A,B	bench.	0.028	0.022	0.101	–	–	–
		C,D		0.044	0.017	0.140	–	–	–
		A,B	optimal	0.033	0.027	0.089	0.149	0.098	0.445
		C,D		0.047	0.038	0.163	0.133	0.109	0.326
	$TS_{wallboard}$	A,B	bench.	0.083	0.053	0.371	–	–	–
		C,D		0.140	0.048	0.655	–	–	–
		A,B	optimal	0.063	0.031	0.249	0.127	0.084	0.443
		C,D		0.072	0.043	0.242	0.123	0.104	0.332
	TS_{XL}		bench.	0.095	0.029	0.750	–	–	–
			optimal	0.085	0.057	0.246	0.206	0.181	0.494
	TS_{XXL}		bench.	0.461	0.462	0.937	–	–	–
			optimal	0.181	0.166	0.387	0.258	0.248	0.465
	TS_{XXXL}		bench.	0.327	0.248	0.826	–	–	–
			optimal	0.090	0.053	0.331	0.238	0.256	0.442
NLOS	$TS_{concrete}$		bench.	0.283	0.188	0.804	–	–	–
			optimal	0.213	0.173	0.490	0.238	0.202	0.512
	TS_{brick}	A,B	bench.	0.254	0.180	0.814	–	–	–
		C,D		0.246	0.135	0.693	–	–	–
		A,B	optimal	0.169	0.091	0.726	0.173	0.136	0.429
		C,D		0.160	0.097	0.511	0.173	0.163	0.394
	$TS_{wallboard}$	A,B	bench.	0.267	0.199	0.824	–	–	–
		C,D		0.277	0.212	0.734	–	–	–
		A,B	optimal	0.177	0.109	0.552	0.195	0.164	0.461
		C,D		0.204	0.145	0.544	0.165	0.146	0.308
	TS_{XL}		bench.	0.467	0.444	0.943	–	–	–
			optimal	0.357	0.269	0.931	0.294	0.255	0.708
	TS_{XXL}		bench.	0.451	0.449	0.953	–	–	–
			optimal	0.243	0.152	0.756	0.214	0.218	0.447
	TS_{XXXL}		bench.	0.428	0.409	0.882	–	–	–
			optimal	0.183	0.139	0.491	0.279	0.279	0.484

Room size

In large rooms, localization performance seriously degrades in the 5 GHz band. This contrasts with 2.47 GHz results, which showed superior performance in

these environments. In LOS tests, mean normalized localization errors range between 21% and 27%, which is even worse than the NLOS results in smaller setups. Surface intervals also demonstrate the underperfomance of the system, with benchmark P95 values nearing 95% and P50 values of almost 50% in TS_{XXL}. This means that a random approach is equally efficient, as 50% or 95% of the room surface needs to be selected for respectively 50% or 95% localization certainty. With the optimized localization algorithm, surface intervals can be improved by a factor of three. In NLOS conditions results are even worse, with mean localization errors up to 30% of the room diagonal. Surface intervals are also particularly high, even for the optimal algorithm.

The cause of these inferior results in large setups was investigated by analyzing and comparing measured spatial spectra and reference data. This study revealed that unforeseen strong peaks occur in all measured spatial spectra under fixed angles. These fixed peaks in the spectrum point to anomalies in the room structure: setups TS_{XL}, TS_{XXL} and TS_{XXXL} are sports halls with basket ball rings attached to the walls with metallic constructions. Apparently these metal bars create scattered multipath components at 5.10 GHz, which are very strong in comparison to the specular reflections. The scattered components always impinge under the same angles, independent of the position of the mobile node. Therefore they do not carry spatial information and can only deteriorate system performance. In NLOS situations, the scattered components cause the strongest peaks in the spatial spectra, explaining the unsatisfying performance. It is remarkable that these effects are very pronounced in 5.10 GHz tests, while 2.47 GHz evaluations show no signs of this phenomenon. Also, the scattered signals are only perceptible in the larger setups, while the smaller rooms TS_{brick} and $TS_{wallboard}$ also feature possibly scattering objects in the rooms, supporting the assumption that this must be a signal strength related phenomenon. Summarizing this matter, we can state that metallic objects with a size comparable to the wavelength λ can result in scattered multipath components that heavily affect localization performance. This statement holds especially in large environments (room diagonal of >25 m) and at higher frequencies (5.10 GHz), where signal components are already weakened by losses in the propagation path and the measurement system (e.g., cable losses and reduced amplifier gain [Tex14]).

As a conclusion on room size influences, significant underperformance was noticed in large setups at 5.10 GHz, especially in NLOS situations. This finding was attributed to scattered multipath signals and only manifested in large setups at 5.10 GHz. In smaller rooms better performance was observed, comparable to 2.4.7 GHz results.

5.8 Combining 2.4 GHz and 5 GHz Measurements

Narrowband tests in the 2.4 GHz or 5 GHz band rely on propagation characteristics at a single frequency. However, the propagation channel behaves differently at different frequencies, a property that is exploited by UWB systems [SGG08]. While some frequency components are reflected by an object, others might just transmit through it. Furthermore, the problem of destructive interference in narrowband systems can be eliminated with larger bandwidths. The frequency dependent propagation characteristics can also be exploited by combining multiple narrowband systems. Of course, this approach does not match the potential of an UWB system, but the technique is compatible with contemporary multi-band communication technologies (e.g., 802.11ac [Hoe13] and cellular systems [Mol11], etc.).

This idea is investigated by combining the 2.47 GHz and 5.10 GHz localization results. All test setups are considered for this evaluation, with the 2.47 GHz 10-element $\lambda/2$ array placed at the same position as the 5.10 GHz 10-element $\lambda/2$ array. It is clear that this approach requires two sets of 10 antennas at different positions, given the different inter-element spacings. Because of the $\lambda/2$ spacing at both frequencies, the resolutions of both antenna arrays are comparable and no grating lobes are present. This means that the main influence on localization accuracy can be attributed to the different propagation characteristics, rather than array resolutions. The results are evaluated by comparing mean surface intervals and mean normalized localization errors for the individual frequency components and their combination, as listed in Table 5.17. In this table, only the optimized algorithm is considered (correlation of convolved ray tracing data with a measured MVDR spatial spectrum).

When both individual components yield similar accuracy, the combination generally exceeds the performance of both, as intended. An example can be found in the LOS $\mathrm{TS}_{\mathrm{wallboard}}$ setup, reducing mean surface intervals from 7% to 5%. When both frequency components present strongly different results, the merge of both frequencies leans towards the best of both results, as illustrated by the NLOS $\mathrm{TS}_{\mathrm{XXL}}$ results. However, the best result is usually not exceeded here. In any case, the combination of frequencies always performs better than the worst individual frequency component.

Overall, a dual-frequency setup does not result in a spectacular increase of accuracy over the 2.47 GHz system. This can be attributed to the generally inferior performance of the 5 GHz system. The evaluation illustrates the limited spatial information of a second $\lambda/2$ anchor node at the exact same position.

A setup with 10 dual-band antennas operated in the 2.4 GHz and 5 GHz bands makes more sense from an economical point of view. In this case, $\lambda_{2.4GHz}/2$

Table 5.17: Combining 2.47 GHz and 5.10 GHz results of the optimized localization algorithm

		mean surface interval			mean normalized error		
		2.4 GHz	5 GHz	combo	2.4 GHz	5 GHz	combo
LOS	$TS_{concrete}$	0.0338	0.0426	0.0301	0.1024	0.1662	0.1389
	TS_{brick}	0.0592	0.0398	0.0420	0.1560	0.1413	0.1410
	$TS_{wallboard}$	0.0701	0.0671	0.0467	0.1247	0.1248	0.1071
	TS_{XL}	0.0333	0.0848	0.0311	0.1179	0.2062	0.1762
	TS_{XXL}	0.0388	0.1807	0.0534	0.1177	0.2581	0.1855
	TS_{XXXL}	0.0480	0.0897	0.0419	0.1122	0.2381	0.1109
NLOS	$TS_{concrete}$	0.2413	0.2134	0.1899	0.2323	0.2384	0.2088
	TS_{brick}	0.1286	0.1642	0.1227	0.1588	0.1731	0.1485
	$TS_{wallboard}$	0.1641	0.1907	0.1421	0.1486	0.1800	0.1357
	TS_{XL}	0.1103	0.3565	0.1521	0.1529	0.2944	0.1822
	TS_{XXL}	0.1124	0.2433	0.1164	0.1189	0.2141	0.1593
	TS_{XXXL}	0.0930	0.1830	0.1056	0.1476	0.2793	0.1776

spacing at 2.47 GHz can be assumed, resulting in a higher resolution and grating lobes in the 5.10 GHz band, due to the larger than $\lambda_{5GHz}/2$ inter antenna spacing. This approach potentially achieves higher accuracy, as a solution without grating lobes is combined with a higher resolution (with grating lobes) at 5.10 GHz [PZ02]. This idea resembles a UWB system more closely, but it requires new measurements and is therefore considered future work.

5.9 Assessment of Achievable Accuracies

The proposed localization system was tested in a variety of configurations and environments. The obtained results can be compared to the related work that was presented in Section 2.6.

Table 2.1 shows a mean normalized error of 6.1% for the standard triangulation approach with three arrays in a LOS area. For our system, a value of 3.8% is achieved in these ideal conditions, an improvement that can be attributed to superior hardware (e.g., more antennas).

The single anchor AoA fingerprinting systems of [GCGM09, MCGM10, RWK16] exhibit mean LOS normalized errors between 21.6% and 29.2%. Our approach generally scores between 10% and 13% at 2.47 GHz (Table 5.14), and between 12% and 17% at 5.10 GHz in small to medium sized rooms (Table 5.16). This illustrates the superior accuracy of the proposed system over a labor intensive

fingerprinting implementation. The same conclusion is demonstrated by the 2.47 GHz AoA fingerprinting approach in Section 4.5.2, with a mean normalized error of 15.9% for on-grid evaluations and 21.3% in off-grid conditions (Table 4.4). In NLOS conditions, this fingerprinting approach yields mean normalized errors of 26.8%, compared to 12% to 23% values for the proposed system. The experiments of Section 5.3.1 point to a similar conclusion. All these results were obtained with the same hardware setup and illustrate that a simulation based reference set can result in similar or better localization accuracy, without the time consuming offline training phase. A reason can be found in the fine resolution of the simulated reference set. Also, the simulations only take LOS and specular components into account according to their expected signal strengths. This appears to be a more accurate solution than relying on a single snapshot of the multipath environment. Especially in NLOS conditions, multipath simulations outperform fingerprinting.

Some fingerprinting systems in literature provide a higher localization accuracy in LOS conditions [hFnLcL08, OIS13, TGdAG09]. However, these implementations rely on multiple anchor nodes or even an antenna array at the mobile node. Furthermore, these systems are not tested in a adverse (NLOS) conditions.

The multipath assisted UWB systems that are presented in [MLLW14, KLM$^+$16, MGW10, dVS12, dVWM$^+$12, HPT$^+$16] deliver another class of performance. With P95 values of normalized errors below 3%, these systems can be considered extremely accurate and reliable, compared to the 26% to 37% values in Table 5.14. These exceptional results can be attributed to the UWB ToA approach, delivering an inherently higher accuracy in comparison to narrowband systems, as explained in Section 2.3.1. Only [HPT$^+$16] considered NLOS conditions. This publication reported median normalized errors of 6.3%, still exceeding the LOS performance of our approach. However, UWB systems should not be considered as a better alternative in all situations. While narrowband AoA hardware can be found in contemporary communication systems, UWB localization systems rely on dedicated and costly infrastructure.

5.10 Conclusions Concerning System Performance

Tests are performed in six distinct environments. The results in the 2.4 GHz and 5 GHz bands lead to an optimal localization algorithm, which is based on the correlation of a measured MVDR spatial spectrum with a reference set of simulated spatial spectra. These reference spectra ideally consist of circular convolutions of the discrete ray tracing data with a Hanning window. In terms

of measurement pre-processing, five spatial smoothing operations are selected for best overall performance with a 10-element $\lambda/2$ array.

An evaluation of the multipath simulator reveals that ray traced reference data can result in a higher accuracy than the classical measurement based fingerprinting approach. For the simulated wall permittivity, best results are obtained when the correct wall material is used in ray tracing simulations. However, a precisely modelled environment does not seem essential for obtaining good results.

An evaluation of array hardware parameters provides insights in antenna coupling, the number of array elements and the amount of array snapshots. Antenna coupling strongly deteriorates localization performance, an effect that should be considered when building a non-synthetic hardware setup. The accuracy of the system logically increases with the number of array elements, as demonstrated for 2 to 10 antennas. These tests also enable the prescription of the optimal amount of spatial smoothing operations as a function of the number of antennas. The required number of array snapshots is very low ($N = 5$ is shown to be sufficient) in the considered setup. This result is attributed to the dedicated highly accurate measurement setup.

In terms of array organization, multiple setups are investigated. In single array configurations, the best array position is found in the middle of the shortest wall. Dual array setups perform best in rectangular rooms with one array against a short wall and the other array against a long wall. A study of antenna distributions shows that two distributed 5-element arrays provide better accuracy than a localization system based on a single 10-element array. Another study investigates splitting an array up into multiple sub-arrays, however this does not improve performance. An overall assessment of localization accuracy in multi-array systems demonstrates the ultimate performance of a 4-array setup.

Environmental influences are also investigated. Floor and ceiling reflections are found to have no noticeable negative influence on localization accuracy in the considered setups, justifying the 2D ray tracing approach at least when transmitting and receiving antennas are placed at the same height. An evaluation of system performance as a function of wall materials in the 2.4 GHz and 5 GHz bands reveals underperformance in concrete rooms, while brick and plasterboard rooms exhibit better performance. When considering room sizes, best results are obtained in the largest rooms in the 2.4 GHz band. In the 5 GHz band, these rooms exhibit worse performance due to the increased susceptibility to scattering. A merge of a 2.47 GHz and 5.1 GHz system is tested, revealing no significant performance gain in the test configuration.

Throughout this chapter, the superiority of the optimized algorithm over the

benchmark is clearly demonstrated, proving that localization accuracy can be enhanced by exploiting multipath effects. The achievable performance depends on a range of hardware and environmental parameters, making it impossible to reduce the overall accuracy to a single value. However, the obtained results are compared to various results in the scientific literature. Improved performance is observed in comparison to classical AoA triangulation systems and fingerprinting approaches. However, the exceptional performance of UWB multipath assisted systems is unparallelled.

Chapter 6 explores the possibility of combining the proposed multipath assisted AoA localization method with RSS or ToF based techniques, aspiring a further increase of localization accuracy and robustness.

Chapter 6

Combination of Localization Techniques

The proposed multipath assisted localization system only considers AoA information. However, a combination of localization techniques might improve overall accuracy and robustness, as described in Section 2.6.5. This chapter starts with Section 6.1, explaining how the existing AoA approach is tailored for RSS or ToF measurements. Section 6.2 details the RSS implementation of the positioning framework, followed by an evaluation of the accuracy in practical setups. A similar discussion of the ToF implementation is provided in Section 6.3. The RSS and ToF techniques are combined with the AoA approach in Section 6.4, which provides an overall assessment of accuracy improvements. The conclusions of this chapter are summarized in Section 6.5.

6.1 Localization Framework

The localization framework that was introduced in Chapter 3 relies on a fingerprinting approach, matching simulated reference vectors $\boldsymbol{f}_i$ to an AoA measurement vector $\boldsymbol{m}$ in order to obtain an SPDF. The multipath simulator can also be used for generating a training set of RSS or ToF fingerprints, enabling distance based positioning within the existing localization framework of Figure 3.1. The following sections explain how $\boldsymbol{f}_i$ and $\boldsymbol{m}$ vectors are conceived in an RSS or ToF based system, and how they result in an SPDF. The focus of this research is on finding a compatible solution that can integrate RSS

or ToF to potentially increase the accuracy of an AoA system. An extensive optimization of RSS or ToF techniques is therefore out of scope.

6.2 RSS Localization

RSS based fingerprinting is a common technique for indoor positioning. While most systems rely on a labor intensive survey phase, ray tracing has previously been studied as a source for reference data [WTCL15, TCL+17]. This section describes an RSS fingerprinting implementation based on the available localization framework. For RSS measurements, the antenna array for AoA estimation is used.

6.2.1 Reference Data

The RSS training data set $\mathcal{T}_{\text{RSS}}$ contains a signal loss value (in dB) for each position of the mobile node $\boldsymbol{p}_i$. This means that the $\boldsymbol{f}_{\text{RSS},i}$ vectors contain a single scalar value, in contrast to the angular PDF in AoA fingerprints. In order to generate the reference vectors, the multipath simulator of Section 3.2.3 is utilized. The signal losses L_{ray} are computed for the LOS and reflected rays between the mobile node and the array, which are simulated as point sources. Since a directional patch antenna is used at the receiver side, also the antenna gain $G_{\text{patch}}(\theta)$ is taken into account. The radiation pattern is illustrated in Figure 4.6, affecting the RSS as a function of θ. Equation 6.1 expresses the fingerprint value $\boldsymbol{f}_{\text{RSS},i}$ as a function of L_{ray} and $G_{\text{patch}}(\theta)$. All ray losses are linearly combined, resulting in a single loss value, representing $L_{\text{path}} - G_{\text{patch}}$ [dB].

$$\boldsymbol{f}_{\text{RSS},i} = L_{\text{path}} - G_{\text{patch}}\ [\text{dB}] = -10 \cdot \log_{10} \sum_{\text{ray}} 10^{\frac{G_{\text{patch}}(\theta_{\text{ray}}) - L_{\text{ray}}}{10}} \tag{6.1}$$

In contrast to common RSS schemes in Section 2.2, no statistical model with survey-based path loss exponents is used, as described by Equation 2.2. Instead, a deterministic ray tracing method is applied, linearly combining all signal strengths. This represents a simplified model, assuming constructively interfering multipath components. The outcome approximates the waveguide effect that occurs in favorable LOS environments, resulting in $n_{\text{path}} < 2$ as discussed in Section 2.2.

6.2.2 Measurement Data

In order to acquire RSS data, the synthetic antenna array that was proposed in chapter 4 for AoA measurements can be used. The signal amplitudes indicate the received power P_{Rx} for each array channel. Since multiple channels are available, signal powers can be averaged, countering small scale fading effects [Sey05].

The RSS measurement vector $\boldsymbol{m}_{\mathrm{RSS}}$ should match the corresponding fingerprint vector from training data. These reference vectors contain a scalar value, representing the combination of path loss and patch antenna gain. This value can be calculated from measurements if all necessary system parameters are known. Equation 6.2 is based on the link budget Equation 2.1, expressing the measurement vector as a function of the transmitted power P_{Tx}, averaged received power $\overline{P_{\mathrm{Rx}}}$, omnidirectional transmit antenna gain G_{dipole}, cable losses L_{cable} and amplifier gain G_{amp}.

$$\boldsymbol{m}_{\mathrm{RSS}} = L_{\mathrm{path}} - G_{\mathrm{patch}}\ [\mathrm{dB}] = P_{\mathrm{Tx}} - \overline{P_{\mathrm{Rx}}} + G_{\mathrm{dipole}} - L_{\mathrm{cable}} + G_{\mathrm{amp}} \tag{6.2}$$

6.2.3 Matching algorithm

Since $\boldsymbol{f}_{\mathrm{RSS},i}$ and $\boldsymbol{m}_{\mathrm{RSS}}$ vectors represent a single scalar value, a more basic matching algorithm can be conceived in comparison to the AoA approach. As stated in Section 2.5, a location can be found as the closest euclidean distance between the RSS vectors. Equation 6.3 expresses the RSS SPDF $r_{\mathrm{SPDF,RSS}}(i)$ as a function of the euclidean distance between $\boldsymbol{f}_{\mathrm{RSS},i}$ and $\boldsymbol{m}_{\mathrm{RSS}}$.

$$r_{\mathrm{SPDF,RSS}}(i) = \frac{\max\limits_{i\in\{1,\ldots,N_f\}} |\boldsymbol{f}_{\mathrm{RSS},i} - \boldsymbol{m}_{\mathrm{RSS}}| - |\boldsymbol{f}_{\mathrm{RSS},i} - \boldsymbol{m}_{\mathrm{RSS}}|}{\sum\limits_{i=1}^{N_f} \left(\max\limits_{i\in\{1,\ldots,N_f\}} |\boldsymbol{f}_{\mathrm{RSS},i} - \boldsymbol{m}_{\mathrm{RSS}}| - |\boldsymbol{f}_{\mathrm{RSS},i} - \boldsymbol{m}_{\mathrm{RSS}}| \right)} \tag{6.3}$$

Figure 6.1 depicts an example RSS SPDF in the $\mathrm{TS_{XXL}}$ setup. Most importantly, this single anchor SPDF does not provide a location estimate, as it can only be used for ranging. For RSS localization, at least three anchor nodes are required, as stated in Section 2.1. Furthermore, the shape of the 'range estimate' (i.e. the white area in Figure 6.1) is not circular, due to the directional radiation pattern of the patch antenna.

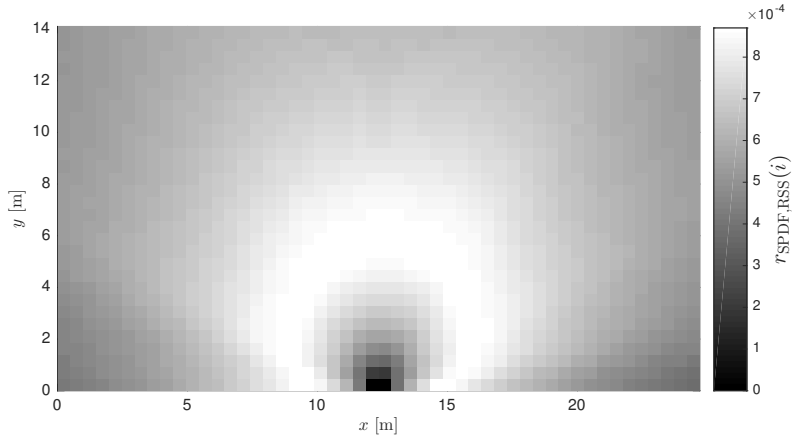

Figure 6.1: Example RSS SPDF in $\mathrm{TS}_{\mathrm{XXL}}$

6.2.4 Accuracy

The accuracy of the RSS approach cannot be evaluated in terms of localization errors, as the SPDF for a single anchor node does not converge to a single position. However, the surface intervals can provide information on the effectiveness of the algorithm. Table 6.1 lists the mean, median and P95 *SI* values for all evaluated setups at 2.47 GHz in LOS and NLOS conditions. Comparing these values to the AoA results of Table 5.14 highlights the poor performance of the RSS approach, with LOS RSS *SI* values inferior to the NLOS AoA results. The reduced performance of RSS localization can partly be attributed to the non-converging SPDF. Another problem could be related to the multipath simulator, only calculating LOS and specularly reflected signal contributions. In an AoA approach, this technique is sufficient because only these components deliver spatial information and exact signal strengths are of minor concern, as illustrated by Section 5.3.2. In an RSS system more accurate information is required on signal strengths. Furthermore, the signal strength is heavily affected by signal obstructions. This is a non-predictable factor, further reducing the accuracy in NLOS situations. The NLOS results in Table 6.1 show P50 values around 0.50 and P95 values around 0.95. As mentioned in Section 3.7.3, these results represent the performance of a random localization approach, making the RSS system useless in NLOS situations.

Table 6.1: Surface intervals for the proposed RSS localization system in LOS and NLOS conditions at 2.47 GHz

	Surface Intervals					
	LOS			NLOS		
	mean	P50	P95	mean	P50	P95
$TS_{concrete}$	0.333	0.316	0.679	0.591	0.614	0.914
TS_{brick}	0.276	0.257	0.764	0.543	0.523	0.961
$TS_{wallboard}$	0.360	0.299	0.829	0.446	0.453	0.864
TS_{XL}	0.304	0.288	0.709	0.522	0.459	0.924
TS_{XXL}	0.304	0.277	0.719	0.504	0.515	0.940
TS_{XXXL}	0.354	0.343	0.747	0.374	0.289	0.971

6.3 ToF Localization

ToF based UWB multipath assisted positioning systems have been presented recently in literature, as discussed in Section 2.6.3. This section presents a ToF based localization method in the 2.4 GHz ISM band, based on the existing localization framework. The main focus of this work is on the general feasibility and possible complementarity to the AoA approach in communication systems, rather than optimizing the ToF localization accuracy regardless of the required hardware.

6.3.1 Measurement Data

Since the AoA hardware setup does not allow ToF measurements, a commercial off-the-shelf solution is considered: the nanoLOC® Development kit from Nanotron Technologies. These modules implement the IEEE 802.15.4a standard [KPGT10], using a Chirp Spread Spectrum (CSS) technique in the 2.4 GHz ISM band [Nan10]. An SDS-TWR technique is applied, resulting in a reported 2 m indoor ranging accuracy (however it was not specified whether this is a mean, median or other error value). The system represents a basic ToF setup which performs a simple range estimation based on a narrowband measurement. This approach is not comparable to the dedicated UWB solutions that are used in literature, providing accurate and complete power delay profiles. However, in the current feasibility study, the basic setup can still give an indication of the value of ToF measurements.

The output of the system for a single measurement represents the measured path length as a scalar value (in m). In an anechoic environment with a LOS connection, this is the distance between the mobile device and the anchor

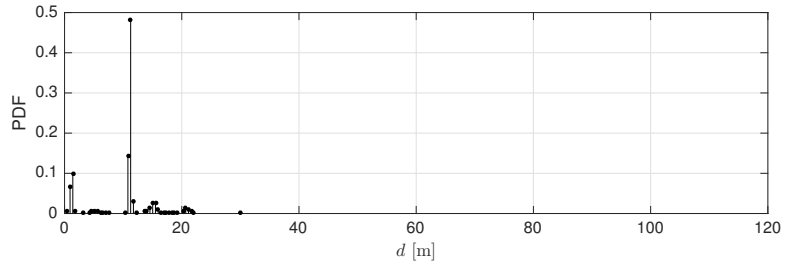

Figure 6.2: Example of a measured distance PDF ($\boldsymbol{m}_{\mathrm{ToF}}$) in $\mathrm{TS}_{\mathrm{XXL}}$

node. However, in a multipath environment with NLOS connections, other pathways might be involved, resulting in a longer distance estimation. All signal processing for the distance measurements is performed on the nodes, so no information on different propagation paths is readily available. In an attempt to overcome this issue, 1201 distance measurements are performed in a set (cfr. the number of array snapshots in one AoA measurement N). Given the time variant nature of the propagation channel, these 1201 distance estimates can provide information of different propagation paths. More specifically: the majority of the measurements indicates the strongest signal paths. The result of these 1201 distance measurements can be represented as a discrete PDF (i.e. a normalized histogram), indicating the probability for each distance measurement. This function $\boldsymbol{m}_{\mathrm{ToF}}$ exhibits resemblance to a power delay profile, which expresses the received power as a function of signal delay τ. The relationship between τ and the distance d is denoted by Equation 2.4 in Section 2.3. Figure 6.2 depicts an example of a measured distance PDF based on 1201 distance measurements in $\mathrm{TS}_{\mathrm{XXL}}$.

6.3.2 Reference Data

The measurement vector $\boldsymbol{m}_{\mathrm{ToF}}$ represents the travelled distances of all signal paths. In order to generate a reference data set with similar vectors $\boldsymbol{f}_{\mathrm{ToF},i}$, the unfolded path lengths can easily be calculated with the multipath simulator, which also delivers the signal attenuation for each path.

However, the measurements are performed with an SDS-TWR setup, relying on three signal transmissions to determine the distance d. Each transmission could follow a different path, increasing the total number of signal paths to the power of three. The probability of each path is determined by the simulated path losses. The result is a discrete distance PDF, based on the combined signal path lengths. In analogy to Section 3.3.1, these discrete values are convolved

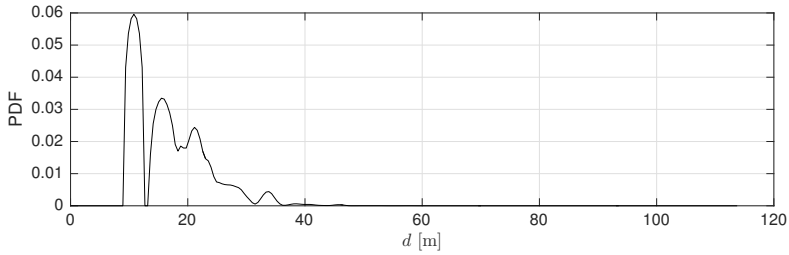

Figure 6.3: Example of a simulated distance PDF in $\mathrm{TS_{XXL}}$

with a 4 m wide hanning window, creating a continuous PDF that takes the reported 2 m ranging errors into account. Figure 6.3 depicts an example of a simulated distance PDF in $\mathrm{TS_{XXL}}$.

6.3.3 Matching algorithm

The existing localization framework performs a position estimation by means of an SPDF, which is created by matching $\boldsymbol{f}_{\mathrm{ToF},i}$ vectors to $\boldsymbol{m}_{\mathrm{ToF}}$. Given the positive results for correlation based matching of AoA vectors in Chapter 5, a similar approach is applied for the ToF implementation. Equation 3.14 is used for the calculation of correlation coefficients, while Equation 3.16 describes the normalization for calculating the SPDF vector.

Figure 6.4 depicts an example ToF SPDF, highlighting the location of the mobile node. Given the symmetric nature of the room and the position of the anchor node, symmetry can also be remarked in the SPDF. Therefore, the ToF approach does not allow localization with a single anchor node.

6.3.4 Accuracy

The accuracy of the ToF approach was evaluated in three setups, listed in Table 6.2. The results for the $\mathrm{TS_{brick}}$ setup display a similar underperformance as the RSS based approach: in LOS conditions positioning is possible but not highly accurate, while NLOS performance comes close to randomness. However, this underperformance can be linked to the small room size of $\mathrm{TS_{brick}}$, which is comparable to the reported nanoLOC® ranging errors of 2 m. In the larger setups $\mathrm{TS_{XXL}}$ and $\mathrm{TS_{XXXL}}$, better performance can be remarked. *SI* values do not equal the accuracy of an AoA system (in Table 5.14), but localization

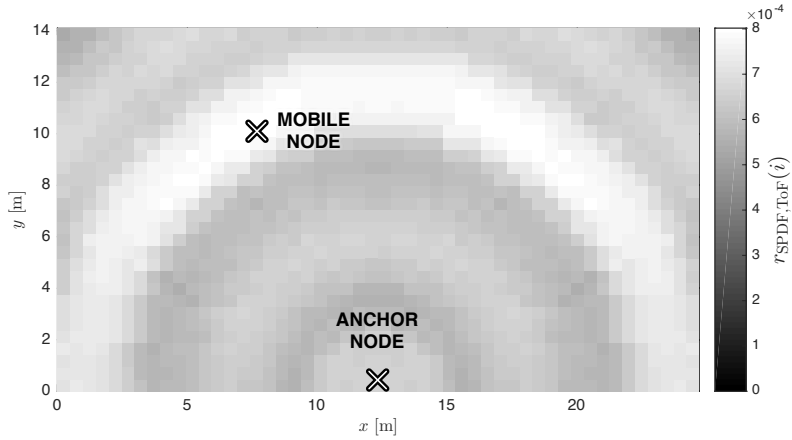

Figure 6.4: Example ToF SPDF in $\mathrm{TS_{XXL}}$, based on the correlation coefficients of $\boldsymbol{m}_{\mathrm{ToF}}$ and $\boldsymbol{f}_{\mathrm{ToF},i}$

effectiveness is demonstrated by P50 and P95 values significantly below 0.50 and 0.95 in LOS and NLOS situations.

Table 6.2: Surface intervals for the proposed ToF localization system in LOS and NLOS conditions in the 2.4 GHz ISM band

	Surface Intervals					
	LOS			NLOS		
	mean	P50	P95	mean	P50	P95
$\mathrm{TS_{brick}}$	0.253	0.223	0.677	0.454	0.436	0.883
$\mathrm{TS_{XXL}}$	0.093	0.073	0.253	0.252	0.199	0.691
$\mathrm{TS_{XXXL}}$	0.137	0.131	0.339	0.248	0.180	0.756

6.4 Combined Localization Techniques

As discussed in the related research Section 2.6.5, a combination of localization techniques can result in a performance increase. The multipath assisted AoA approach can easily be merged with the RSS or ToF based schemes by combining SPDF vectors (assuming they are equally sized), in analogy to the multi-anchor solution in Section 3.6. All following results rely on the best AoA method, using the correlation coefficients of measured MVDR spatial spectra with a reference set of artificial spatial spectra.

6.4.1 RSS + AoA

The RSS approach that was described in Section 6.2 exhibits poor LOS performance and can even be considered useless in NLOS situations. However, adding RSS to an AoA system comes at no extra hardware cost, so every accuracy improvement (even if only in LOS conditions), is considered valuable.

Equation 6.4 represents the merge of an AoA SPDF with RSS results. Because of the difference in accuracies, the weight factors w_{AoA} and w_{RSS} are introduced ($w_{\mathrm{AoA}} + w_{\mathrm{RSS}} = 1$).

$$r_{\mathrm{SPDF,AoA,RSS}}(i) = w_{\mathrm{AoA}} \cdot r_{\mathrm{SPDF,AoA}}(i) + w_{\mathrm{RSS}} \cdot r_{\mathrm{SPDF,RSS}}(i) \tag{6.4}$$

Figure 6.5 depicts the mean, P50 and P95 values of LOS and NLOS surface intervals over all test scenarios, as a function of the AoA-RSS weight distribution. The superior results of the AoA approach are clearly depicted. However, the AoA accuracy can slightly be increased in LOS scenarios by including RSS information with a weight factor of 0.2 to 0.4. In NLOS situations, no conclusive effects can be perceived. As a result, the weight factor values $w_{\mathrm{AoA}} = 0.7$ and $w_{\mathrm{RSS}} = 0.3$ are appointed for AoA-RSS combinations (and will also be used in Section 6.4.3).

6.4.2 ToF + AoA

For the combination of ToF and AoA information, a similar approach is followed with weight factors w_{ToF} and w_{AoA}, as expressed in Equation 6.5.

$$r_{\mathrm{SPDF,AoA,ToF}}(i) = w_{\mathrm{AoA}} \cdot r_{\mathrm{SPDF,AoA}}(i) + w_{\mathrm{ToF}} \cdot r_{\mathrm{SPDF,ToF}}(i) \tag{6.5}$$

Figure 6.6 represents the surface intervals for each weighted combination of ToF and AoA SPDFs in $\mathrm{TS}_{\mathrm{brick}}$, $\mathrm{TS}_{\mathrm{XXL}}$ and $\mathrm{TS}_{\mathrm{XXXL}}$. Again the superiority of the AoA algorithm is demonstrated, but some minor improvements can be remarked in LOS situations for $w_{\mathrm{AoA}} = 0.7$ and $w_{\mathrm{ToF}} = 0.3$. These values will also be used in the next section.

6.4.3 ToF + RSS + AoA

A combination of ToF, RSS and AoA data can be achieved by merging $r_{\mathrm{SPDF,AoA,RSS}}(i)$ and $r_{\mathrm{SPDF,AoA,ToF}}(i)$ with weight factors $w_{\mathrm{AoA,RSS}}$ and $w_{\mathrm{AoA,ToF}}$, as described by Equation 6.6.

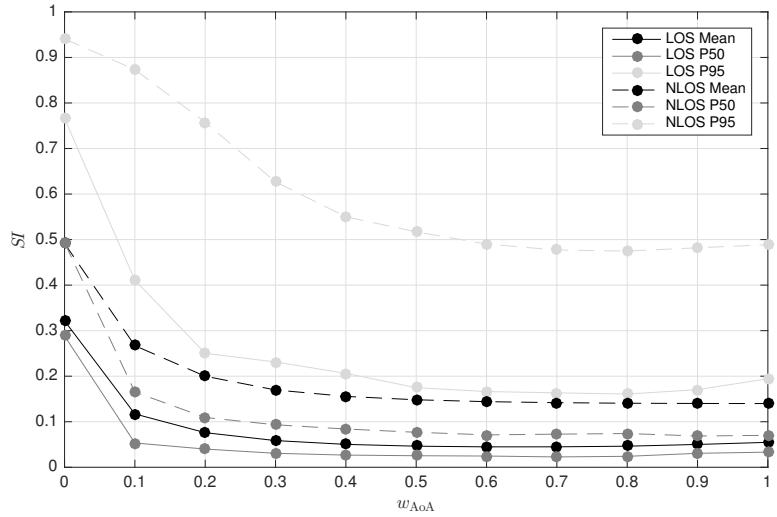

Figure 6.5: AoA-RSS combination: mean, P50 and P95 values of LOS and NLOS surface intervals over all test scenarios, as a function of w_{AoA}

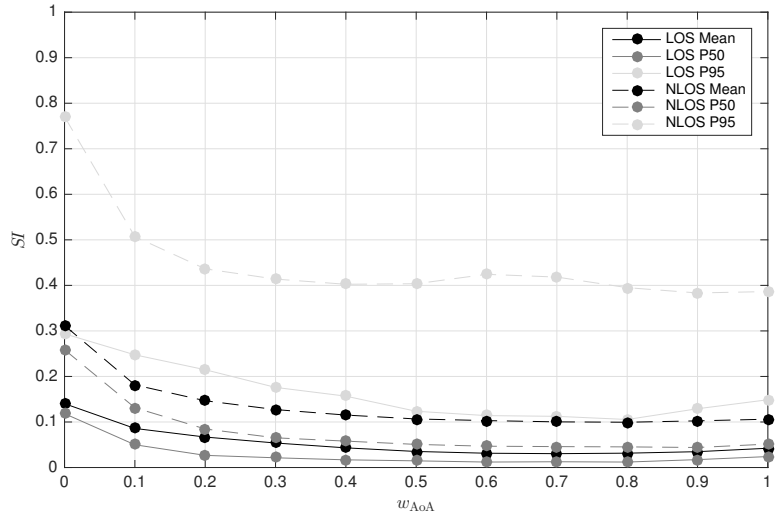

Figure 6.6: AoA-ToF combination: mean, P50 and P95 values of LOS and NLOS surface intervals in $\mathrm{TS}_{\mathrm{brick}}$, $\mathrm{TS}_{\mathrm{XXL}}$ and $\mathrm{TS}_{\mathrm{XXXL}}$, as a function of w_{AoA}

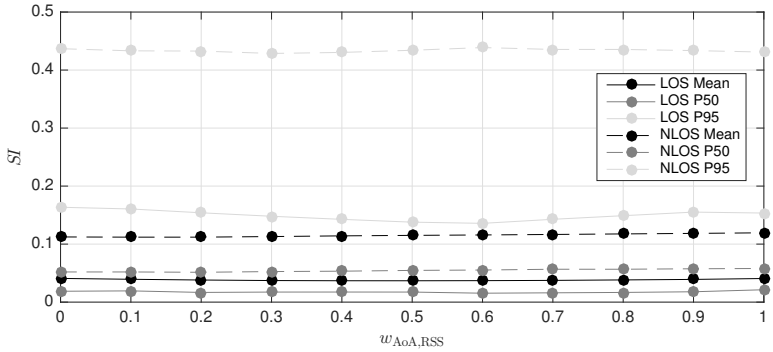

Figure 6.7: AoA-ToF-RSS combination: mean, P50 and P95 values of LOS and NLOS surface intervals in $\mathrm{TS_{brick}}$, $\mathrm{TS_{XXL}}$ and $\mathrm{TS_{XXXL}}$, as a function of $w_{\mathrm{AoA,RSS}}$

$$\begin{aligned} r_{\mathrm{SPDF,AoA,ToF,RSS}}(i) = w_{\mathrm{AoA,RSS}} \cdot r_{\mathrm{SPDF,AoA,RSS}}(i) \\ + w_{\mathrm{AoA,ToF}} \cdot r_{\mathrm{SPDF,AoA,ToF}}(i) \end{aligned} \tag{6.6}$$

The surface intervals for each combination of AoA-RSS and AoA-ToF SPDFs are depicted in Figure 6.7 for the $\mathrm{TS_{brick}}$, $\mathrm{TS_{XXL}}$ and $\mathrm{TS_{XXXL}}$ test setups. The performance gain of this configuration is very limited, but minor improvements occur for $w_{\mathrm{AoA,RSS}} = 0.5$ and $w_{\mathrm{AoA,ToF}} = 0.5$.

6.4.4 Accuracy Assessment

In order to evaluate the performance of combined localization techniques in the 2.4 GHz band, localization results are summarized in Table 6.3. This table lists the mean surface intervals and mean normalized localization errors for all test setups in LOS and NLOS conditions.

In LOS conditions, the AoA-RSS combination delivers a slight improvement of surface intervals and localization errors over the bare AoA method. In NLOS conditions, the results remain inconclusive: the AoA-RSS results approximate the AoA accuracy. These findings can be explained with Table 6.1, as NLOS RSS measurements approach randomness. As a conclusion, RSS can be added to an AoA system for limited LOS positioning improvements at no hardware cost.

The AoA-ToF combination shows no LOS or NLOS accuracy improvements for the TS_{brick} setup. This underperformance can be explained by the small room size, which approximates the reported ranging errors of the used hardware. However, in large test setups TS_{XXL} and TS_{XXXL}, the AoA-ToF method exhibits superior performance. In LOS situations, localization errors are more than halved in comparison to the AoA approach, and also NLOS results are improved. As a conclusion, ToF measurements can deliver a significant contribution to localization accuracy in large environments. However, when the ToF measurement errors approach the room size, RSS is a better option.

The combination of AoA, ToF and RSS information generally results in a suboptimal averaged accuracy. Therefore, the AoA-RSS combination forms the best option in small rooms, while AoA-ToF is the optimal choice for large environments (with the considered ToF hardware setup).

Table 6.3: Mean surface intervals and mean normalized errors for combined localization techniques in the 2.4 GHz band

		Mean Surface Intervals				Mean Normalized Errors			
		AoA	AoA RSS	AoA ToF	AoA RSS ToF	AoA	AoA RSS	AoA ToF	AoA RSS ToF
LOS	$TS_{concrete}$	0.034	**0.028**	–	–	0.102	**0.098**	–	–
	TS_{brick}	0.060	**0.043**	0.060	0.046	0.156	0.089	0.086	**0.079**
	$TS_{wallboard}$	0.070	**0.058**	–	–	0.125	**0.114**	–	–
	TS_{XL}	0.033	**0.029**	–	–	0.118	**0.092**	–	–
	TS_{XXL}	0.039	0.037	**0.020**	0.026	0.118	0.092	**0.041**	0.048
	TS_{XXXL}	0.048	0.046	**0.026**	0.034	0.112	0.104	**0.049**	0.078
NLOS	$TS_{concrete}$	0.241	**0.229**	–	–	0.232	**0.227**	–	–
	TS_{brick}	**0.129**	0.136	0.140	0.138	0.159	**0.146**	0.186	0.17
	$TS_{wallboard}$	0.164	**0.163**	–	–	0.149	**0.142**	–	–
	TS_{XL}	**0.110**	0.112	–	–	0.153	**0.147**	–	–
	TS_{XXL}	0.112	0.113	**0.098**	0.104	0.118	0.115	**0.098**	0.102
	TS_{XXXL}	0.093	0.091	**0.074**	0.081	0.148	0.122	**0.091**	0.105

6.5 Conclusions Concerning the Combination of Localization Techniques

This chapter investigated how RSS and ToF techniques can be applied for further accuracy improvements of the developed AoA localization algorithm. The AoA framework with the multipath simulator is reused and accommodated for RSS and ToF positioning.

The RSS implementation represents a simple approach, as the fingerprints and measurement vectors contain a single scalar value that expresses the signal attenuation. Furthermore, measurements can be performed with the existing AoA setup, imposing no extra hardware costs. Tests indicate a low accuracy improvement in LOS conditions. In NLOS situations RSS can even be considered useless, as its performance approaches randomness.

The ToF solution relies on measured and simulated path lengths. A dedicated SDS-TWR setup with on-board signal processing is used, although the hardware limitations of this setup restrict a full exploitation and evaluation of ToF measurements. For example, access to the raw measurement data could further improve results. Also, a larger bandwidth would reduce ranging errors, which is currently a major problem in small rooms. However, the potential of ToF systems is demonstrated, delivering better performance in LOS and NLOS situations in comparison to the RSS approach.

Localization techniques can easily be combined by taking the weighted average of SPDFs. After the selection of the ideal weight factors, the combined accuracies can be evaluated. The AoA-RSS combination results in a slightly improved accuracy in LOS conditions. On the other hand, the AoA-ToF combination exhibits very promising results in LOS and NLOS situations, in spite of the basic hardware setup. Further research with more advanced hardware is required to optimize the localization approach and investigate the achievable performance. Lastly, the merge of AoA, ToF and RSS data is studied, presenting sub-optimal performance on all counts.

Chapter 7

Conclusions and Future Work

Each chapter concluded with a specific summary of the obtained results. This final chapter provides the overall conclusions and discusses future work, situating this research in a general context.

7.1 Conclusions

This work presented a multipath assisted indoor AoA localization method. The research and evaluation process follows a structured approach based on a set of research questions, which are answered throughout this book and recapitulated in this section.

The proposed positioning technique relies on an AoA measurement vector $\boldsymbol{m}$, which is matched to a set of simulated reference vectors $\boldsymbol{f}_i$, resembling a fingerprinting approach. The measurement vector consists of a discrete or continuous spatial spectrum, indicating the incident power for all angles. This spectrum is calculated using an MVDR, MUSIC or ESPRIT AoA estimation algorithm, in combination with forward-backward averaging, spatial smoothing, and possibly a circular convolution or deconvolution with a Hanning window. The reference vectors are computed in a multipath simulation framework, which relies on a-priori known floor plan information. Therefore, a 2D ray tracer was developed, simulating LOS and specularly reflected signal components according to the image method. The results can be represented as a discrete spatial spectrum, but a continuous version can be created with the MVDR algorithm or a circular convolution with a Hanning window. An extensive step

by step evaluation of the proposed localization system demonstrated the value of the ray tracing approach and lead to an ideal configuration of measurement vectors, reference vectors and a matching algorithm. The best results are obtained with an MVDR measurement vector and a reference set of artificial spatial spectra, created by the circular convolution of discrete ray tracing data with a Hanning window. The matching of a measurement vector with reference vectors is ideally performed by calculating correlation coefficients. These values result in an SPDF, indicating the location probability.

In order to test the proposed localization method in a variety of environments and configurations, a flexible hardware setup was built. The mobile node is represented by an omnidirectional antenna, transmitting a carrier signal at 2.47 GHz or 5.10 GHz. The anchor node consists of a linear phased antenna array, allowing AoA estimation based on phase and amplitude measurements. Given the early research stage, a flexible and low complexity synthetic array design was selected for experiments in static environments. This approach omits mutual antenna coupling and relies on signal measurements with a vector network analyzer, providing accurate phase and amplitude readings. An evaluation of this setup with 10 virtual $\lambda/2$ spaced dual band patch antennas indicated satisfactory performance for the intended multipath localization tests.

The indoor positioning system was tested in six distinct rooms with varying sizes and building materials, representing real-world environments. The first tests evaluated the performance of the ray tracer. A comparison between simulated and measured reference data revealed that simulations result in an equal or even better localization accuracy. This indicates that the implemented solution with coarse floor plan information is sufficient. Moreover, the system was shown to be highly tolerant to deviations in wall permittivity. An evaluation of hardware configurations demonstrated how the accuracy increases as the number of antennas varies from 2 to 10. Also the optimal amount of spatial smoothing was defined as a function of the number of antennas in the array ($K_{\mathrm{ss}} = 5$ for $M = 10$). Furthermore the required number of array snapshots was determined as only 5, this low value can be attributed to the dedicated measurement setup. The synthetic array also omits mutual coupling, however tests showed that this effect is adverse to localization accuracy and should be taken into account in non-synthetic arrays. Further tests focused on the geometric organization of antenna arrays in rectangular rooms. The best array positions were found in the middle of the shortest wall. In the case of multiple anchor nodes, orthogonal walls are preferred. Furthermore, a spatial distribution of antennas was found to be advantageous, as two 5-element arrays deliver a higher accuracy than one 10-element array. Localization accuracies were investigated for systems with up to four arrays and all possible combinations of LOS and NLOS connections. The results of these tests indicate that the multipath assisted approach can result in

similar or better performance in comparison to the benchmark algorithm, while using less anchor nodes. Especially in NLOS situations, the proposed method delivers a significant accuracy improvement. Additional research focused on the influence of environmental factors and the operating frequency. When comparing the influence of building materials on localization accuracy in the 2.4 GHz and 5 GHz band, concrete was observed to reduce performance in comparison to brick or plasterboard walls. Furthermore, large rooms are preferable from a localization accuracy point of view, however signal attenuation in the 5 GHz band should be considered. Also, scattering might be a bigger concern at shorter wavelengths (i.e. in the 5 GHz band). In general, 2.4 GHz systems were shown to be superior to 5 GHz implementations, and a merge of these two systems revealed no significant performance gains.

The outcomes of the experiments often follow the expectations. NLOS localization is clearly more challenging than LOS positioning, and increasing the number of antennas or arrays logically results in a higher localization accuracy. However, some results were found to be remarkable, unexpected or even counterintuitive. For example, the influence of mutual coupling heavily impacts localization accuracy, bringing LOS and NLOS accuracy at the same level. Another remarkable result was found when the array is placed in a corner of the room: with the considered experimental setup, the benchmark algorithm appears to outperform a multipath assisted approach. From a frequency point of view, 5 GHz signals could be expected to result in higher resolutions and consequently a better localization performance, given the shorter wavelengths. However, the contrary was observed due to an increased path loss and scattering. Of course, also positive remarkable effects were noted. Despite all theoretical assumptions and computer simulations, the localization accuracy outperforms the state of the art. The system appears to be highly tolerant to deviations of the simulation model in terms of room interior and material permittivity. Also, the influence of floor and ceiling reflections appears to be negligible, despite the 2D simplification.

The proposed AoA approach was expanded with RSS and ToF measurements in order to investigate achievable performance gains. The RSS approach only resulted in minor improvements in LOS conditions. The ToF approach exhibits better performance gains in LOS and NLOS situations. However, the accuracy of the ToF measurements should be significant with respect to the room dimensions.

The overall accuracy of the multipath assisted AoA positioning method cannot be reduced to a single value due to the variety of system configurations, however some examples can illustrate the achievable accuracy. A single anchor approach results in median normalized errors between 7% and 9% in LOS conditions, while NLOS situations yield values from 10% to 22%, depending on the environment. In 4-anchor setups, these results improve to 3% for LOS, and 4% in NLOS

situations. The exact configuration of the localization system depends on the required accuracy and robustness. The proposed system exhibits significant performance improvements over the benchmark algorithms and comparable systems in literature, especially in NLOS conditions. However, the exceptional performance of dedicated UWB multipath assisted solutions was not matched.

The presented research provides a proof of concept for indoor multipath assisted AoA positioning, relying on narrowband signals and antenna arrays. These properties make the technology compatible with emerging MIMO or MaMIMO communication systems, allowing a 'signals-of-opportunity' approach for the localization system. The proposed method uses multipath propagation as a valuable source of information, even in NLOS conditions. However, an obstruction of the LOS path still results in degraded performance, therefore NLOS avoidance should be a major goal. This could be achieved by using planar arrays mounted on the ceiling, instead of wall mounted linear arrays.

In comparison to contemporary localization systems, the multipath assisted AoA positioning method and the studied optimizations allow for simpler system architectures without sacrificing localization performance, resulting in decreased hardware costs. In fingerprinting systems, setup costs can be reduced since labor intensive surveying is replaced with multipath simulations. Furthermore, computational overhead is considered during system design, as well as power consumption and latency. As a result, the proposed method covers a whole range of requirements, making it a feasible technology in a variety of applications. The most obvious future applications include indoor tracking, guiding and informing people in large buildings. These activities require meter accuracy, which was proven feasible in this work. Furthermore no dedicated hardware is required, because MIMO communication infrastructure is omnipresent and portable wireless devices are widespread.

7.2 Future Work

The performed research mainly focused on the development, demonstration and evaluation of the multipath assisted AoA localization technique. However, further hardware and software development is required to obtain a commercially deployable system.

A transition to non-synthetic antenna arrays can be considered a logical evolution in the hardware design. Furthermore, the wired connection between the mobile node and the measurement equipment should be eliminated. A flexible solution for this future research stage consists of a MIMO Software Defined Radio (SDR) testbed, providing digital access to the physical signals. This allows

a seamless integration of communication and localization services. In a later research stage, the resulting solution can be implemented in a dedicated setup. A concrete application is envisioned in future 5G cellular networks, which aim for localization and communication in a single MaMIMO framework. However, any other MIMO communication technology can be merged with the proposed localization approach.

A specific challenge in the development of a real antenna array consists of the RF design. The combination of multiple antennas leads to mutual coupling, which has been demonstrated to affect AoA estimation performance. Antenna coupling can be minimized with custom antenna designs, exploiting antenna polarization, and post-processing techniques like RMIM. However, the effectiveness of these countermeasures should be evaluated. Furthermore, research on different array structures can improve localization accuracy and reduce hardware complexity. For example, rectangular or conformal arrays provide extra information on elevation angles, while sparse arrays focus on the elimination of array elements.

The design of a real antenna array opens possibilities for a further development of the localization algorithm. In contrast to a synthetic array, all antenna signals can be sampled simultaneously, so no static environment is required during the measurements. This means that real-time tracking of a moving transmitter becomes a possibility. Travelled path tracking can even be further improved with the implementation of dead reckoning techniques, Kalman filtering or particle filters.

Further improvements of the localization algorithm are aimed at the practical applicability in real-world situations. The current solution only considers rectangular rooms with a single omnidirectional antenna, generating a vertically polarized electric field. However, a deployable system should allow arbitrarily shaped room layouts, which require a more extensive multipath simulator. Another feature is user separation, which could be supported by communication protocols. Further research should also focus on the influence of field polarizations and the effect of a human body on localization accuracy. When a reduction of the computational load is aspired, training datasets can be optimized. This is possible by applying non-uniform reference grids and compressing reference vectors. Whenever user privacy becomes a concern, a handset based approach could be applied, with the array acting as a beamforming transmitter, and the mobile node determining its own position based on a local reference dataset and the received signals.

Future research opportunities are not only limited to the field of RF multipath assisted AoA localization. As demonstrated, the proposed framework can easily be tailored to RSS or ToF based localization measurements. Moreover, the developed techniques can be used for acoustic AoA or ToF based positioning, or

even for improving wireless communication links in MIMO systems. Therefore, the multipath simulator can be used for estimating the channel, allowing beamforming without performing channel measurements.

Bibliography

[ACD+11] S. Azzouzi, M. Cremer, U. Dettmar, R. Kronberger, and T. Knie. New measurement results for the localization of uhf rfid transponders using an angle of arrival (aoa) approach. In *2011 IEEE International Conference on RFID*, pages 91–97, April 2011.

[Ana05] Analog Devices. Datasheet AD8347 - 0.8 GHz to 2.7 GHz Direct Conversion Quadrature Demodulator, 2005.

[Ana13] Analog Devices. Datasheet ADL5521 - 400 MHz to 4000 MHz Low Noise Amplifier, 2013.

[APV+13] S. Aerts, D. Plets, L. Verloock, E. Tanghe, W. Joseph, and L. Martens. Empirical path-loss model in train car. In *2013 7th European Conference on Antennas and Propagation (EuCAP)*, pages 3777–3780, April 2013.

[Bar03] L. W. Barclay. *Propagation of Radiowaves*. Institution of Engineering and Technology, 2 edition, 2003.

[Ben08] Alan Bensky. *Wireless Positioning Technologies and Applications*. Artech House, 2008.

[BHH+12] L. Burchett, S. Hartzell, G. Hoffar, J. Mautz, C. Taylor, and A. Terzuoli. Angle of arrival geolocation using non-linear optimization. In *2012 IEEE International Geoscience and Remote Sensing Symposium*, pages 1–4, July 2012.

[BLM+07] A. Broumandan, T. Lin, A. Moghaddam, D. Lu, J. Nielsen, and G. Lachapelle. Direction of arrival estimation of gnss signals based on synthetic antenna array. In *Proceedings of the 20th International Technical Meeting of the Satellite Division*

of The Institute of Navigation, pages 728–738, Fort Worth, TX, September 2007.

[BZR08] Michael J. Biercuk, John C. Zolper, and Carey M. Rappaport. *RF and Microwave Applications and Systems*. The Electrical Engineering Handbook Series. Taylor & Francis, Boca Raton, FL, 2nd edition, 2008.

[CGY10] Z. Chen, G. Gokeda, and Y. Yu. *Introduction to Direction-of-Arrival Estimation*. Artech House, Norwood, MA, 2010.

[Che99] Pi-Chun Chen. A non-line-of-sight error mitigation algorithm in location estimation. In *WCNC. 1999 IEEE Wireless Communications and Networking Conference (Cat. No.99TH8466)*, pages 316–320 vol.1, 1999.

[CiTTG07] P. Cherntanomwong, J. i. Takada, H. Tsuji, and D. Gray. New radio source localization using array antennas based on fingerprinting techniques in outdoor environment. In *2007 Asia-Pacific Microwave Conference*, pages 1–4, Dec 2007.

[CnPHGS01] I. Cuiñas, J.-P. Pugliese, A. Hammoudeh, and M. García Sánchez. Frequency dependence of dielectric constant of construction materials in microwave and millimeter-wave bands. *Microwave and Optical Technology Letters*, 30(2):123–124, 2001.

[CS02] Iñigo Cuiñas and ManuelGarcía Sánchez. Permittivity and conductivity measurements of building materials at 5.8 ghz and 41.5 ghz. *Wireless Personal Communications*, 20(1):93–100, 2002.

[CSW12] Si Wen Chen, Chee Kiat Seow, and Kai Wen. Concept of image based non-line-of-sight (nlos) localization in multipath environments. In *Progress In Electromagnetics Research Symposium Proceedings, Moscow, Russia*, August 2012.

[CVC+16] C. M. Chen, V. Volskiy, A. Chiumento, L. Van der Perre, G. A. E. Vandenbosch, and S. Pollin. Exploration of user separation capabilities by distributed large antenna arrays. In *2016 IEEE Globecom Workshops (GC Wkshps)*, pages 1–6, Dec 2016.

[CZ05] Li Cong and Weihua Zhuang. Nonline-of-sight error mitigation in mobile location. *IEEE Transactions on Wireless Communications*, 4(2):560–573, March 2005.

[dGBCK14] E. d. Groot, T. Bose, C. Cooper, and M. Kruse. Remote transmitter tracking with raytraced fingerprint database. In

2014 IEEE Military Communications Conference, pages 325–328, Oct 2014.

[dVS12] S. Van de Velde and H. Steendam. Cupid algorithm for cooperative indoor multipath-aided localization. In *2012 International Conference on Indoor Positioning and Indoor Navigation (IPIN)*, pages 1–6, Nov 2012.

[dVWM+12] S. Van de Velde, H. Wymeersch, P. Meissner, K. Witrisal, and H. Steendam. Cooperative multipath-aided indoor localization. In *2012 IEEE Wireless Communications and Networking Conference (WCNC)*, pages 3107–3111, April 2012.

[Eme10] Emerson & Cuming Anechoic Chambers NV. Datasheet ECCOSORB VHP-NRL EB-100 Very High Performance Broadband Pyramidal Absorber, 2010.

[Fri46] H. T. Friis. A note on a simple transmission formula. *Proceedings of the IRE*, 34(5):254–256, May 1946.

[GAMD04] E. Grosicki, K. Abed-Meriam, and R. Dehak. A novel method to fight the non-line-of-sight error in aoa measurements for mobile location. In *2004 IEEE International Conference on Communications (IEEE Cat. No.04CH37577)*, volume 5, pages 2794–2798 Vol.5, June 2004.

[GART13] Camillo Gentile, Nayef Alsindi, Ronald Raulefs, and Carole Teolis. *Geolocation techniques principles and applications*. Springer New York, 2013.

[GCGM09] G. Giorgetti, A. Cidronali, S. K. S. Gupta, and G. Manes. Single-anchor indoor localization using a switched-beam antenna. *IEEE Communications Letters*, 13(1):58–60, January 2009.

[GMM+14] Mingming Gan, P. Meissner, F. Mani, E. Leitinger, M. Frohle, C. Oestges, K. Witrisal, and T. Zemen. Low-complexity sub-band divided ray tracing for uwb indoor channels. In *Wireless Communications and Networking Conference (WCNC), 2014 IEEE*, pages 305–310, April 2014.

[God97] L.C. Godara. Application of antenna arrays to mobile communications. ii. beam-forming and direction-of-arrival considerations. *Proceedings of the IEEE*, 85(8):1195–1245, Aug 1997.

[GWL+17] N. Garcia, H. Wymeersch, E. G. Larsson, A. M. Haimovich, and M. Coulon. Direct localization for massive mimo. *IEEE Transactions on Signal Processing*, 65(10):2475–2487, May 2017.

[HAGY08] H. K. Hwang, Zekeriya Aliyazicioglu, Marshall Grice, and Anatoly Yakovlev. Direction of arrival estimation using a root-music algorithm. In *Proceedings of the International MultiConference of Engineers and Computer Scientists*, volume 2, March 2008.

[Hay96] S. Haykin. *Adaptive Filter Theory*. Prentice Hall, Upper Saddle River, NJ, 1996.

[hFnLcL08] S. h. Fang, T. n. Lin, and K. c. Lee. A novel algorithm for multipath fingerprinting in indoor wlan environments. *IEEE Transactions on Wireless Communications*, 7(9):3579–3588, September 2008.

[HHB+03] Tian He, Chengdu Huang, Brian M. Blum, John A. Stankovic, and Tarek Abdelzaher. Range-free localization schemes for large scale sensor networks. In *Proceedings of the 9th Annual International Conference on Mobile Computing and Networking*, MobiCom '03, pages 81–95, New York, NY, USA, 2003. ACM.

[HL06] H. T. Hui and S. Lu. Receiving mutual impedance between two parallel dipole antennas. In *TENCON 2006 - 2006 IEEE Region 10 Conference*, pages 1–4, Nov 2006.

[Hoe13] Roger Pierre Fabris Hoefel. Ieee 802.11ac: A performance assessment of single-user transmit beamforming and multi-user mimo transceiver architectures. In *Wireless Communication Systems (ISWCS 2013), Proceedings of the Tenth International Symposium on*, pages 1–5, Aug 2013.

[HPT+16] B. Hanssens, D. Plets, E. Tanghe, C. Oestges, D. P. Gaillot, M. Liénard, L. Martens, and W. Joseph. An indoor localization technique based on ultra-wideband aod/aoa/toa estimation. In *2016 IEEE International Symposium on Antennas and Propagation (APSURSI)*, pages 1445–1446, June 2016.

[IY02] M.F. Iskander and Zhengqing Yun. Propagation prediction models for wireless communication systems. *Microwave Theory and Techniques, IEEE Transactions on*, 50(3):662–673, Mar 2002.

[JLW+01] Zhong Ji, Bin-Hong Li, Hao-Xing Wang, Hsing-Yi Chen, and T. K. Sarkar. Efficient ray-tracing methods for propagation prediction for indoor wireless communications. *IEEE Antennas and Propagation Magazine*, 43(2):41–49, April 2001.

[JSR11] M.S. Juwita, S. Ummi Syafiqah, and A. Mohd Riduan. Ray tracing algorithm for specific indoor propagation modeling. *Journal of Telecommunication, Electronic and Computer Engineering*, 3(2):15–21, Dec 2011.

[KC10] M. Kwak and J. Chong. A new double two-way ranging algorithm for ranging system. In *2010 2nd IEEE InternationalConference on Network Infrastructure and Digital Content*, pages 470–473, Sept 2010.

[KH06] Krzysztof W. Kolodziej and Johan Hjelm. *Local Positioning Systems: LBS Applications and Services*. CRC Press, Boca Raton, FL, 2006.

[KLM+16] J. Kulmer, E. Leitinger, P. Meissner, S. Hinteregger, and K. Witrisal. Cooperative localization and tracking using multipath channel information. In *2016 International Conference on Localization and GNSS (ICL-GNSS)*, pages 1–6, June 2016.

[KNO+01] N. E. Klepeis, W. C. Nelson, W. R. Ott, J. P. Robinson, A. M. Tsang, P. Switzer, J. V. Behar, S. C. Hern, and W. H. Engelmann. The National Human Activity Pattern Survey (NHAPS): a resource for assessing exposure to environmental pollutants. *Journal of Exposure Analysis and Environmental Epidemiology*, 11(3):231–252, 2001.

[KPGT10] E. Karapistoli, F. N. Pavlidou, I. Gragopoulos, and I. Tsetsinas. An overview of the ieee 802.15.4a standard. *IEEE Communications Magazine*, 48(1):47–53, January 2010.

[Kup05] Axel Kupper. *Location-based Services: Fundamentals and Operation*. John Wiley & Sons, 2005.

[KWC13] E. Kupershtein, M. Wax, and I. Cohen. Single-site emitter localization via multipath fingerprinting. *IEEE Transactions on Signal Processing*, 61(1):10–21, Jan 2013.

[Lam90] R. W. Lampe. Compensation of phase errors due to coaxial cable flexure in near-field measurements. In *Antennas and Propagation Society International Symposium, 1990. AP-S. Merging Technologies for the 90's. Digest.*, pages 1322–1324 vol.3, May 1990.

[LDBL07] Hui Liu, H. Darabi, P. Banerjee, and Jing Liu. Survey of wireless indoor positioning techniques and systems. *Systems, Man, and Cybernetics, Part C: Applications and Reviews, IEEE Transactions on*, 37(6):1067–1080, Nov 2007.

[LETM14] E. G. Larsson, O. Edfors, F. Tufvesson, and T. L. Marzetta. Massive mimo for next generation wireless systems. *IEEE Communications Magazine*, 52(2):186–195, February 2014.

[LFR96] O. Landron, M. J. Feuerstein, and T. S. Rappaport. A comparison of theoretical and empirical reflection coefficients for typical exterior wall surfaces in a mobile radio environment. *IEEE Transactions on Antennas and Propagation*, 44(3):341–351, Mar 1996.

[LG11] Z.-Y. Liu and L.-X. Guo. A quasi three-dimensional ray tracing method based on the virtual source tree in urban microcellular environments. *Progress In Electromagnetics Research*, 118:397–414, 2011.

[LH10] Hoi Shun Lui and Hon Tat Hui. Mutual coupling compensation for direction-of-arrival estimations using the receiving-mutual-impedance method. *International Journal of Antennas and Propagation*, 2010(373061), 2010.

[LHL09] Hoi-Shun Lui, H. T. Hui, and Mook Seng Leong. A note on the mutual-coupling problems in transmitting and receiving antenna arrays. *IEEE Antennas and Propagation Magazine*, 51(5):171–176, Oct 2009.

[Lim12] S. Y. Lim. A ray tracing method for radio wave propagation prediction on selected locations of sun-u campus. *Sunway Academic Journal*, 9:43–58, 2012.

[LR14] Binghao Li and Chris Rizos. Editorial. *Journal of Location Based Services*, 8(1):1–2, 2014.

[LSG+16] S. De Lausnay, L. De Strycker, J. P. Goemaere, B. Nauwelaers, and N. Stevens. A survey on multiple access visible light positioning. In *2016 IEEE International Conference on Emerging Technologies and Innovative Business Practices for the Transformation of Societies (EmergiTech)*, pages 38–42, Aug 2016.

[Mau09] R. Mautz. The challenges of indoor environments and specification on some alternative positioning systems. In *2009 6th Workshop on Positioning, Navigation and Communication*, pages 29–36, March 2009.

[MCGM10] S. Maddio, A. Cidronali, G. Giorgetti, and G. Manes. Calibration of a 2.45 ghz indoor direction of arrival system based on unknown antenna gain. In *The 7th European Radar Conference*, pages 77–80, Sept 2010.

[Mei14] Paul Meissner. *Multipath-Assisted Indoor Positioning.* PhD thesis, Graz University of Technology, October 2014.

[MGM+13] P. Meissner, M. Gan, F. Mani, E. Leitinger, M. Fröhle, C. Oestges, T. Zemen, and K. Witrisal. On the use of ray tracing for performance prediction of uwb indoor localization systems. In *2013 IEEE International Conference on Communications Workshops (ICC)*, pages 68–73, June 2013.

[MGW10] P. Meissner, T. Gigl, and K. Witrisal. Uwb sequential monte carlo positioning using virtual anchors. In *2010 International Conference on Indoor Positioning and Indoor Navigation*, pages 1–10, Sept 2010.

[MLG+05] A. Mandal, C. V. Lopes, T. Givargis, A. Haghighat, R. Jurdak, and P. Baldi. Beep: 3d indoor positioning using audible sound. In *Second IEEE Consumer Communications and Networking Conference, 2005. CCNC. 2005*, pages 348–353, Jan 2005.

[MLLW14] P. Meissner, E. Leitinger, M. Lafer, and K. Witrisal. Real-time demonstration of multipath-assisted indoor navigation and tracking (mint). In *Communications Workshops (ICC), 2014 IEEE International Conference on*, pages 144–149, June 2014.

[MLVC09] D. Munoz, F.B. Lara, C. Vargas, and R.E. Caldera. *Position Location Techniques and Applications.* Academic Press, Burlington, MA, 2009.

[Mol11] Andreas Molisch. *Wireless Communications.* John Wiley & Sons, Chichester, West Sussex, United Kingdom, 2nd edition, 2011.

[MPV03] M. McGuire, K. N. Plataniotis, and A. N. Venetsanopoulos. Location of mobile terminals using time measurements and survey points. *IEEE Transactions on Vehicular Technology*, 52(4):999–1011, July 2003.

[MSW10] P. Meissner, C. Steiner, and K. Witrisal. Uwb positioning with virtual anchors and floor plan information. In *2010 7th Workshop on Positioning, Navigation and Communication*, pages 150–156, March 2010.

[MW08] Michael E. Majerus and James B. West. *RF and Microwave Passive and Active Technologies.* The Electrical Engineering Handbook Series. Taylor & Francis, Boca Raton, FL, 2nd edition, 2008.

[MYTB12] A. Mannesson, M. A. Yaqoob, F. Tufvesson, and B. Bernhardsson. Radio and imu based indoor positioning and tracking. In *2012 19th International Conference on Systems, Signals and Image Processing (IWSSIP)*, pages 32–35, April 2012.

[Nan10] Nanotron Technologies 2010. nanoLOC Development Kit 3.0. Technical report, April 2010.

[ÖDV14] O. Öçal, I. Dokmanić, and M. Vetterli. Source localization and tracking in non-convex rooms. In *2014 IEEE International Conference on Acoustics, Speech and Signal Processing (ICASSP)*, pages 1429–1433, May 2014.

[OIS13] M. Ohtani, H. Iwai, and H. Sasaoka. Evaluation of terminal position estimation by position fingerprinting technique using array antenna. In *2013 Asia-Pacific Microwave Conference Proceedings (APMC)*, pages 392–394, Nov 2013.

[OMHS13] M.-K. Olkkonen, V. Mikhnev, and E. Huuskonen-Snicker. Complex permittivity of concrete in the frequency range 0.8 to 12 ghz. In *Antennas and Propagation (EuCAP), 2013 7th European Conference on*, pages 3319–3321, April 2013.

[PAK+05] N. Patwari, J. N. Ash, S. Kyperountas, A. O. Hero, R. L. Moses, and N. S. Correal. Locating the nodes: cooperative localization in wireless sensor networks. *IEEE Signal Processing Magazine*, 22(4):54–69, July 2005.

[PDV14] R. Parhizkar, I. Dokmanić, and M. Vetterli. Single-channel indoor microphone localization. In *2014 IEEE International Conference on Acoustics, Speech and Signal Processing (ICASSP)*, pages 1434–1438, May 2014.

[PP00] Zoya B. Popovic and Branko D. Popovic. *Introductory Electromagnetics*. Prentice Hall, 2000.

[PZ02] D. Parker and D. C. Zimmermann. Phased arrays - part 1: theory and architectures. *IEEE Transactions on Microwave Theory and Techniques*, 50(3):678–687, Mar 2002.

[RBZF10] F. Ribeiro, D. Ba, C. Zhang, and D. Florêncio. Turning enemies into friends: Using reflections to improve sound source localization. In *2010 IEEE International Conference on Multimedia and Expo*, pages 731–736, July 2010.

[RK89] R. Roy and T. Kailath. Esprit-estimation of signal parameters via rotational invariance techniques. *IEEE Transactions on Acoustics, Speech and Signal Processing*, 37(7):984–995, 1989.

[RWK16] M. Rzymowski, P. Woznica, and L. Kulas. Single-anchor indoor localization using espar antenna. *IEEE Antennas and Wireless Propagation Letters*, 15:1183–1186, 2016.

[SAZ07] Simon R. Saunders and Alejandro Aragon-Zavala. *Antennas and Propagation for Wireless Communication Systems*. John Wiley & Sons, Chichester, West Sussex, England, 2nd edition, 2007.

[SBO11] P. Svaizer, A. Brutti, and M. Omologo. Use of reflectedwavefronts for acoustic source localization with a line array. In *2011 Joint Workshop on Hands-free Speech Communication and Microphone Arrays*, pages 165–169, May 2011.

[SDB07] M. Salamah, E. Doukhnitch, and C. Bayramer. Dynamic hardware-oriented algorithm for angle of arrival positioning technique. In *2007 IEEE International Conference on Signal Processing and Communications*, pages 201–204, Nov 2007.

[Sey05] J. Seybold. *Introduction to RF Propagation*. John Wiley & Sons, Hoboken, New Jersey, 2005.

[SGG08] Zafer Sahinoglu, Sinan Gezici, and Ismail Guvenc. *Ultra-wideband Positioning Systems*. Cambridge University Press, Cambridge, UK, 2008.

[Sim01] Rainee N. Simons. *Coplanar Waveguide Circuits, Components & Systems*. John Wiley & Sons, New York, NY, USA, 2001.

[SIM11] Majdi Salem, Mahamod Ismail, and Norbahiah Misran. Validation of three-dimensional ray-tracing algorithm for indoor wirless propagations. *ISRN Communications and networking*, 2011:5, 2011.

[SJRMB02] Ahmad Safaai-Jazi, Sedki M. Riad, A. Muqaibel, and Ahmet Bayram. Ultra-wideband propagation measurements and channel modeling. Technical report, Virginia Polytechnic Institute and State University, November 2002.

[SKS12] Satvir Singh Sidhu, Arun Khosla, and Ashita Sharma. Implementation of 3-d ray tracing propagation model for indoor wireless communication. *International Journal of Electronics Engineering*, 4(1):43–47, 2012.

[SL15] V. Savic and E. G. Larsson. Fingerprinting-based positioning in distributed massive mimo systems. In *2015 IEEE 82nd Vehicular Technology Conference (VTC2015-Fall)*, pages 1–5, Sept 2015.

[SLD08] Yizhu Shen, C.L. Law, and Wenbin Dou. Ultra-wideband measurement of the dielectric constant and loss tangent of concrete slabs. In *Microwave Conference, 2008 China-Japan Joint*, pages 537–540, Sept 2008.

[SM99] Hae-Won Son and Noh-Hoon Myung. A deterministic ray tube method for microcellular wave propagation prediction model. *IEEE Transactions on Antennas and Propagation*, 47(8):1344–1350, Aug 1999.

[SM05] Petre Stoica and Randolph Moses. *Spectral Analysis of Signals*. Prentice Hall, Upper Saddle River, NJ, USA, 2005.

[SPK86] D. Spielman, A. Paulraj, and T. Kailath. Performance analysis of the music algorithm. In *IEEE international Conference on Acoustics, Speech and Signal Processing 11*, pages 1909–1912, 1986.

[SRFb+11] H. Saad, H.A. Rahman, N. Fazlina bt.Naim, M.H. bin Mohd Nasir, I. Pasya, and Z. Awang. Simulation of microwave non destructive testing environment (mndt) in determining the dielectric constant of concrete using waveguide port approximation at 8-12ghz (x-band). In *RF and Microwave Conference (RFM), 2011 IEEE International*, pages 83–86, Dec 2011.

[SSJ13] Hema Singh, H. L. Sneha, and R. M. Jha. Mutual coupling in phased arrays: A review. *International Journal of Antennas and Propagation*, 2013(348123), 2013.

[ST08] C. K. Seow and S. Y. Tan. Non-line-of-sight localization in multipath environments. *IEEE Transactions on Mobile Computing*, 7(5):647–660, May 2008.

[STK05] A.H. Sayed, A. Tarighat, and N. Khajehnouri. Network-based wireless location: challenges faced in developing techniques for accurate wireless location information. *Signal Processing Magazine, IEEE*, 22(4):24–40, July 2005.

[SWSPB03] Tapan K. Sarkar, Michael C. Wicks, Magdalena Salazar-Palma, and Robert J. Bonneau. *Smart Antennas*. John Wiley & Sons, Hoboken, New Jersey, 2003.

[Tao15] Taoglas. Specification: Wi-Fi Dual-band 2.4/5 GHz Embedded Ceramic Patch Antenna, 2015.

[TCL+17] P. H. Tseng, Y. C. Chan, Y. J. Lin, D. B. Lin, N. Wu, and T. M. Wang. Ray-tracing-assisted fingerprinting based on channel impulse response measurement for indoor positioning. *IEEE Transactions on Instrumentation and Measurement*, 66(5):1032–1045, May 2017.

[Tex14] Texas Instruments. Datasheet TRF37D73 1-6000 MHz RF Gain Block, May 2014.

[TGdAG09] A. Tayebi, J. Gomez, F. S. de Adana, and O. Gutierrez. Ray-tracing application to mobile localization in multipath indoor environments. In *2009 International Conference on Electromagnetics in Advanced Applications*, pages 412–415, Sept 2009.

[THAD11] C. Thajudeen, A. Hoorfar, F. Ahmad, and T. Dogaru. Measured complex permittivity of walls with different hydration levels and the effect on power estimation of twri target returns. *Progress In Electromagnetics Research B*, 30:177–199, 2011.

[TJL+10] E. Tanghe, W. Joseph, M. Lienard, A. Nasr, P. Stefanut, L. Martens, and P. Degauque. Statistics of multipath component clustering in an office environment. In *Proceedings of the Fourth European Conference on Antennas and Propagation*, pages 1–5, April 2010.

[TT95] W. K. Tam and V. N. Tran. Propagation modelling for indoor wireless communication. *Electronics Communication Engineering Journal*, 7(5):221–228, Oct 1995.

[VB95] C. Vaidyanathan and K. M. Buckley. Performance analysis of the mvdr spatial spectrum estimator. *IEEE Transactions on Signal Processing*, 43(6):1427–1437, Jun 1995.

[VT05] H.L. Van Trees. *Optimum Array Processing.* John Wiley & Sons, New York, 2005.

[WTCL15] T. M. Wang, P. H. Tseng, Y. C. Chan, and D. B. Lin. A ray-tracing based fingerprinting for indoor positioning. In *2015 IEEE 12th Intl Conf on Ubiquitous Intelligence and Computing and 2015 IEEE 12th Intl Conf on Autonomic and Trusted Computing and 2015 IEEE 15th Intl Conf on Scalable Computing and Communications and Its Associated Workshops (UIC-ATC-ScalCom)*, pages 1859–1863, Aug 2015.

[Yan17] T. C. Yang. Deconvolved conventional beamforming for a horizontal line array. *IEEE Journal of Oceanic Engineering*, PP(99):1–13, 2017.

[YBWT12] Zhong Yanhui, Zhang Bei, Shi Wenbo, and Wang Tao. Experimental research on relationships between dielectric constant of cement concrete materials and measuring frequency. In *Ground Penetrating Radar (GPR), 2012 14th International Conference on*, pages 403–406, June 2012.

[YI05] Zhengqing Yun and M. F. Iskander. Characterization of angle of arrival based on ray-tracing for an indoor wireless communications environment. In *IEEE/ACES International Conference on Wireless Communications and Applied Computational Electromagnetics, 2005.*, pages 736–739, April 2005.

[YLAU11] L. Yu, M. Laaraiedh, S. Avrillon, and B. Uguen. Fingerprinting localization based on neural networks and ultra-wideband signals. In *2011 IEEE International Symposium on Signal Processing and Information Technology (ISSPIT)*, pages 184–189, Dec 2011.

[YNH12] Yantao Yu, Choon Hock Niow, and Hon Tat Hui. Mutual coupling compensation for a compact array in direction finding. In *Progress In Electromagnetics Research Symposium Proceedings, Kuala Lumpus, Malaysia*, pages 1338–1340, March 2012.

[ZLS+13] L. Zhang, X. Liu, J. Song, C. Gurrin, and Z. Zhu. A comprehensive study of bluetooth fingerprinting-based algorithms for localization. In *2013 27th International Conference on Advanced Information Networking and Applications Workshops*, pages 300–305, March 2013.

Curriculum Vitae

Stijn Wielandt was born in Sint-Niklaas, Belgium on April 8, 1989. He obtained the Master degree in Engineering Technology, Electronics from then KAHO Sint-Lieven, Ghent, Belgium, in 2011. After his studies, he joined the DRAMCO (wireless and mobile communications) research group to investigate inductive power transfer systems. In 2013, he started his PhD at the same research group of KU Leuven in Ghent, investigating "Indoor Multipath Assisted Angle of Arrival Localization". In this context, he spent two months at the Darmstadt University of Applied Sciences. Besides his work as a researcher, he supported lab exercises at the faculty of Engineering Technology of KU Leuven. He also supervised numerous bachelor and master theses in Ghent and in Darmstadt.

List of Publications

Articles as Main Author

Papers at International Conferences and Symposia

2017 S. Wielandt, M. Shah, N. Athaullah, U. Sayyad, R. Yadav, R. Dharamdasani, L. De Strycker, and M. Kuhn. 2.4 GHz single anchor node indoor localization system with angle of arrival fingerprinting. In *2017 Wireless Days*, pages. 152–154, March 2017.

2016 S. Wielandt, J. Goemaere, and L. De Strycker. 2.4 GHz synthetic linear antenna array for indoor propagation measurements in static environments. In *Indoor Positioning and Indoor Navigation (IPIN), 2016 International Conference on*, Oct 2016.

2016 S. Wielandt, J. Goemaere, and L. De Strycker. Multipath-assisted angle of arrival indoor positioning system in the 2.4 GHz and 5 GHz band. In *Indoor Positioning and Indoor Navigation (IPIN), 2016 International Conference on*, Oct 2016.

2015 S. Wielandt, J. Goemaere, L. De Strycker, and B. Nauwelaers. Performance simulations of a 2.4 GHz indoor angle of arrival system for multipath components. In *Indoor Positioning and Indoor Navigation (IPIN), 2015 International Conference on*, Oct 2015.

2015 S. Wielandt, J. Goemaere, L. De Strycker, and B. Nauwelaers. Indoor localization system based on correlation of MVDR spatial spectra. In *Indoor Positioning and Indoor Navigation (IPIN), 2015 International Conference on*, Oct 2015.

2015 S. Wielandt. Angle of arrival localization in indoor multipath environments. In *Indoor Positioning and Indoor Navigation (IPIN), 2015 International Conference on*, Oct 2015.

2015 S. Wielandt, J. Goemaere, L. De Strycker, and B. Nauwelaers. RF ray tracing in various indoor environments: a study for angle of arrival localization. In *Location Based Services (LBS), 2015 International Symposium on*, Sep 2015.

2015 S. Wielandt, B. Thoen, J. Goemaere, L. De Strycker, and N. Stevens. Inductive charging of an EDLC powered wristband device for medical measurements. In *Circuit Theory and Design (ECCTD), 2015 European Conference on*, Aug 2015.

2014 S. Wielandt, J. Goemaere, L. De Strycker, and N. Stevens. Study of wireless power systems with two-dimensionally moving receivers. In *Wireless Power Transfer Conference (WPTC), 2014 IEEE*, pages. 243–246, May 2014.

2014 S. Wielandt, J. Goemaere, L. De Strycker, and N. Stevens. Study and simulations of an angle of arrival localization system for indoor multipath environments. In *Location Based Services (LBS), 2014 International Symposium on*, pages. 203-211 Nov 2014.

2014 S. Wielandt, A. Van Nieuwenhuyse, J. Goemaere, B. Nauwelaers, and L. De Strycker. Evaluation of angle of arrival estimation for localization in multiple indoor environments. In *2014 Ubiquitous Positioning Indoor Navigation and Location Based Services (UPINLBS)*, pages 36–43, 2014.

2013 S. Wielandt, L. De Strycker, J. Goemaere, and N. Stevens. Influence of shielding materials on coil characteristics in inductive wireless power systems. In *Electromagnetic Compatibility (EMC EUROPE), 2013 International Symposium on*, pages. 605–609 Nov 2013.

2013 S. Wielandt, and N. Stevens. Influence of magnetic design choices on the quality factor of off-the-shelf wireless power transmitter and receiver coils. In *Wireless Power Transfer Conference (WPTC), 2013 IEEE*, pages. 151–154 May 2013.

2012 S. Wielandt, D. Mercy, N. Stevens, L. De Strycker, and J. Goemaere. Evaluation of shielding materials for low frequency RFID systems. In *Electromagnetic Compatibility (EMC EUROPE), 2012 International Symposium on*, sep 2012.

2012 S. Wielandt, G. Ottoy, J. Goemaere, N. Stevens, and L. De Strycker. Integration of a CAN bus in an onboard computer for space applications. In *Developement and Application Systems (DAS), International conference on*, May 2012.

2012 S. Wielandt, T. Van Maerhem, N. Stevens, and J. Cappelle. Testing compliance of wireless power transmitters to EMC and public health legislation. In *Wireless Energy Transport and Harvesting, International workshop on*, May 2012.

Articles as Co-Author

Papers at International Conferences and Symposia

2014 A. Van Nieuwenhuyse, S. Wielandt, J. Goemaere, L. De Strycker, B. Nauwelaers. Resolving positions of coherent sources using linear antenna arrays at 2.4 GHz. In *2014 Ubiquitous Positioning Indoor Navigation and Location Based Service (UPINLBS)*, pages 141–147, Nov 2014.

2014 B. Thoen, S. Wielandt, J. De Baere, J. Goemaere, L. De Strycker, and N. Stevens. Design of an inductively coupled wireless power system for moving receivers. In *Wireless Power Transfer Conference (WPTC), 2014 IEEE*, pages 48–51, May 2014.

FACULTY OF ENGINEERING TECHNOLOGY
DEPARTMENT OF ELECTRICAL ENGINEERING
DRAMCO RESEARCH GROUP
Gebroeders De Smetstraat 1
B-9000 Gent
stijn.wielandt@kuleuven.be
http://www.dramco.be